Local Correlation Methods for Extended Systems



Kesha Tarun Sorathia

St Hilda's College

University of Oxford

A thesis submitted for the degree of

Doctor of Philosophy

Hilary 2025

Dedicated to my parents,

Neeta and Tarun Sorathia

Acknowledgements

I extend my gratitude to my supervisor, Prof. David Tew, for his support during the research phase and for his immense patience and encouragement throughout the writing of this thesis. His expertise and insightful guidance have been instrumental in shaping my understanding of electronic structure theory and quantum chemistry more broadly. His rigorous and meticulous approach to work has certainly influenced my growth as a researcher.

I am thankful to Andrew and Arman for continuing the work on this project and for keeping me informed with regular updates–it meant a lot to stay connected through their efforts.

My DPhil undertaking has felt like living three distinct lives–first in Stuttgart, then in Oxford, and finally in Cambridge. I fondly remember my time in the Alavi group in Stuttgart and am grateful to Oscar, Eugenio, Giovanni, Gaurav, Gonçalo Karla for making it truly memorable. Both Oxford and Cambridge are so similar, yet so uniquely different. I am particularly thankful to Padma and Devanshi for the warmth of their friendship during my time in Oxford. And to the Cambridge 'gang'–Sangam, Arya, Shubhangi, Devesh, Akash, and Charu–thank you for becoming my family and filling my life in Cambridge with laughter, care, and unforgettable memories. I am grateful for the encouragement from my friends and colleagues at Quantinuum, especially Michelle, Basudha, and Seyon, who have been on my mind during the writing of this thesis.

This journey would not have been possible without the unwavering support of my wonderful family. I will forever be indebted to my parents for their unconditional support towards my education, which made this journey a reality. A special mention goes to my little brother, Manan, whom I missed watching grow up and mature during my DPhil years. I thank him for always challenging my choices with brutal honesty yet secretly rooting for my success in everything I do.

Last but certainly not least, my partner, Prakrut, has been nothing short of an inspiration throughout my pursuit of science. Words fall short of capturing how deeply his support and encouragement have meant to me, especially during the writing of this thesis. I can only hope to one day repay his thoughtfulness, care, and the quiet sacrifices he has made along the way.

Declaration

I, Kesha Tarun Sorathia, declare that the work presented in this thesis is my own original work except where indicated otherwise.

Signature	*Date*

List of Publications

Chapter 5 is based on two collaborative works published in the following peer-reviewed articles. My specific contributions to each publication are indicated below:

1 Sorathia, K., Tew, D. P. *Basis set extrapolation in pair natural orbital theories*. *The Journal of Chemical Physics*, 153(17), 174112 (**2020**).

Contribution: Implementation of a two-point pairwise extrapolation scheme, execution of calculations, data analysis, and manuscript writing.

2 Sorathia, K., Frantzov, D., Tew, D. P. *Improved CPS and CBS extrapolation of PNO-CCSD(T) energies: The MOBH35 and ISOL24 data sets*. *Journal of Chemical Theory and Computation*, 20(7), 2740–2750 (**2024**).

Contribution: Performed and analysed calculations for the MOBH35 data set.

Abstract

Despite constituting only a tiny fraction of the total electronic energy, the correlation energy stemming from electron-electron Coulomb interactions is of the order of the binding energy of a system. A hierarchy of quantum chemical methods, while capable of systematically improving the accuracy of correlation effects, simultaneously increases the computational cost. Crystalline solids are especially susceptible to the high costs of these methods due to their extended nature. Consequently, notwithstanding its limitations, density functional theory continues to be the primary instrument for simulating the electronic structure of solids. Initially formulated for molecular systems, local correlation methods leverage the short-range characteristics of dynamical electron correlation. Despite the increased complexity of the underlying equations, the local correlation approach significantly reduces the computational scaling of these quantum chemistry techniques, thus enabling the treatment of molecules with hundreds of atoms. In this work, we develop a theoretical framework for a local correlation treatment of extended systems employing domain-based pair natural orbitals (PNOs) at the level of second-order Møller-Plesset perturbation theory (MP2). We present a new technique solely relying on Cholesky-factorised Γ-point Bloch orbitals to obtain localised Wannier functions, which facilitate the local correlation treatment in periodic systems. We also present the results of preliminary calculations carried out on 1D and 2D systems with our PNO-MP2 implementation. We discuss various aspects of the implementation and the techniques adopted, particularly the challenges in the density fitting of electron repulsion integrals. Towards the end of the thesis, we discuss the investigation of various extrapolation schemes to mitigate the error due to the truncation of PNO space and consequently approach the complete basis set limit.

Table of Contents

1 Motivation and Outline **1**

2 Background Theory **6**

2.1 The Electronic Hamiltonian and the Wavefunction 6

2.2 The Hartree-Fock Theory 10

2.2.1 Brillouin's Theorem and Canonical Orbitals 12

2.2.2 The Basis Set Approximation 12

2.3 Orbital Rotations 13

2.4 Natural Orbitals 14

2.5 Many-Body Perturbation Theory 16

2.6 Second-Order Møller-Plesset Perturbation Theory (MP2) 20

2.6.1 Notes on MP2 24

2.7 The MP2 Hylleraas Functional 25

2.8 Orbital-Invariant MP2 Theory 27

2.9 Fundamentals of Local Correlation Approach 30

2.10 Localised Occupied Space 32

2.10.1 Foster-Boys (FB) 32

2.10.2 Edmiston-Ruedenberg (ER) 32

2.10.3 Pipek-Mezey (PM) 33

2.10.4 Intrinsic Bond Orbitals (IBOs) 33

2.10.5 Cholesky Orbitals 34

2.11 Local Virtual Space 35

2.11.1 Projected Atomic Orbitals (PAOs) 36

2.11.2 Pair Natural Orbitals (PNOs) 38

2.11.2.1 Orbital-Specific Virtuals (OSVs) 40

2.12 Conclusions 41

3 Periodic PNO-MP2 **43**

3.1 Bloch Theorem and Periodic Boundary Conditions 43

3.2 Linear Combination of Atomic Orbitals in Crystals 50

3.3 Periodic Hartree-Fock Theory . . . 52
3.4 Periodic Canonical MP2 Theory . . . 53
3.4.1 Coulomb Integrals Between Bloch Orbitals . . . 54
3.5 Wannier Functions . . . 56
3.6 Localised Wannier Orbitals . . . 58
3.7 Periodic Local MP2 with Wannier Orbitals . . . 60
3.8 BvK Supercell PAOs . . . 61
3.9 BvK Supercell OSVs . . . 63
3.10 Periodic Local MP2 with PNOs . . . 65
3.11 Periodic Density Fitting . . . 66
3.12 Conclusions . . . 69

4 Calculations: Results and Discussion **71**
4.1 Cholesky Wannier Orbitals . . . 71
4.2 Correlation Energy Per Cell: Periodic vs Molecular . . . 74
4.3 Rolling Energy of BN Nanoscroll . . . 79
4.4 Notes on Implementation . . . 83
4.5 Conclusions . . . 86

5 Extrapolation Schemes in PNO Methods **88**
5.1 Extrapolation of PNO-MP2 Energies . . . 89
5.1.1 Extrapolation to the Canonical Limit . . . 89
5.1.2 Extrapolation to the Basis Set Limit . . . 89
5.1.3 Test Sets and Computational Details . . . 92
5.1.4 Results and Discussion . . . 95
5.2 Extrapolation of PNO-CCSD(T) Energies . . . 102
5.2.1 Extrapolation Error Models for PNO-CCSD(T) . . . 102
5.2.2 Computational Details, Structures and Basis Sets . . . 104
5.2.3 Results and Discussion . . . 106
5.2.3.1 Error model $E(T) = E + AT^{\alpha}$ . . . 106
5.2.3.2 Error model $E(T) = E + A(T)T^{1/2}$ . . . 109
5.2.4 Benchmark Data . . . 116

5.3 Conclusions 119

6 Summary and Outlook **123**

List of Figures

4.1 SCF-converged Wannier orbitals for an 11-unit polyethylene chain, plotted with an isosurface value of 0.01. 73

4.2 Cholesky-localised Wannier orbitals for an 11-unit polyethylene chain, plotted with an isosurface value of 0.01. 73

4.3 SCF-converged Wannier orbitals for a $5 \times 5 \times 5$ silicon lattice, plotted with an isosurface value of 0.001. 73

4.4 Cholesky-localised Wannier orbitals for a $5 \times 5 \times 5$ silicon lattice, plotted with an isosurface value of 0.001. 74

4.5 (a)Illustration of a polyethylene molecule with a total length equivalent to 15 repeating units of the monomer, ethylene (C_2H_2). The red box indicates the unit cell employed in periodic calculations or the monomer unit employed in molecular calculations. (b) Decomposition of a finite 1D molecular chain into middle (M) and edge (E) cells. 75

4.6 Comparison of HF energy per unit cell (in Ha) between periodic and molecular results of Polyethylene, plotted as a function of the number of **k**-points for (a) def-SVP and (b) pob-TZVP basis sets 76

4.7 Comparison of PNO-MP2 correlation energy per unit cell (in Ha) from periodic (per) and molecular (mol) calculations against canonical MP2 results of Polyethylene, plotted as a function of the number of **k**-points for (a) def-SVP and (b) pob-TZVP basis sets and PNO thresholds in the range of 10^{-5} and 10^{-9} which are indicated in the legend as 'tol 5', 'tol 6', and so on. 77

4.8 Absolute deviation in PNO-MP2 correlation energy per unit cell (Ha) between periodic and molecular calculations of Polyethylene, plotted as a function of the number of **k**-points for (a) def-SVP and (b) pob-TZVP basis sets and PNO thresholds in the range of 10^{-5} and 10^{-9} which are indicated in the legend as 'tol 5', 'tol 6', and so on. 77

4.9 (a) Xe 5×5 lattice with unit cell highlighted by a square. (b) CO lattice of dimension 3×3 with its unit cell shown in (c). (d) Decomposition of a finite 2D periodic system into corners (C), edges (E) and middle (M) cells. 78

4.10 Illustrations of BN nanosheet and nanoscroll: (a) nanosheet unit cell (b) nanosheet consisting of 5 unit cells (c) nanoscroll unit cell (d) nanoscroll consisting of 5 unit cells 81

5.1 PNO truncation error for the MP2 correlation energy of formic acid using the cc-pVDZ-F12 basis, as a function of PNO threshold T. The data for this plot was extracted from previous work, which involved a test set of 105 reactions generated from a set of 106 molecules compiled by Bakowies. 90

5.2 Mean Absolute Error in correlation energy in kJ/mol per valence electron as a function of (a) N and (b) $1/N$ for 105 reaction energies computed using PNO-MP2 method for cc-pVXZ-F12 (X=D,T,Q) basis sets where N is mean number of PNOs. Data points correspond to PNO thresholds of $-\log T = 3, 4, \ldots, 10$. . 91

5.3 Mean Absolute Errors from basis set incompleteness in the correlation energy for (a) total and (b) reaction energies of the HCNOF set as a function of the average number of PNOs N, computed using three schemes: PNO-MP2 (N_{ij}^{-1}) extrapolation, PNO-MP2+Δ and X^{-3} extrapolation of PNO-MP2+Δ energies. Data points correspond to PNO thresholds of $-\log T = 3.5, 4, \ldots, 10$ 97

5.4 The correlation between QZ and (TQ) basis set errors for reaction energies of (a) the HCNOF set and (b) the Cu set, using canonical MP2 and PNO-MP2+Δ with $T_{\mathrm{PNO}} = 10^{-6}$ and 10^{-7}. 101

5.5 PNO truncation errors for educt number 20 of the ISOL24 set using a cc-pVTZ basis. The legend includes the value of α from the best fit to $\log_{10}(E(T) - E) = \log_{10} A + \alpha \log_{10} T$. 107

5.6 Values of α from linear fits using Equation (5.11) against RMS deviation, for PNO truncation errors in MP2, CCSD, and CCSD(T) energies. 108

5.7 Values of $\alpha(T)$ from Equation (5.12) for PNO-CCSD(T) energies of molecules in the ISOL18 set. 109

5.8 Values of $A(T)$ in the error model $E(T) = E + A(T)T^{1/2}$ for PNO-CCSD(T) energies, expressed in mE_h per valence electron. 110

5.9 Ratios of $A(T)$ between cc-pVTZ and cc-pVDZ basis sets, and between CCSD(T) and MP2 correlation energies for the ISOL18 set. 113

5.10 Schematic of the reactant and product species of reaction 13 in the MOBH35 set, highlighting the C9 position on the ligand involved in hydride transfer. Figure taken from Ref. 3. 114

List of Tables

4.1 PM metric for unoptimised and Cholesky localised Wannier orbitals of Polyethylene and Silicon 72

4.2 Molecular and periodic PNO-MP2 correlation energies per repeating unit calculated for PNO thresholds 10^{-7} and 10^{-8} for the 2D Xe lattice, along with correlation energy per repeating unit obtained after $(3,5,7)$ and $(5,7,9)$ decompositions for molecular calculations. All energies are in the units of Ha. . . 80

4.3 Molecular and periodic PNO-MP2 correlation energies per repeating unit calculated for PNO thresholds 10^{-7} and 10^{-8} for the 2D CO lattice, along with correlation energy per repeating unit obtained after $(3,5,7)$ decomposition for molecular calculations. All energies are in the units of Ha. 80

4.4 Rolling energy per BN unit in kJ/mol computed at DFT, HF and HF+PNO-MP2 level for two PNO thresholds, 10^{-6} and 10^{-7}. PNO-MP2 calculations for the k-point mesh of 5 were not possible for the def-SVP basis as the HF calculation remained unconverged (indicated by '-'). 83

5.1 Mean absolute deviations from the basis set limit of total energies computed with and without using extrapolated PNO-MP2 correlation energies for aug-cc-pVXZ basis sets (kJ/mol per valence electron) for the HCNOF set. 95

5.2 Mean absolute deviations from the basis set limit of total energies computed with and without using extrapolated PNO-MP2 correlation energies for aug-cc-pVXZ basis sets (kJ/mol per valence electron) for the Cu set. T^{α} extrapolation with PNO threshold 10^{-4} is not performed (indicated by '-') as calculation with PNO threshold 10^{-2} introduces large PNO truncation errors. 96

5.3 Mean absolute deviations from the basis set limit of reaction energies computed with and without using extrapolated PNO-MP2 correlation energies for aug-cc-pVXZ basis sets (kJ/mol) for the HCNOF set. 96

5.4 Mean absolute deviations from the basis set limit of reaction energies computed with and without using extrapolated PNO-MP2 correlation energies for aug-cc-pVXZ basis sets (kJ/mol) for the Cu set. T^{α} extrapolation with PNO threshold 10^{-4} is not performed (indicated by '-') as calculation with PNO threshold 10^{-2} introduces large PNO truncation errors. 97
5.5 PNO-CCSD(T) truncation error statistics for $T = 10^{-6}$–10^{-9} in kcal/mol with and without two-point CPS extrapolation 111
5.6 PNO truncation error statistics for CCSD(T)/cc-pVTZ isomerisation energies of the ISOL18 set using Eq 5.17. 114
5.7 Timings and PNO truncation errors in kcal/mol of CCSD(T)/def2-TZVPP barrier heights for MOBH35 reaction 13 using PNO thresholds 10^{-6}-10^{-8} and with extrapolation and correction schemes. 115
5.8 Best estimates for CCSD(T) barrier heights for the MOBH35 test set in kcal/mol 118
5.9 Best estimates for CCSD(T) isomerisation energies for the ISOL24 test set in kcal/mol. 120
5.10 CPS- and CBS-Extrapolated CCSD(T) isomerisation energies in kcal/mol of isomer pairs 4 and 22 in ISOL24 set. 120

Nomenclature

Abbreviations

AO ..... Atomic orbital

MO ..... Molecular orbital

GTO ..... Gaussian-type orbital

LCAO ..... Linear combination of atomic orbitals

DFT ..... Density functional theory

XC ..... Exchange-correlation

HF ..... Hartree-Fock

MP2 ..... Møller-Plesset perturbation theory to 2^{nd} order

CCSD ..... Coupled cluster with singles and doubles

CCSD(T) ..... Coupled cluster with singles, doubles and perturbative triples

MI ..... Method of increments

IAO ..... Intrinsic atomic orbital

IBO ..... Intrinsic bond orbital

PM ..... Pipek-Mezey

LMO ..... Localised molecular orbital

PAO ..... Projected atomic orbital

PNO ..... Pair natural orbital

OSV ..... Orbital specific virtual

ERI ..... Electron repulsion integrals

DF ..... Density fitting

RI ..... Resolution of identity

CFMM ..... Continuous fast multipole method

CBS ..... Complete basis set

CPS ..... Complete PNO space

1D, 2D, 3D .... one-dimensional, two-dimensional, three-dimensional

MAE ..... Mean absolute error

RMS ..... Root mean square

General Notations

r ..... Spatial coordinates of an electron (x, y, z)

x ..... Spatial and spin coordinates of an electron (x, y, z, σ)

$\hat{H}_{el}$ ..... Non-relativistic electronic Hamiltonian

$\hat{F}$ ..... Fock operator

$\hat{U}$ ..... Perturbation operator

$\hat{U}_{MP}$ ..... Perturbation operator in Møller-Plesset perturbation theory

r_{ij}^{-1} ..... Exact two-electron Coulomb operator

Ψ ..... Wavefunction

ψ_{HF} ..... HF wavefunction

$\hat{v}_{HF}$ ..... HF potential

E_{HF} ..... HF energy

$\Phi_0^{(m)}$ ..... m-th order wavefunction

$\psi_i^{a(m)}, \psi_{ij}^{ab(m)}$, ... m-th order singly, doubly ... excited determinants

$t_a^{i(m)}, t_{ab}^{ij(m)}$, ... m-th order single, double ... excitation amplitudes

R ..... Lattice vector in real space lattice

l, m, n, o ..... Unit cell indices

L, M, N, O ..... Supercell indices

$\mathcal{V}$ ..... Volume of supercell

$\mathbf{R}_l$ ..... Lattice vector for unit cell l

$\mathbf{R}_L$ ..... Lattice vector for supercell L

$\hat{\mathbf{T}}_\mathbf{R}$ ..... Translation operator

$\mathbf{k}$ ..... Wavevector in reciprocal space

$\mathbf{G}$ ..... Lattice vector in reciprocal lattice

Orbital Space Notations

μ, ν, κ, τ ..... Atomic basis functions or AOs

i, j, k, l ..... Internal or occupied MOs

a, b, c, d ..... External or virtual MOs

p, q, r, s ..... General indices for MOs

$\rho(\mathbf{r})$ ..... Electron density

$\check{\mu}, \check{\nu}, \check{\kappa}, \check{\tau}$ ..... PAOs

$\bar{a}, \bar{b}, \bar{c}, \bar{d}$ ..... OSVs

$\tilde{a}, \tilde{b}, \tilde{c}, \tilde{d}$ ..... PNOs

$\tilde{a}^{ij}$ ..... PNOs corresponding to pair ij

$\psi_{n\mathbf{k}}$ ..... Bloch function corresponding to wavevector $\mathbf{k}$

$\mu_\mathbf{k}$ ..... Bloch function corresponding to wavevector $\mathbf{k}$ in the LCAO framework

$i_\mathbf{k}$ ..... Bloch orbital (crystalline single particle state)

$\tilde{i}_\mathbf{k}$ ..... Localised Bloch orbital (crystalline single particle state)

$\tilde{i}$ ..... Wannier orbital

$\tilde{i}_l$ ..... Localised Wannier orbital

μ_l ..... AO centred in unit cell l

$\tilde{\mu}_l$ ..... Supercell AO centred in unit cell l

$\check{\mu}_l$ ..... Supercell PAOs

1 | Motivation and Outline

Modelling the electronic structure of molecules and periodic solids predominantly relies on two distinct approaches. The first is the widely popular Density Functional Theory (DFT) based on the density of electrons in the system, while the second encompasses a suite of techniques rooted in the many electron wavefunction. DFT provides an excellent compromise between accuracy and computation time. While being a cost-effective alternative, DFT shows several limitations. The two most prominent issues are the missing long-range correlation effects[4] and the delocalisation error[5]. The lack of adequate treatment for long-range correlation makes accurately capturing dispersion interactions challenging, thus necessitating the use of correlation schemes[6,7]. As a result, studying systems such as molecular crystals where long-range effects are important becomes problematic within the framework of DFT. Owing to the delocalisation error, the standard approximations to the exact exchange-correlation (XC) functionals underestimate the transition state energies, such as in hydrogen-transfer reactions[8,9], band gaps and optical properties in case of periodic solids[10]. This deficiency limits the accuracy and predictive capabilities of DFT for many ubiquitous thermochemical processes. To remedy this issue, several hybrid or double-hybrid exchange-correlation functionals have been developed by mixing a fraction of exact exchange with the standard functionals, leading to improved barrier heights[11–13] and band gaps[14–16]. However, the design of XC functionals remains a fundamental challenge. A universal functional with an optimal fraction of exact exchange that treats on an equal footing both, an extended solid and a molecular reaction occurring on the surface of the solid is far from reality. Functionals which improve specific properties have been explored, and a crude ranking of functionals is possible based on the degree of exchange-correlation interactions they incorporate[17]. However, it is challenging to achieve systematic improvement across all desired properties[18]. This characteristic distinguishes DFT from the class of wavefunction-based methods where a well-defined hierarchy of models enables approaching the exact solution of the non-relativistic electronic Schrödinger equation in a systematic manner. The control over the accuracy of the models makes *ab initio* wavefunction methods the most reliable among the techniques available for treating the electron correlation problem in quantum chemistry.

Wavefunction-based methods have achieved remarkable success in their application to molecular systems and have now become a routine tool in the field. Although DFT remains dominant

to date, wavefunction-based methods began emerging in solid-state physics around the turn of the century. The first implementation of the periodic Hartree-Fock (HF) method dates back to the 1980s[19]. Since then, several post-HF electron correlation methods have been developed for periodic solids. These methods differ primarily in the choice of the one-electron basis, the computational framework adopted (such as direct or reciprocal space formulation), and the theoretical model utilised to capture correlation effects.

Two commonly used basis set expansions representing the crystalline orbitals are: naturally periodic plane waves and atom-centred local functions. Plane wave expansions provide a reciprocal space representation of the simulation cell, independent of the molecular structure. They uniformly fill up a 3D computational box containing the system to be simulated, relying solely on the size and geometry of the cell. This makes plane wave-based calculations free of basis set superposition error (BSSE)[20,21], a notable advantage. Another appealing feature is that plane waves, being eigenfunctions of the kinetic energy operator, allow the quality and completeness of the basis set to be controlled by a single parameter: the kinetic energy cutoff. However, when simulating systems of low dimensionality such as surfaces, or defects, it becomes necessary to expand the cell along the non-periodic directions to create sufficient void space between the periodic images, effectively decoupling their interactions. Plane wave expansion in such systems may lead to undesired effects and thus waste of computational effort[22]. On the other hand, atom-centred functions, such as Gaussian-type orbitals (GTOs), provide a real-space description of the atoms in a simulation cell. They are widely used in molecular electronic structure calculations due to their speed of convergence with respect to basis set size. Other types of atom-centred functions, such as numerical atomic orbitals[23], muffin-tin orbitals[24,25], wavelets[26], and Slater-type orbitals[27,28] have also been developed, but GTOs are the most widely used. An advantage of using atom-centred functions is that periodic boundary conditions can be applied while retaining the true dimensionality of the system. This means that interactions with periodic images, which can introduce spurious effects in low-dimensional systems, can be avoided. In terms of computational performance, plane wave calculations for solid-state systems are generally faster than GTO calculations at the HF level. Nonetheless, plane wave calculations can be more memory-intensive[29] and may show slow convergence with respect to the number of basis functions for post-HF correlation methods[30]. GTOs provide a local basis to expand the wavefunction. Although they are well suited for correlation methods,

GTOs are susceptible to BSSE, however, it can be corrected using the well-known counterpoise method[31]. Additionally, the Gaussian basis sets are optimised for molecular calculations, and their transferability to periodic systems, especially when diffuse functions are involved, is limited. The preceding mean-field calculations encounter difficulties when dealing with large and diffuse basis sets, which are necessary for achieving convergence in correlation methods. Nevertheless, GTOs can be employed by adjusting the exponents of the diffuse functions. The key advantage of utilising GTOs lies in their local character, which facilitates the development of reduced scaling techniques that benefit from the predominantly local nature of dynamical electron correlation. Both plane waves and GTOs have been employed in post-HF correlation calculations for solids, such as second-order Møller-Plesset perturbation theory (MP2)[32–35] and various coupled cluster methods[36–39]. Hybrid approaches that incorporate the strengths of both types of basis sets have also been reported[30,40,41].

At post-HF level, the electron correlation effects in periodic systems can be modeled primarily in two different ways: finite-cluster or fragmentation methods and truly periodic approaches. In finite-cluster methods, the periodic system is approximated by a series of small clusters or fragments. Thus, the total correlation energy of the periodic system is decomposed into a sum of contributions from the series of clusters. The clusters are typically defined by groups of atoms or localised orbitals sharing a common centre, and the key idea in many of these methods is that the result converges to that of the periodic solid as the cluster is expanded. Truly periodic approaches treat the infinite solid as a whole by exploiting its translational symmetry. In practice, these methods use periodic boundary conditions to simulate a solid using a single unit cell, effectively treating the cell as if it were infinitely repeating in space. The quantity of interest in such fully periodic models is the *energy per unit cell*.

One of the earliest correlation methods for periodic systems was the so-called *method of increments* (MI) or the *incremental scheme* introduced by Stoll in 1992[42,43], which falls into the category of finite-cluster methods. The incremental scheme uses a series of energy increments calculated on finite clusters to perform a many-body expansion of the correlation energy. MI has been successfully applied to a variety of systems[44–47], including strongly correlated metallic solids[48,49]. While MI has the potential to converge to the periodic result by increasing cluster size, achieving the desired level of accuracy can be challenging, as the rate of convergence of the correlation energy and other properties with respect to cluster size can vary greatly across

different systems. The cluster-in-molecule approach[50–52] has also been applied to periodic systems[53–55]. Another notable method in the class of cluster-based approaches is the *hierarchical scheme* proposed by Manby *et al.*[56]. In this scheme, the correlation energy is decomposed into residual and non-residual components, where the latter corresponds to the correlation energy of the isolated molecule or the repeating unit, and the residual part is calculated by solving a system of linear equations for clusters of systematically varying sizes such that the corner, edge, or surface effects are eliminated. A common problem in these cluster-based methods is finding an appropriate model for clusters that provides sufficiently accurate results with affordable convergence[44,57,58]. By embedding the cluster in an environment that acts as the missing part of the solid and treating the environment with a less accurate but affordable method, the convergence behaviour can potentially be improved. Several embedding approaches have been employed throughout the years[57,59,60]. However, in practice, partitioning a system into fragment and environment to achieve smooth and rapid convergence remains a challenge.

Approaching the thermodynamic limit in simulations of solids is crucial for making a direct comparison with experiments. This can be achieved by exploiting the translational symmetry of periodic systems through periodic boundary conditions. Such truly periodic methods have been realised at MP2[32,61–63] and coupled-cluster levels[36,37,39,64–66] of theory using canonical formulations of either plane waves or Gaussian basis sets. Results close to the thermodynamic limit require calculations with large simulation cells[34,67–69]. However, in their canonical formulation, wavefunction methods scale unfavourably, e.g., MP2 scales as $O(N^5)$, and the "gold standard" CCSD(T)–coupled cluster with single and double excitations augmented with perturbative triples–scales as $O(N^7)$ with respect to system size N. This steep scaling limits the application of these accurate wavefunction methods to relatively small simulation cells and prevents their routine application to crystalline systems[63,70]. Therefore, achieving the thermodynamic limit in moderate- to large-scale periodic simulations remains beyond the reach of these canonical methods. To overcome this limitation, several approximations have been developed, which reduce the computational cost of wavefunction-based methods while preserving their accuracy. Some of the most successful of these approximations are rooted in exploiting the locality of electron correlation and can be loosely classified into two categories. The first category consists of the aforementioned fragmentation approaches. The second category is based on the *local correlation* ansatz proposed by Pulay and Saebø[71,72]. It treats the whole system at once

but uses *localised orbitals*, which allows for the use of local approximations, thus compressing the virtual space. Such local correlation methods have been applied to molecular systems to achieve reduced, even linear scaling with system size[73–78]. Due to their success in molecular applications, extending local correlation methods to periodic systems is desirable.

Local correlation methods at the MP2 level have been implemented for crystalline systems in the CRYSCOR program[79–82] and have been successfully tested on ionic solids, molecular solids, rare-gas solids, semiconductors and other systems. The efficiency of these methods is mainly governed by their rate of convergence with respect to the size of the virtual space, also known as the *domain size*. Therefore, the definition of localised virtual orbitals plays a key role in determining the convergence rate. Pair Natural Orbitals (PNOs) are known to provide the fastest convergence with respect to their domain sizes. This motivates our effort to extend PNOs to wavefunction methods for extended systems. To the best of our knowledge, this work represents the first implementation of a PNO-based method for periodic systems.

This thesis is structured as follows: Chapter 2 provides relevant theoretical background for the quantum chemical treatment of extended systems and local correlation methods. In Chapter 3, we formulate our periodic method based on PNOs at the MP2 level under periodic boundary conditions. Chapter 4 presents preliminary calculations performed on 1D and 2D systems to validate the proper functioning of our implementation and highlights the challenges to overcome in the near future. Chapter 5 presents complementary studies carried out to investigate basis set truncation errors in PNO methods, and it also presents techniques to extrapolate to the complete PNO space and the complete basis set limit. Chapter 6 summarises the work and presents an outlook for future endeavours.

2 | Background Theory

This chapter introduces the basic concepts and notations of electronic structure theory and local correlation methods. In Section 2.1, we present the structure of the many-electron Hamiltonian and the form of the many-electron wavefunction. In Section 2.2, the HF approximation is introduced. Section 2.3 discusses the invariance of *canonical orbitals*–the solutions of the HF approximation–under unitary transformations. In Section 2.4, we introduce density matrices and the concept of natural orbitals, which will be useful for developing the idea of PNOs in Section 2.11.2. Next, we briefly discuss how the HF theory may fail in capturing correlation effects due to many-electron Coulomb interactions and introduce the general equations for many-body perturbation theory in Section 2.5. We then introduce the MP2 theory as the simplest post-HF correlation method using the HF solution as a starting point in Section 2.6. Since local correlation methods utilise local orbitals, we introduce the MP2 Hylleraas energy functional in order to develop orbital-invariant MP2 theory in Section 2.8 that will set the stage for a local-MP2 method. We then motivate the use of local correlation methods and introduce the primary ideas of a local correlation treatment–the pair approximation and the domain approximation in Section 2.9. In Section 2.10, we discuss the various approaches to obtain localised occupied orbitals. Finally, in Section 2.11, we discuss localisation of the virtual space and introduce intrinsically local virtual orbitals, including the PNOs. Although the equations for the various methods presented in this chapter are for electronic structure calculations of molecules, the ideas presented are general, and extending certain methods to periodic systems will be the subject of the subsequent chapter.

2.1 The Electronic Hamiltonian and the Wavefunction

The full non-relativistic Hamiltonian for N electrons in the field of M nuclei is expressed using atomic units as

$$\hat{H} = -\frac{1}{2}\sum_{i}^{N}\nabla_i^2 - \sum_{A}^{M}\frac{1}{2M_A}\nabla_A^2 - \sum_{i}^{N}\sum_{A}^{M}\frac{Z_A}{|\mathbf{r}_i - \mathbf{r}_A|} + \sum_{i}^{N}\sum_{j>i}^{N}\frac{1}{|\mathbf{r}_i - \mathbf{r}_j|} + \sum_{A}^{M}\sum_{B>A}^{M}\frac{1}{|\mathbf{r}_A - \mathbf{r}_B|} \tag{2.1}$$

The first term in the above equation is the kinetic energy operator for electrons, and the second term is the kinetic energy operator for nuclei, where M_A is the ratio of the mass of the nucleus

A to the mass of an electron. The third term is the Coulomb operator between electrons and nuclei, which involves the atomic number Z_A of nucleus A. The fourth term represents the electron-electron repulsion, and the last term represents the repulsion between nuclei. The coordinates of the electrons and the nuclei are denoted as $\mathbf{r}_i$ and $\mathbf{r}_A$, respectively.

We are only concerned with the motion of electrons, and the nuclei being much heavier than the electrons, move very slowly compared to the electrons. Therefore, we can assume the electrons to be moving in the field of *fixed* nuclei. This is known as the Born-Oppenheimer approximation. Hence, to describe the electronic motion, the second term in Equation (2.1) can be neglected. Moreover, the last term can be regarded as constant, as it does not affect the eigenfunctions of the electronic operators but only adds a constant value to the eigenvalues. Thus, the electronic Hamiltonian becomes

$$\hat{H}_{el} = -\frac{1}{2}\sum_{i}^{N}\nabla_i^2 - \sum_{i}^{N}\sum_{A}^{M}\frac{Z_A}{r_{iA}} + \sum_{i}^{N}\sum_{j>i}^{N}\frac{1}{r_{ij}} \tag{2.2}$$

where we have used the shorthand notations $r_{iA} \coloneqq |\mathbf{r}_i - \mathbf{r}_A|$ and $r_{ij} \coloneqq |\mathbf{r}_i - \mathbf{r}_j|$. We are interested in the ground state solution Ψ_0 to the electronic Schrödinger equation

$$\hat{H}_{el}\Psi_0 = E_0\Psi_0 \tag{2.3}$$

For a normalised ground state solution Ψ_0, the corresponding ground state energy can be evaluated as

$$E_0 = \left\langle \Psi_0 \middle| \hat{H}_{el} \middle| \Psi_0 \right\rangle \tag{2.4}$$

An exact N-electron wavefunction describes the spatial and spin arrangement of N-electrons. It not only must satisfy the Schrödinger equation but must also satisfy Pauli's exclusion principle. This enforces the wavefunction to be antisymmetric upon exchange of either spatial or spin coordinates of any two electrons.

$$\Psi(\mathbf{x}_1, \cdots, \mathbf{x}_i, \cdots, \mathbf{x}_j \cdots \mathbf{x}_N) = -\Psi(\mathbf{x}_1, \cdots, \mathbf{x}_j, \cdots, \mathbf{x}_i \cdots \mathbf{x}_N) \tag{2.5}$$

where $\mathbf{x}_i$ collectively denotes the four spatial coordinates $\mathbf{r}_i$ and one spin coordinate of electron i. Since we can solve the Schrödinger equation for one-electron systems exactly, we assume

a many-electron wavefunction Ψ to have a general form of the product of one-electron wavefunctions ϕ

$$\Psi(\mathbf{x}_1, \mathbf{x}_2, \cdots \mathbf{x}_N) = \phi(\mathbf{x}_1)\phi(\mathbf{x}_2)\cdots\phi(\mathbf{x}_N) \tag{2.6}$$

This is known as the *Hartree product*. It assumes that the electrons in a many-electron system do not interact with each other. Expressing a many-electron wavefunction using an independent-particle model is a crude approximation. Importantly, the Hartree product does not satisfy the Pauli exclusion principle. A wavefunction, when expressed as a determinant of spin orbitals, satisfies the antisymmetry principle. Such a wavefunction is known as a *Slater determinant*

$$\Psi(\mathbf{x}_1, \mathbf{x}_2, \cdots, \mathbf{x}_N) = \frac{1}{\sqrt{N!}} \begin{vmatrix} \chi_1(\mathbf{x}_1) & \chi_2(\mathbf{x}_1) & \cdots & \chi_N(\mathbf{x}_1) \\ \chi_1(\mathbf{x}_2) & \chi_2(\mathbf{x}_2) & \cdots & \chi_N(\mathbf{x}_2) \\ \vdots & \vdots & & \vdots \\ \chi_1(\mathbf{x}_N) & \chi_2(\mathbf{x}_N) & \cdots & \chi_N(\mathbf{x}_N) \end{vmatrix} \tag{2.7}$$

where $\frac{1}{\sqrt{N!}}$ is a normalisation factor, and the N electrons occupy N *spin orbitals* $(\chi_i, \chi_j, \cdots \chi_k)$. A spin orbital is a one-electron wavefunction that describes both the spatial and spin coordinates of an electron. It is obtained by multiplying a *spatial orbital* $\psi(\mathbf{r})$ by one of the two possible spin functions-α or β. Thus, for a given set of M spatial orbitals $\{\psi\}$, we get $2M$ spin orbitals $\{\chi\}$. Consequently, a spatial orbital can have a maximum occupancy of two electrons, while a maximum of one electron can occupy a spin orbital.

$$\chi(\mathbf{x}) = \begin{cases} \psi(\mathbf{r})\alpha : \text{spin-up} \\ \psi(\mathbf{r})\beta : \text{spin-down} \end{cases} \tag{2.8}$$

Interchanging two rows in a Slater determinant changes the sign of the total wavefunction. This preserves the antisymmetry of the N-electron wavefunction under the exchange of two electrons. When two electrons occupy the same spin orbital, it corresponds to two columns being identical, which makes the determinant zero. This property satisfies the Pauli exclusion principle, ensuring that no two electrons can occupy the same spin orbital simultaneously. For convenience, a Slater determinant is expressed concisely using only the diagonal elements as

$$\Psi(\mathbf{x}_1, \mathbf{x}_2, \cdots, \mathbf{x}_N) = |\chi_1(\mathbf{x}_1)\chi_2(\mathbf{x}_2)\cdots\chi_N(\mathbf{x}_N)\rangle \tag{2.9}$$

If the ordering of the electron labels is always chosen to be $\mathbf{x}_1, \mathbf{x}_2 \cdots \mathbf{x}_N$, then the above expression can be further shortened to be

$$\Psi(\mathbf{x}_1, \mathbf{x}_2, \cdots, \mathbf{x}_N) = |\chi_1 \chi_2 \cdots \chi_N\rangle \tag{2.10}$$

Generally, Slater determinants are eigenfunctions of the spin-projection operator S_z but not of the total spin operator S^2. They are simultaneous eigenfunctions of S_z and S^2 when the spin quantum number $M_s = \pm S$. Thus, determinants corresponding to closed-shell singlet configurations ($S = M_s = 0$) are eigenfunctions of both S_z and S^2.

Matrix elements for one or two-electron operators between Slater determinants can be evaluated using the following rules based on the difference between the two determinants

$$\left\langle \Psi_1 \left| \sum_i^N \hat{h}(i) \right| \Psi_2 \right\rangle = \begin{cases} \sum_p^N \left\langle \chi_p \middle| \hat{h} \middle| \chi_p \right\rangle, \text{ if } \Psi_1 = \left| \cdots \chi_a \chi_p \cdots \chi_b \chi_q \cdots \right\rangle = \Psi_2 \\ \left\langle \chi_p \middle| \hat{h} \middle| \chi_r \right\rangle, \text{ if } \Psi_1 = \left| \cdots \chi_a \chi_p \cdots \chi_b \chi_q \cdots \right\rangle, \Psi_2 = \left| \cdots \chi_a \chi_r \cdots \chi_b \chi_q \cdots \right\rangle \\ 0 \text{ otherwise} \end{cases} \tag{2.11}$$

where the one-electron operator $\hat{h}(i) = -\frac{1}{2}\nabla_i^2 - \sum_A^M \frac{Z_A}{r_{iA}}$. The matrix elements for two-electron operators such as the Coulomb repulsion operator, $\sum_i^N \sum_{j>i}^N r_{ij}^{-1}$, are evaluated as

$$\left\langle \Psi_1 \left| \sum_i^N \sum_{j>i}^N r_{ij}^{-1} \right| \Psi_2 \right\rangle = \begin{cases} \frac{1}{2} \sum_p^N \sum_q^N \left\langle \chi_p \chi_q \middle\| \chi_p \chi_q \right\rangle, \text{ if } \Psi_1 = \left| \cdots \chi_a \chi_p \cdots \chi_b \chi_q \cdots \right\rangle = \Psi_2 \\ \sum_q^N \left\langle \chi_p \chi_q \middle\| \chi_r \chi_q \right\rangle, \text{ if } \Psi_1 = \left| \cdots \chi_a \chi_p \cdots \chi_b \chi_q \cdots \right\rangle, \Psi_2 = \left| \cdots \chi_a \chi_r \cdots \chi_b \chi_q \cdots \right\rangle \\ \left\langle \chi_p \chi_q \middle\| \chi_r \chi_s \right\rangle, \text{ if } \Psi_1 = \left| \cdots \chi_a \chi_p \cdots \chi_b \chi_q \cdots \right\rangle, \Psi_2 = |\cdots \chi_a \chi_r \cdots \chi_b \chi_s \cdots\rangle \\ 0 \text{ otherwise} \end{cases} \tag{2.12}$$

where $\left\langle \chi_p \chi_q \middle\| \chi_r \chi_s \right\rangle \equiv \langle pq \| rs \rangle = \left\langle pq \middle| r_{ij}^{-1} \middle| rs \right\rangle - \left\langle pq \middle| r_{ij}^{-1} \middle| sr \right\rangle$. Henceforth, we may also use the shorthand notation $\left\langle pq \middle| r_{ij}^{-1} \middle| rs \right\rangle \equiv \langle pq | rs \rangle$. An electron-electron repulsion integral over spin orbitals is fully expressed as

$$\langle pq | rs \rangle = \int d\mathbf{x}_1 d\mathbf{x}_2 \chi_p^*(\mathbf{x}_1) \chi_q^*(\mathbf{x}_2) \frac{1}{r_{12}} \chi_r(\mathbf{x}_1) \chi_s(\mathbf{x}_2) \tag{2.13}$$

Occasionally, we use the so-called Chemist's notation for expressing matrix elements over spatial orbitals $\{\psi_p(\mathbf{r})\}$, specifically, for electron-electron repulsion integrals:

$$(pq|rs) = \int d\mathbf{r}_1 d\mathbf{r}_2 \psi_p^*(\mathbf{r}_1)\psi_q(\mathbf{r}_1)\frac{1}{r_{12}}\psi_r^*(\mathbf{r}_2)\psi_s(\mathbf{r}_2) \tag{2.14}$$

2.2 The Hartree-Fock Theory

The HF theory provides a mean-field solution to the Schrödinger equation. The HF Hamiltonian is the many-electron Fock operator $\hat{F}$ given by the sum of one-electron Fock operators $\hat{f}(i)$

$$\hat{F} = \sum_i^N \hat{f}(i) \tag{2.15}$$

The Fock operator $\hat{f}(1)$ for a single electron (chosen to be electron 1) is a sum of one-electron core Hamiltonian $\hat{h}(1)$, and the HF potential $\hat{v}_{HF}$ which is given by the sum of coulomb $\hat{J}(1)$ and exchange $\hat{K}(1)$ terms.

$$\hat{f}(1) = \hat{h}(1) + \hat{v}_{HF}(1) \tag{2.16}$$

$$\hat{v}_{HF}(1) = \sum_j \left(\hat{J}_j(1) - \hat{K}_j(1)\right) \tag{2.17}$$

The one-electron Hamiltonian $\hat{h}(1)$ is constituted by the kinetic energy and the electron-nuclei potential

$$\hat{h}(1) = -\frac{1}{2}\nabla_1^2 - \sum_A^M \frac{Z_A}{r_{1A}} \tag{2.18}$$

The corresponding one-electron integrals are given as

$$h_{ii} = \left\langle \chi_i \middle| \hat{h}(1) \middle| \chi_j \right\rangle = \langle i|\hat{h}|j\rangle \tag{2.19}$$

The Coulomb and exchange operators are defined by their action on a spin orbital

$$\hat{J}_j(1)\chi_i(\mathbf{x}_1) = \int d\mathbf{x}_2 \chi_j^*(\mathbf{x}_2)\frac{1}{r_{12}}\chi_j(\mathbf{x}_2)\chi_i(\mathbf{x}_1) \tag{2.20}$$

$$\hat{K}_j(1)\chi_i(\mathbf{x}_1) = \int d\mathbf{x}_2 \chi_j^*(\mathbf{x}_2)\frac{1}{r_{12}}\chi_i(\mathbf{x}_2)\chi_j(\mathbf{x}_1) \tag{2.21}$$

where $\mathbf{x}_1$ denotes the combined spin and spatial coordinates of electron 1 and the corresponding Coulomb and exchange integrals can be evaluated as

$$J_{ij} = \langle ij|ij\rangle = \int d\mathbf{x}_1 d\mathbf{x}_2 \chi_i^*(\mathbf{x}_1)\chi_i(\mathbf{x}_1)\frac{1}{r_{12}}\chi_j^*(\mathbf{x}_2)\chi_j(\mathbf{x}_2). \tag{2.22}$$

$$K_{ij} = \langle ij|ji\rangle = \int d\mathbf{x}_1 d\mathbf{x}_2 \chi_i^*(\mathbf{x}_1)\chi_j(\mathbf{x}_1)\frac{1}{r_{12}}\chi_j^*(\mathbf{x}_2)\chi_i(\mathbf{x}_2). \tag{2.23}$$

$$J_{ij} - K_{ij} = \langle ij|ij\rangle - \langle ij|ji\rangle = \langle ij||ij\rangle \tag{2.24}$$

Here, in the *Dirac bra-ket* notation, the spin orbitals χ_i and χ_j have been denoted using a shorthand notation of i and j respectively.

$\hat{v}_{HF}$ describes the two-electron interactions in an average way, and thus it is effectively a one-electron potential. Formally, the HF equations are obtained as stationary conditions for varying the orbitals such that the total energy is minimised under the constraint of orthonormality of orbitals. This leads to HF equations being eigenvalue equations with the effective one-electron operators—the single-electron Fock operators. For example, the HF equation for electron 1, occupying canonical spin orbital $\chi_i(\mathbf{x}_1)$ is given as

$$\hat{f}(1)\chi_i(\mathbf{x}_1) = \varepsilon_i\chi_i(\mathbf{x}_1) \tag{2.25}$$

where ε_i and χ_i are the eigenvalue and the eigenvector, respectively. The solutions to the HF equations are obtained by employing the *variational principle* which involves minimising the energy functional for a single Slater determinant $\Psi = |\chi_1, \chi_2, \cdots, \chi_N\rangle$ with respect to the spin orbitals such that they remain orthonormal

$$E_{HF} = \left\langle \Psi \middle| \hat{H}_{el} \middle| \Psi \right\rangle ; \langle \chi_a|\chi_b\rangle = \delta_{ab} \tag{2.26}$$

The energy of a single orbital in a closed-shell system then becomes

$$\varepsilon_i = f_{ii} = h_{ii} + \sum_j^N \left(2J_{ij} - K_{ij}\right) \tag{2.27}$$

and the total closed-shell HF energy can be expressed as

$$E_{HF} = \sum_{i}^{N} h_{ii} + \frac{1}{2} \sum_{ij}^{N} \left(2J_{ij} - K_{ij}\right) + E_{nuc} \tag{2.28}$$

where E_{nuc} is the constant that corresponds to the nuclear-nuclear repulsion term.

2.2.1 Brillouin's Theorem and Canonical Orbitals

The N spin orbitals that minimise the energy functional in Equation (2.26) constitute the optimised HF Slater determinant or the HF wavefunction. In the typical situation where the number of spin orbitals exceeds the number of electrons, the space can be divided into *occupied* or *internal* space and *virtual* or *external* space. Since the HF wavefunction is formed by the occupied orbitals, the virtual orbitals do not contribute to the HF energy E_{HF}. Finding the N lowest energy spin orbitals is equivalent to block diagonalising the *Fock* matrix such that the occupied $\{i\}$ and virtual $\{a\}$ spaces do not mix with each other, $F_{ia} = \langle \chi_i | \hat{F} | \chi_a \rangle = 0$. Replacing an occupied orbital by a virtual orbital is known as the excitation of a single electron from a lower energy orbital i to a higher energy orbital a. Since the optimisation of the HF wavefunction requires that $F_{ia} = 0$, such single excitations do not contribute to the HF energy. This is known as Brillouin's theorem, and it is a direct consequence of the *variational principle*, which is used for minimising energy. In the special case where the Fock matrix is diagonal, the optimised spin orbitals are known as the *canonical orbitals* and the corresponding eigenvalues are the orbital energies. The canonical solution to the HF equations is widely popular because the difference between the two orbital energies is observable as the electronic transition frequency.

2.2.2 The Basis Set Approximation

To obtain numerical solutions for Equation (2.25), we introduce a basis set consisting of K known basis functions $\{\mu(\mathbf{x}_i)\}$, simply referred to as atomic orbitals, which expand the spin orbitals as a linear combination

$$\chi_i(\mathbf{x}_1) = \sum_{\mu}^{K} C_{\mu i}\, \mu(\mathbf{x}_1) \tag{2.29}$$

where $C_{\mu i}$ are the coefficients of expansion. Equation (2.25) now becomes

$$\hat{f}(1)\sum_{\nu=1}^{K} C_{\nu i}\nu(\mathbf{x}_1) = \varepsilon_i \sum_{\nu=1}^{K} C_{\nu i}\nu(\mathbf{x}_1) \tag{2.30}$$

Multiplying by $\mu^*(\mathbf{x}_1)$ from the left, and integrating gives the equation known as the Roothan equation

$$\sum_{\nu=1}^{K} C_{\nu i}\int d\mathbf{x}_1\mu^*(\mathbf{x}_1)\hat{f}(1)\nu(\mathbf{x}_1) = \varepsilon_i \sum_{\nu=1}^{K} C_{\nu i}\int d\mathbf{x}_1\mu^*(\mathbf{x}_1)\nu(\mathbf{x}_1) \tag{2.31}$$

which can be written in matrix form as

$$\mathbf{FC} = \varepsilon\mathbf{SC} \tag{2.32}$$

with the Fock matrix elements expressed as $F_{\mu\nu} = \int d\mathbf{x}_1\mu^*(\mathbf{x}_1)\hat{f}(1)\nu(\mathbf{x}_1)$ and the overlap matrix elements as $S_{\mu\nu} = \int d\mathbf{x}_1\mu^*(\mathbf{x}_1)\nu(\mathbf{x}_1)$. The various contributions to the Fock matrix are the kinetic energy of electrons **T**, electron-nuclei attraction potential **Z**, coulomb repulsion between electrons **J** and the exchange term **K** arising out of the antisymmetry requirement

$$F_{\mu\nu} = T_{\mu\nu} + Z_{\mu\nu} + J_{\mu\nu} + K_{\mu\nu} \tag{2.33}$$

Thus, we obtain a generalised eigenvalue problem (Equation (2.32)) that is solved by transforming to an orthogonal basis and then iterating until self-consistency is reached, starting with guessed trial expansions for the spin orbitals.

2.3 Orbital Rotations

A new set of spin orbitals $\{\chi'_a\}$ can be obtained by applying a unitary transformation **U** on the original set $\{\chi_a\}$, so that the new set of spin orbitals then constitute a new wavefunction $|\Psi'\rangle$ which differs from the original wavefunction $|\Psi\rangle$ only by a phase factor $e^{i\phi}$.

$$\chi'_a = \sum_b U_{ba}\chi_b \tag{2.34}$$

where U_{ba} are the elements of the unitary matrix $\mathbf{U}$. Since $\mathbf{U}^\dagger\mathbf{U} = \mathbf{1}$,

$$|\Psi'\rangle = \det(\mathbf{U})\,|\Psi\rangle = e^{i\phi}\,|\Psi\rangle \tag{2.35}$$

Since all observable properties depend on $|\Psi|^2$, any expectation value remains stable with respect to arbitrary unitary transformations of the spin orbitals. Thus, the energy corresponding to a single determinant wavefunction, such as the HF wavefunction, is invariant with respect to orbital rotations through unitary transformations. Therefore, the canonical orbitals are not a unique solution to the HF equations, and other types of unitarily equivalent orbitals can be employed for different purposes.

2.4 Natural Orbitals

A set of generalised density matrices can be used to calculate the expectation values of physical quantities that involve many-body interactions. Given an N-electron system described by a normalised wavefunction Ψ, the probability of finding an electron in volume element $d\mathbf{x}_1$, while simultaneously finding another electron in $d\mathbf{x}_2$, and so on is expressed as $\Psi^*(\mathbf{x}_1, \mathbf{x}_2, \cdots, \mathbf{x}_N)\Psi(\mathbf{x}_1, \mathbf{x}_2, \cdots, \mathbf{x}_N)d\mathbf{x}_1 d\mathbf{x}_2 \cdots d\mathbf{x}_N$. The *first-order reduced density matrix*, also known as the one-electron reduced density matrix γ, is given as

$$\begin{aligned}\gamma(\mathbf{x'}_1|\mathbf{x}_1) &= N \int \Psi^*(\mathbf{x'}_1, \mathbf{x}_2, \cdots, \mathbf{x}_N)\Psi(\mathbf{x}_1, \mathbf{x}_2, \cdots, \mathbf{x}_N)d\mathbf{x}_2 \cdots d\mathbf{x}_N \\ &= \sum_{p,q} \chi_p^*(\mathbf{x'}_1)\chi_q(\mathbf{x}_1)\gamma_{pq}\end{aligned} \tag{2.36}$$

where the right-hand side expresses the first-order reduced density matrix in an orthonormal spin orbital basis, and γ_{pq} are the coefficients of expansion in the given basis. The diagonal elements of the above matrix provide the probability of finding an electron in a given volume element, independent of the location of all the other electrons

$$\rho(\mathbf{x}_1) = \gamma(\mathbf{x}_1|\mathbf{x}_1) = N \int \Psi^*(\mathbf{x}_1, \mathbf{x}_2, \cdots, \mathbf{x}_N)\Psi(\mathbf{x}_1, \mathbf{x}_2, \cdots, \mathbf{x}_N)d\mathbf{x}_2 \cdots d\mathbf{x}_N \tag{2.37}$$

Similarly, the two-electron or the *second-order reduced density matrix* is given as

$$\begin{aligned}\gamma(\mathbf{x'}_1, \mathbf{x'}_2|\mathbf{x}_1, \mathbf{x}_2) &= N(N-1)\int \Psi^*(\mathbf{x'}_1, \mathbf{x'}_2, \cdots, \mathbf{x}_N)\Psi(\mathbf{x}_1, \mathbf{x}_2, \cdots, \mathbf{x}_N)d\mathbf{x_3}\cdots d\mathbf{x}_N \\ &= \sum_{p,q,r,s} \chi_p^*(\mathbf{x'}_1)\chi_r^*(\mathbf{x'}_2)\chi_q(\mathbf{x}_1)\chi_s(\mathbf{x}_2)\gamma_{pqrs}\end{aligned} \tag{2.38}$$

Higher-order density matrices can be similarly defined. These reduced density matrices are Hermitian and antisymmetric with respect to the sets of electronic indices. The average values of various operators can then be expressed using the reduced density matrices. For example, the expectation value of a HF determinant can be expressed in terms of the first and second-order reduced density matrices as

$$E_{HF} = \left\langle \Psi \middle| \hat{H}_{el} \middle| \Psi \right\rangle = \sum_{p,q} h_{pq}\gamma_{pq} + \frac{1}{2}\sum_{pqrs} g_{pqrs}\gamma_{pqrs} \tag{2.39}$$

where h_{pq} and g_{pqrs} are one and two-electron matrix elements, respectively, which can be evaluated using Equation (2.11) and Equation (2.12). In the special case of the single-determinantal HF wavefunction, the first-order reduced density matrix is diagonal,

$$\gamma^{HF}(\mathbf{x'}_1|\mathbf{x}_1) = \sum_i \chi_i^*(\mathbf{x'}_1)\chi_i(\mathbf{x}_1). \tag{2.40}$$

In general, the first-order reduced density matrix is not diagonal; however, since it is Hermitian, it is possible to find a unitary transformation which transforms the first-order matrix into a diagonal form. The orthonormal elements of the diagonalised one-electron reduced density matrix are called natural spin orbitals or, more commonly, natural orbitals ψ_k

$$\psi_k = \sum_a \chi_a U_{ka} \tag{2.41}$$

$$\mathbf{U}^\dagger\boldsymbol{\gamma}\mathbf{U} = \lambda \quad \text{such that} \quad \lambda_{ij} = \delta_{ij}\lambda_i \tag{2.42}$$

The eigenvalues λ represent the average number of electrons in each natural orbital and can therefore be interpreted as the occupation numbers of the natural orbitals. Introduced by Löwdin in 1955, natural orbitals provide the most rapid convergence of a CI wavefunction expansion[83]. The configuration space formed by natural orbitals can be truncated based on their occupation numbers, as only those with large occupations contribute significantly to the

energy.

2.5 Many-Body Perturbation Theory

The HF theory successfully predicts the electronic structure in many cases; however, it sometimes fails remarkably. The most well-known example is probably the failure of restricted HF in describing the dissociation of molecules into open-shell fragments. Although unrestricted HF provides a qualitatively correct picture in many cases, it often fails to yield accurate potential energy surfaces. The reason for this is that while HF exactly accounts for *Fermi correlation* arising from the antisymmetry of electrons, it only describes an electron as moving in the average potential of all the other electrons, thus neglecting the correlation due to many-body interactions. The energy due to this neglected effect is known as the *correlation energy*, and is defined as the difference between the exact non-relativistic energy E_{exact} of the system and the HF energy E_{HF}, both obtained in the complete basis set limit.

$$E_{corr} = E_{exact} - E_{HF} \tag{2.43}$$

Electron correlation accounts for the correlated motion of electrons, which reduces the system's energy by reducing electron-electron repulsion. The correlation energy is thus negative, and, therefore, the HF energy is always an upper bound to the exact energy. One of the simplest approaches to recover the missing correlation is perturbation theory. In this section, we discuss important aspects of the most useful form of perturbation theory, a widely employed post-HF method for capturing electron correlation effects.

One of the most general and useful formulation of time-independent many-body perturbation theory is provided by the Rayleigh-Schrödinger perturbation theory. We assume that the system of interest can be described reasonably accurately using a reference unperturbed Hamiltonian $\hat{H}_0$, and its corresponding wavefunction $\left|\psi^{(0)}_{ref}\right\rangle$, so that the Hamiltonian operator can be decomposed into two components as

$$\hat{H} = \hat{H}_0 + \lambda\hat{U} \tag{2.44}$$

where $\hat{U}$ represents a weak perturbing Hamiltonian. The parameter λ quantifies the strength of the perturbation, ranging from 0 (no perturbation) to 1 (fully perturbed). Thus, we get the

eigenvalue problem

$$\hat{H}\,|\Phi_i\rangle = (\hat{H}_0 + \lambda\hat{U})\,|\Phi_i\rangle = \varepsilon_i\,|\Phi_i\rangle \tag{2.45}$$

The eigenfunctions, $\left|\psi_i^{(0)}\right\rangle \equiv \left|i^{(0)}\right\rangle$, and the eigenvalues $\epsilon_i^{(0)}$ of $\hat{H}_0$ are known. The eigenfunctions are orthonormal

$$\hat{H}_0\left|i^{(0)}\right\rangle = \epsilon_i^{(0)}\left|i^{(0)}\right\rangle \tag{2.46}$$

$$\left\langle m^{(0)}\middle|\, n^{(0)}\right\rangle = \delta_{mn} \tag{2.47}$$

We are interested in obtaining approximations to the exact ground state solution $|\Phi_0\rangle$ and the corresponding eigenvalue ε_0 to Equation (2.45). The exact eigenfunctions $|\Phi_i\rangle$ and eigenvalues ε_i can be expanded in a power series in λ such that we can systematically improve upon the eigenfunctions and eigenvalues of $\hat{H}_0$

$$|\Phi_i\rangle = \left|i^{(0)}\right\rangle + \lambda\left|i^{(1)}\right\rangle + \lambda^2\left|i^{(2)}\right\rangle + \ldots \tag{2.48}$$

$$\varepsilon_i = \epsilon_i^{(0)} + \lambda\epsilon_i^{(1)} + \lambda^2\epsilon_i^{(2)} + \ldots \tag{2.49}$$

We refer to $\left|i^{(n)}\right\rangle$ as the nth-order wavefunction and $\epsilon_i^{(n)}$ as the nth-order energy. Since we only know the zeroth-order wavefunction and energy, the problem translates to expressing the nth-order quantities in terms of the zeroth-order quantities and the perturbation $\hat{U}$. For convenience, we impose intermediate normalisation between the zeroth-order and the exact wavefunction.

$$\left\langle i^{(0)}\middle|\,\Phi_i\right\rangle = \left\langle i^{(0)}\middle|\, i^{(0)}\right\rangle + \lambda\left\langle i^{(0)}\middle|\, i^{(1)}\right\rangle + \lambda^2\left\langle i^{(0)}\middle|\, i^{(2)}\right\rangle + \ldots = 1 \tag{2.50}$$

Since the above equation holds for all values of λ, equality of coefficients of λ^n on both sides implies orthogonality between the zeroth-order wavefunction and every nth-order wavefunction. This is known as intermediate normalisation.

$$\left\langle i^{(0)}\middle|\, i^{(n)}\right\rangle = \delta_{n0} \tag{2.51}$$

A general equation for the nth-order perturbation can be derived by substituting Equation (2.48) in Equation (2.45), and subsequently equating coefficients of λ^n

$$(\hat{H}_0 - \epsilon_i^{(0)})\left|i^{(n)}\right\rangle = -\hat{U}\left|i^{(n-1)}\right\rangle + \sum_{k=1}^{n}\epsilon_i^{(k)}\left|i^{(n-k)}\right\rangle \quad ; \quad n > 0 \tag{2.52}$$

The above equation represents the residual of the zeroth-order Schrödinger equation with respect to the nth-order wavefunction in terms of all lower-order wavefunctions. Thus, this equation can be applied recursively to generate higher-order corrections to the wavefunction. The zeroth-order perturbation is given by Equation (2.46) while the first to third-order perturbations are explicitly given as

$$(\hat{H}_0 - \epsilon_i^{(0)}) \left|i^{(1)}\right\rangle = -\hat{U} \left|i^{(0)}\right\rangle + \epsilon_i^{(1)} \left|i^{(0)}\right\rangle \tag{2.53}$$

$$(\hat{H}_0 - \epsilon_i^{(0)}) \left|i^{(2)}\right\rangle = -\hat{U} \left|i^{(1)}\right\rangle + \epsilon_i^{(1)} \left|i^{(1)}\right\rangle + \epsilon_i^{(2)} \left|i^{(0)}\right\rangle \tag{2.54}$$

$$(\hat{H}_0 - \epsilon_i^{(0)}) \left|i^{(3)}\right\rangle = -\hat{U} \left|i^{(2)}\right\rangle + \epsilon_i^{(1)} \left|i^{(2)}\right\rangle + \epsilon_i^{(2)} \left|i^{(1)}\right\rangle + \epsilon_i^{(3)} \left|i^{(0)}\right\rangle \tag{2.55}$$

By left multiplying Equation (2.52) by $\left|i^{(0)}\right\rangle$, then using the orthogonality relation in Equation (2.51) we see that the nth-order correction to the energy can be expressed as a matrix element of the perturbation operator $\hat{U}$ between the zeroth-order and the $(n-1)$th-order wavefunction

$$\epsilon_i^{(n)} = \left\langle i^{(0)} \middle| \hat{U} \middle| i^{(n-1)} \right\rangle \quad ; \quad n > 0 \tag{2.56}$$

The explicit expressions for the zeroth to third-order energies are

$$\epsilon_i^{(0)} = \left\langle i^{(0)} \middle| \hat{H}_0 \middle| i^{(0)} \right\rangle \tag{2.57}$$

$$\epsilon_i^{(1)} = \left\langle i^{(0)} \middle| \hat{U} \middle| i^{(0)} \right\rangle \tag{2.58}$$

$$\epsilon_i^{(2)} = \left\langle i^{(0)} \middle| \hat{U} \middle| i^{(1)} \right\rangle \tag{2.59}$$

$$\epsilon_i^{(3)} = \left\langle i^{(0)} \middle| \hat{U} \middle| i^{(2)} \right\rangle \tag{2.60}$$

Thus, the nth-order energy can be determined by the $(n-1)$th wavefunction. For example, the first-order energy $\epsilon_i^{(1)}$ can be obtained by applying the perturbing Hamiltonian to the zeroth-order wavefunctions, and the zeroth and first-order wavefunctions are sufficient to calculate the second-order energy. For the third and higher-order energies, a computationally more efficient formulation is possible, which allows for the calculation of the energy of order $2n+1$ using wavefunctions of order n and lower. This is known as Wigner's $2n+1$ rule[84]. This work is limited to determining the second-order energy correction; therefore we restrict the discussion to the determination of the first-order wavefunction.

Assuming a complete set of eigenfunctions are known for $\hat{H}_0$, $\left|i^{(1)}\right\rangle$ can be expanded as a linear

combination of those eigenfunctions

$$\left|i^{(1)}\right\rangle = \sum_n a_n^{(1)} \left|n^{(0)}\right\rangle \tag{2.61}$$

The expansion coefficients $a_n^{(1)}$ are referred to as amplitudes. The eigenfunctions $\left|n^{(0)}\right\rangle$ are excited configurations generated from the ground state reference wavefunction $\left|\psi_{ref}^{(0)}\right\rangle$. By multiplying Equation (2.61) by $\left\langle n^{(0)}\right|$ and using the orthonormality of the eigenfunctions of $\hat{H}_0$

$$a_n^{(1)} = \left\langle n^{(0)} \middle| i^{(1)} \right\rangle \tag{2.62}$$

Using Equation (2.61) and Equation (2.62) in the second-order energy expression in Equation (2.59), we get

$$\epsilon_i^{(2)} = \sum_{n \neq i} \left\langle i^{(0)} \middle| \hat{U} \middle| n^{(0)} \right\rangle \left\langle n^{(0)} \middle| i^{(1)} \right\rangle = \sum_{n \neq i} a_n^{(1)} \left\langle i^{(0)} \middle| \hat{U} \middle| n^{(0)} \right\rangle \tag{2.63}$$

Multiplying Equation (2.53) by $\left\langle n^{(0)}\right|$, and using the orthogonality of the zeroth-order wavefunctions, the first-order amplitudes can be expressed as

$$\begin{aligned} \left\langle n^{(0)} \middle| \hat{H}_0 - \epsilon_i^{(0)} \middle| i^{(1)} \right\rangle &= -\left\langle n^{(0)} \middle| \hat{U} \middle| i^{(0)} \right\rangle \\ (\epsilon_n^{(0)} - \epsilon_i^{(0)}) \left\langle n^{(0)} \middle| i^{(1)} \right\rangle &= -\left\langle n^{(0)} \middle| \hat{U} \middle| i^{(0)} \right\rangle \\ a_n^{(1)} &= \frac{\left\langle n^{(0)} \middle| \hat{U} \middle| i^{(0)} \right\rangle}{\epsilon_i^{(0)} - \epsilon_n^{(0)}} \end{aligned} \tag{2.64}$$

Substituting Equation (2.64) in Equation (2.63), we finally get

$$\epsilon_i^{(2)} = \sum_{n \neq i} \frac{\left\langle n^{(0)} \middle| \hat{U} \middle| i^{(0)} \right\rangle \left\langle i^{(0)} \middle| \hat{U} \middle| n^{(0)} \right\rangle}{\epsilon_i^{(0)} - \epsilon_n^{(0)}} = \sum_{n \neq i} \frac{\left| \left\langle i^{(0)} \middle| \hat{U} \middle| n^{(0)} \right\rangle \right|^2}{\epsilon_i^{(0)} - \epsilon_n^{(0)}} \tag{2.65}$$

Similarly, by expanding higher-order wavefunctions, we can obtain the general expressions for higher-order perturbation energies. For our purposes, the expressions up to second-order are sufficient.

2.6 Second-Order Møller-Plesset Perturbation Theory (MP2)

The success of many-body perturbation theory depends on a suitable zeroth-order Hamiltonian $\hat{H}_0$. In the instances where the exact wavefunction can be adequately approximated by a single Slater determinant *i.e.* systems with small static correlation contributions, the HF wavefunction provides a reliable mean-field approximation to the exact wavefunction. Therefore, the HF Hamiltonian, given by the Fock operator defined in Equation (2.15), serves as a suitable $\hat{H}_0$ in Equation (2.44). In the framework of the Fock operator serving as the zeroth-order Hamiltonian, the theory is recognised as Møller-Plesset Perturbation Theory (MPPT). The Fock operator for a system of N electrons is expressed as

$$\hat{H}_0 \equiv \hat{F} = \sum_i^N \hat{f}_i = \sum_i^N \hat{h}(i) + \sum_i^N \sum_p^N \left[\hat{J}_p(i) - \hat{K}_p(i)\right] \tag{2.66}$$

Thus, the zeroth-order wavefunction in MPPT is the HF Slater determinant, and the zeroth-order energy $E_{MP}^{(0)}$ is simply the sum of energies ε_i of all occupied MOs

$$E_{MP}^{(0)} = \sum_i^N \varepsilon_i \tag{2.67}$$

We recall that the Fock operator describes the motion of an electron in an average field of other electrons, thus it is effectively a one-electron operator. In the MPPT framework, the perturbation operator can be described as a fluctuation in the average field of the other electrons, and is referred to as the *fluctuation potential*. Since the exact Hamiltonian, $\hat{H}_{el}$, describes the coulomb interaction between two electrons as an instantaneous electron-electron interaction, the perturbation operator $\hat{U}_{MP}$ is defined as the difference between the instantaneous electron-electron interactions and the HF mean-field potential.

$$\hat{H}_{el} = \sum_i^N \hat{h}(i) + \sum_i^N \sum_{j>i}^N \frac{1}{r_{ij}} \tag{2.68}$$

$$\begin{aligned} \hat{U}_{MP} &= \hat{H}_{el} - \hat{F} \\ \hat{U}_{MP} &= \sum_i^N \sum_{j>i}^N \frac{1}{r_{ij}} - \sum_i^N \sum_p^N \left[\hat{J}_p(i) - \hat{K}_p(i)\right] \end{aligned} \tag{2.69}$$

The Coulomb $\hat{J}_p(i)$ and exchange $\hat{K}_p(i)$ operators are defined in Equation (2.20) and Equation (2.21), respectively. According to Equation (2.58), the first-order energy is expressed using the HF ground state, $|\psi_{HF}\rangle$, as the zeroth-order wavefunction can be evaluated using Equation (2.12) and Equation (2.24) as

$$\begin{aligned} E_{MP}^{(1)} &= \left\langle \psi_{HF} \left| \sum_{i}^{N} \sum_{j>i}^{N} \frac{1}{r_{ij}} \right| \psi_{HF} \right\rangle - \left\langle \psi_{HF} \left| \sum_{i}^{N} \sum_{p}^{N} [\hat{J}_p(i) - \hat{K}_p(i)] \right| \psi_{HF} \right\rangle \\ &= \frac{1}{2} \sum_{i}^{N} \sum_{j}^{N} \langle ij||ij\rangle - \sum_{p}^{N} \sum_{q}^{N} \langle pq||pq\rangle \\ &= -\frac{1}{2} \sum_{i}^{N} \sum_{j}^{N} \langle ij||ij\rangle \end{aligned} \tag{2.70}$$

where we have used the fact that i and j, as well as p and q are dummy indices for orbitals occupied by electrons i and j respectively. The MP perturbation energy up to first-order, E_{MP1}, can be evaluated with the help of Equation (2.27) and Equation (2.70)

$$\begin{aligned} E_{MP1} &= E_{MP}^{(0)} + E_{MP}^{(1)} \\ &= \sum_{i}^{N} \varepsilon_i - \frac{1}{2} \sum_{i}^{N} \sum_{j}^{N} \langle ij||ij\rangle \\ &= \sum_{i}^{N} \left(\left\langle i \left| \hat{h} \right| i \right\rangle + \sum_{j}^{N} \langle ij||ij\rangle \right) - \frac{1}{2} \sum_{i}^{N} \sum_{j}^{N} \langle ij||ij\rangle \\ &= \sum_{i}^{N} \left\langle i \left| \hat{h} \right| i \right\rangle + \frac{1}{2} \sum_{i}^{N} \sum_{j}^{N} \langle ij||ij\rangle \\ E_{MP1} &= E_{HF} \end{aligned} \tag{2.71}$$

Hence, the sum of the zeroth- and first-order perturbation corrections yields exactly the HF energy. This means that the first correction to the HF energy is only obtained using second-order perturbation theory.

The expression for the second-order perturbation correction derived in Equation (2.65) involves the first-order wavefunction. The first-order wavefunction in Equation (2.61) is spanned by the excited determinants $\{|\psi_e\rangle\}$ generated from the HF ground state wavefunction,

$$\left|\Phi_0^{(1)}\right\rangle = \sum_{e\neq 0} a_e^{(1)} |\psi_e\rangle \tag{2.72}$$

where $a_e^{(1)}$ are the amplitudes for the expansion of the first-order wavefunction, $\left|\Phi_0^{(1)}\right\rangle$. The excited determinants can be classified and grouped together according to the degree of excitation

$$\left|\Phi_0^{(1)}\right\rangle = \sum_{ia} t_a^{i(1)} \left|\psi_i^a\right\rangle + \sum_{\substack{i<j,\\ a<b}} t_{ab}^{ij(1)} \left|\psi_{ij}^{ab}\right\rangle + \sum_{\substack{i<j<k,\\ a<b<c}} t_{abc}^{ijk(1)} \left|\psi_{ijk}^{abc}\right\rangle + \dots \tag{2.73}$$

In the above equation, the amplitudes and determinants corresponding to a single excitation $i \rightarrow a$ of an electron from orbital i to a are denoted as $t_a^{i(1)}$ and $\left|\psi_i^a\right\rangle$, respectively. Similarly, double excitations $i \rightarrow a \wedge j \rightarrow b$ are expressed using amplitudes $t_{ab}^{ij(1)}$ and determinants $\left|\psi_{ij}^{ab}\right\rangle$, and so on. Like the reference ground state determinant $|\psi_{HF}\rangle$, the excited determinants are eigenfunctions of the Fock operator. For example,

$$\hat{F}\left|\psi_i^a\right\rangle = \left(E_{MP}^{(0)} - \varepsilon_i + \varepsilon_a\right)\left|\psi_i^a\right\rangle \tag{2.74}$$

$$\hat{F}\left|\psi_{ij}^{ab}\right\rangle = \left(E_{MP}^{(0)} - \varepsilon_i - \varepsilon_j + \varepsilon_a + \varepsilon_b\right)\left|\psi_{ij}^{ab}\right\rangle \tag{2.75}$$

which gives us the zeroth-order energies for the singly and doubly excited wavefunctions,

$$E_i^{a(0)} = E_{MP}^{(0)} - \varepsilon_i + \varepsilon_a \tag{2.76}$$

$$E_{ij}^{ab(0)} = E_{MP}^{(0)} - \varepsilon_i - \varepsilon_j + \varepsilon_a + \varepsilon_b \tag{2.77}$$

By substituting the expression for the first-order MP wavefunction given by Equation (2.73), and the MP perturbation operator given by Equation (2.69) into the general expression for the second-order energy, Equation (2.59), we obtain the following expression for the second-order MP perturbation energy $E_{MP}^{(2)}$

$$\begin{aligned} E_{MP}^{(2)} &= \left\langle \psi_{HF} \middle| \hat{U}_{MP} \middle| \Phi_0^{(1)} \right\rangle \\ &= \sum_{ia} t_a^{i(1)} \left\langle \psi_{HF} \middle| \hat{U}_{MP} \middle| \psi_i^a \right\rangle \\ &\quad + \sum_{\substack{i<j,\\ a<b}} t_{ab}^{ij(1)} \left\langle \psi_{HF} \middle| \hat{U}_{MP} \middle| \psi_{ij}^{ab} \right\rangle \\ &\quad + \sum_{\substack{i<j<k,\\ a<b<c}} t_{abc}^{ijk(1)} \left\langle \psi_{HF} \middle| \hat{U}_{MP} \middle| \psi_{ijk}^{abc} \right\rangle + \dots \end{aligned} \tag{2.78}$$

Now, according to the Brillouin theorem (Section 2.2.1), the singly excited determinants do

not interact directly with the HF reference determinant. Therefore, the first term in the above equation is zero. Moreover, since the perturbation operator is a two-electron operator, it does not mix determinants that differ by more than two electrons. This implies that the triply and higher excited wavefunctions do not couple with the reference wavefunction, leaving us with only the doubly excited terms in the first-order MP2 wavefunction

$$E_{MP}^{(2)} = \sum_{\substack{i<j,\\ a<b}} t_{ab}^{ij(1)} \left\langle \psi_{HF} \middle| \hat{U}_{MP} \middle| \psi_{ij}^{ab} \right\rangle \tag{2.79}$$

The amplitudes for double excitations can be evaluated using Equation (2.64), Equation (2.71), and Equation (2.77) as

$$\begin{aligned} t_{ab}^{ij(1)} &= \frac{\left\langle \psi_{ij}^{ab} \middle| \hat{U}_{MP} \middle| \psi_{HF} \right\rangle}{E_{HF} - E_{ij}^{ab(0)}} \\ &= \frac{\left\langle \psi_{ij}^{ab} \middle| \hat{U}_{MP} \middle| \psi_{HF} \right\rangle}{\varepsilon_i + \varepsilon_j - \varepsilon_a - \varepsilon_b} \end{aligned} \tag{2.80}$$

Using the expression for the perturbation operator in Equation (2.69), and the rules for evaluation of matrix elements in Equation (2.12), we get

$$\begin{aligned} \left\langle \psi_{HF} \middle| \hat{U}_{MP} \middle| \psi_{ij}^{ab} \right\rangle &= \left\langle \psi_{HF} \middle| \sum_i \sum_{j>i} \frac{1}{r_{ij}} \middle| \psi_{ij}^{ab} \right\rangle - \left\langle \psi_{HF} \middle| \sum_i^N \sum_p^N \left[\hat{J}_p(i) - \hat{K}_p(i) \right] \middle| \psi_{ij}^{ab} \right\rangle \\ &= \langle ij||ab \rangle \end{aligned} \tag{2.81}$$

Since $\hat{J}_p(i)$ and $\hat{K}_p(i)$ are one-electron operators, all of their matrix elements between the ground state and the doubly excited determinants vanish. Using Equation (2.80) and Equation (2.81) in Equation (2.79), we finally get the expression for the second-order energy correction,

$$\begin{aligned} E_{MP}^{(2)} &= \sum_{\substack{i<j,\\ a<b}} t_{ab}^{ij(1)} \langle ij||ab \rangle \\ &= \sum_{\substack{i<j,\\ a<b}} \frac{\langle ij||ab \rangle \langle ab||ij \rangle}{\varepsilon_i + \varepsilon_j - \varepsilon_a - \varepsilon_b} \\ &= \frac{1}{4} \sum_{ijab} \frac{|\langle ij||ab \rangle|^2}{\varepsilon_i + \varepsilon_j - \varepsilon_a - \varepsilon_b}. \end{aligned} \tag{2.82}$$

where the factor of $\frac{1}{4}$ in the last line accounts for the integral being symmetric in i and j and a and b. $E^{(2)}_{MP}$ provides the leading contribution to the correlation energy defined in Equation (2.43). MPPT, when including perturbations up to nth-order, is denoted as MPn. The total energy at the MP2 level thus becomes,

$$E_{MP2} = E^{(0)}_{MP} + E^{(1)}_{MP} + E^{(2)}_{MP} \tag{2.83}$$

For closed-shell or non-spin-polarized systems, analogously to the HF energy in Section 2.2, the expression for $E^{(2)}_{MP}$ in Equation (2.82) can be further modified by separating the spin and spatial parts of the wavefunction, and integrating over the spin variables

$$E^{(2)}_{MP} = \sum_{i,j}^{N/2} \sum_{a,b=\frac{N}{2}+1}^{M} \frac{\langle ij|ab\rangle \left(2\langle ab|ij\rangle - \langle ab|ji\rangle\right)}{\varepsilon_i + \varepsilon_j - \varepsilon_a - \varepsilon_b} \tag{2.84}$$

where i, j denote the occupied spatial orbitals, and a, b denote the unoccupied spatial orbitals.

2.6.1 Notes on MP2

The MP2 method provides one of the most cost-effective ways to calculate the correlation energy. It recovers approximately 80% to 90% of the total correlation energy. Unlike HF, MPPT is not a variational method, which means that the total energy of MP2 is not necessarily an upper bound to the exact total energy. Thus, MP2 improves the HF energy, but it may overestimate the correlation energy. It is important to note that the applicability of the MP2 method is limited to molecules with a large HOMO-LUMO gap and solids with a large Fermi band gap. This is due to the denominator in Equation (2.82), which, for too small values, leads to the divergence of the perturbation expansion.

Furthermore, due to its non-variational nature, MPPT shows erratic convergence behaviour. This means that with increasing orders of perturbation, the total energy may not converge monotonically towards the exact energy[85]. In practice, it is frequently observed that the MPn series diverges, leading to limited use of higher-order variants such as MP3 and MP4[86].

In its canonical form, MP2 scales as $O(M^5)$ with respect to system size M. The computational cost primarily arises from two factors: the calculation of electron repulsion integrals (ERIs), and the transformation of integrals from the AO basis to the MO basis. A basis set of size M

requires the calculation of M^4 ERIs, and the transformation from AO to MO basis involves $4 \times M^5$ operations. This means that increasing the basis set by a factor of 10 amplifies the calculation cost by 100, 000 times, restricting the application of the MP2 method to small systems and small basis sets. However, various developments have significantly improved the efficiency of the MP2 method. Direct MP2[87,88], and semidirect MP2[89] leverage molecular symmetry and permutational symmetry of ERIs to avoid storing a large ERI matrix on disk. Techniques such as dual-basis MP2[90], pseudospectral approach[91], and density fitting[73,92] have reduced the cost of evaluating and transforming ERIs. For very large systems, fragment-based approaches like the divide and conquer method partition a large system into smaller, more manageable subsystems[93].

Lastly, the calculation cost of the MP2 energy can be substantially reduced by using orbitals other than the delocalised HF orbitals. This concept is central to two approaches that have achieved near-linear or linear scaling of MP2: Laplace-Transformation Atomic Orbital MP2 (LT-AO-MP2)[94,95] and Local MP2 (LMP2)[96]. However, the denominator in the MP2 energy Equation (2.82), involving the HF canonical orbitals, imposes a restriction on using any other orbital basis, as the Fock matrix may not be diagonal in the other basis. This necessitates reformulating the MP2 energy expression in an orbital-invariant fashion, enabling the evaluation of energy in a basis other than the canonical HF orbitals. LT-AO-MP2 uses the Laplace transform to remove the denominator in the MP2 energy expression and employs atomic orbitals to effectively screen ERIs with small contributions. While Laplace transformation can also be applied in the LMP2 method, LMP2 typically utilises the Hylleraas functional for an orbital-invariant formulation of MP2 and employs localised molecular orbitals (LMOs) to exploit the short-range nature of dynamical correlation. This thesis focuses on the LMP2 approach.

2.7 The MP2 Hylleraas Functional

There exists a series of functionals from which the even-ordered energy corrections for RSPT can be obtained iteratively, starting from an approximate wavefunction. This procedure is based on the *Hylleraas variation principle* which enables the calculation of the energy of order $2n$ by

minimising the Hylleraas functional of order $2n$ with respect to the variational parameters Θ,

$$E^{(2n)} = \min_{\Theta} J_H^{(2n)}(\Theta) \tag{2.85}$$

Using Equation (2.53) and Equation (2.59), we write the first-order equation and second-order energy correction for MPPT as

$$\left(\hat{F} - E_{MP}^{(0)}\right)\left|\Phi_0^{(1)}\right\rangle = \left(E_{MP}^{(1)} - \hat{U}_{MP}\right)|\psi_{HF}\rangle \tag{2.86}$$

$$E_{MP}^{(2)} = \left\langle \psi_{HF}\middle|\hat{U}_{MP}\middle|\Phi_0^{(1)}\right\rangle. \tag{2.87}$$

By multiplying Equation (2.86) by $\left\langle\Phi_0^{(1)}\right|$, we get

$$\begin{aligned}\left\langle\Phi_0^{(1)}\middle|\hat{F} - E_{MP}^{(0)}\middle|\Phi_0^{(1)}\right\rangle &= \left\langle\Phi_0^{(1)}\middle|E_{MP}^{(1)} - \hat{U}_{MP}\middle|\psi_{HF}\right\rangle \\ \left\langle\Phi_0^{(1)}\middle|E_{MP}^{(0)} - \hat{F}\middle|\Phi_0^{(1)}\right\rangle &= \left\langle\Phi_0^{(1)}\middle|\hat{U}_{MP}\middle|\psi_{HF}\right\rangle\end{aligned} \tag{2.88}$$

where we have utilised the orthogonality between the HF wavefunction and the first-order wavefunction (Equation (2.50)). Adding Equation (2.88) to Equation (2.87), and rearranging yields the following expression for the second-order energy correction

$$E_{MP}^{(2)} = \left\langle \psi_{HF}\middle|\hat{U}_{MP}\middle|\Phi_0^{(1)}\right\rangle + \left\langle\Phi_0^{(1)}\middle|\hat{U}_{MP}\middle|\psi_{HF}\right\rangle + \left\langle\Phi_0^{(1)}\middle|\hat{F} - E_{MP}^{(0)}\middle|\Phi_0^{(1)}\right\rangle \tag{2.89}$$

The MP2 Hylleraas functional can then be defined as

$$J_{MP2}[\phi] = 2\Re\mathrm{e}\,\langle\phi|\hat{U}_{MP}|\psi_{HF}\rangle + \left\langle\phi\middle|\hat{F} - E_{MP}^{(0)}\middle|\phi\right\rangle \tag{2.90}$$

Here, ϕ is an arbitrary trial wavefunction. This functional is designed to have a minimum at the exact first-order wavefunction. Hence, the first-order wavefunction can be determined by minimising the above functional. It can be shown that for a general wavefunction, the MP2 Hylleraas functional provides an upper bound to the second-order energy correction

$$\begin{aligned}J_{MP2}[\phi] &> E_{MP}^{(2)} \quad \text{for} \quad \phi \neq \Phi_0^{(1)} \\ &= E_{MP}^{(2)} \quad \text{for} \quad \phi = \Phi_0^{(1)}.\end{aligned} \tag{2.91}$$

2.8 Orbital-Invariant MP2 Theory

In this section we reformulate the closed-shell MP2 theory such that it is invariant to the unitary rotations in the subspaces of the occupied and virtual orbitals. We recall that the first-order MP2 wavefunction is given by a linear combination of all doubly excited determinants,

$$\left|\Phi^{(1)}\right\rangle = \frac{1}{2}\sum_{ij}^{val}\sum_{ab}^{virt} t_{ab}^{ij}\left|\psi_{ij}^{ab}\right\rangle \tag{2.92}$$

where the first sum is over the occupied valence orbitals (since the correlation treatment is typically not applied to the core orbitals), and the second sum is over the unoccupied or virtual orbitals. The configurations $\left|\psi_{ij}^{ab}\right\rangle$ are generated by applying spin-summed excitation operators, $\hat{\tau} = \hat{\tau}_\alpha + \hat{\tau}_\beta$, to the HF reference determinant $|\psi_{HF}\rangle$,

$$\left|\psi_{ij}^{ab}\right\rangle = \hat{\tau}_i^a \hat{\tau}_j^b \left|\psi_{HF}\right\rangle \tag{2.93}$$

Since the excitation operators $\hat{\tau}_i^a$ and $\hat{\tau}_j^b$ commute, the configurations used in the expansion of $\phi^{(1)}$ form a redundant set,

$$\left|\psi_{ij}^{ab}\right\rangle = \left|\psi_{ji}^{ba}\right\rangle \tag{2.94}$$

This redundancy of configurations is accounted for by imposing the following restriction on their corresponding amplitudes,

$$t_{ab}^{ij} = t_{ba}^{ji} \tag{2.95}$$

However, some configurations, namely, $\left|\psi_{ij}^{ab}\right\rangle$ and $\left|\psi_{ij}^{ba}\right\rangle$ are non-orthogonal. Therefore, for convenience, contravariant configurations $\left|\tilde{\psi}_{ij}^{ab}\right\rangle$ are introduced, which along with the original configurations, $\left|\psi_{ij}^{ab}\right\rangle$, form the basis for a biorthogonal representation of the doubly excited space

$$\left|\tilde{\psi}_{ij}^{ab}\right\rangle = \frac{1}{6}\left(2\left|\psi_{ij}^{ab}\right\rangle + \left|\psi_{ij}^{ba}\right\rangle\right) \tag{2.96}$$

such that the following conditions are fulfilled

$$\left\langle\tilde{\psi}_{ij}^{ab}\middle|\Phi^{(1)}\right\rangle = t_{ab}^{ij} \tag{2.97}$$

$$\left\langle\tilde{\psi}_{ij}^{ab}\middle|\psi_{kl}^{cd}\right\rangle = \delta_{ik}\delta_{jl}\delta_{ac}\delta_{bd} + \delta_{il}\delta_{jk}\delta_{ad}\delta_{bc} \tag{2.98}$$

The first-order MP2 wavefunction is now expressed in terms of the contravariant configurations and amplitudes as

$$\left|\Phi^{(1)}\right\rangle = \sum_{ij}^{val}\sum_{ab}^{virt} \tilde{t}_{ab}^{ij}\left|\tilde{\psi}_{ij}^{ab}\right\rangle \tag{2.99}$$

which leads to the following definition of contravariant amplitudes

$$\tilde{t}_{ab}^{ij} = 2t_{ab}^{ij} - t_{ba}^{ij}. \tag{2.100}$$

We now recall that the MP2 Hylleraas functional is given by

$$E_{MP}^{(2)} = 2\left\langle\Phi^{(1)}\middle|\hat{U}_{MP}\middle|\psi_{HF}\right\rangle + \left\langle\Phi^{(1)}\middle|\hat{F} - E_{MP}^{(0)}\middle|\Phi^{(1)}\right\rangle \tag{2.101}$$

Expanding $\left\langle\Phi^{(1)}\right|$ in Equation (2.101) using Equation (2.99), we get

$$E_{MP}^{(2)} = \sum_{ij}^{val}\sum_{ab}^{virt} \tilde{t}_{ab}^{ij*}\left[2\left\langle\tilde{\psi}_{ij}^{ab}\middle|\hat{U}_{MP}\middle|\psi_{HF}\right\rangle + \left\langle\tilde{\psi}_{ij}^{ab}\middle|\hat{F} - E_{MP}^{(0)}\middle|\Phi^{(1)}\right\rangle\right] \tag{2.102}$$

Analogously to Equation (2.81), the matrix element in the first term in Equation (2.102) can be derived to be

$$\left\langle\tilde{\psi}_{ij}^{ab}\middle|\hat{U}_{MP}\middle|\psi_{HF}\right\rangle = \langle ij||ab\rangle \tag{2.103}$$

The matrix element in the second term in Equation (2.102) can be simplified to

$$\left\langle\tilde{\psi}_{ij}^{ab}\middle|\hat{F} - E_{MP}^{(0)}\middle|\Phi^{(1)}\right\rangle = \sum_{c}^{virt}\left(f_{ac}t_{cb}^{ij} + f_{cb}t_{ac}^{ij}\right) - \sum_{k}^{val}\left(f_{ik}t_{ab}^{kj} + f_{kj}t_{ab}^{ik}\right) \tag{2.104}$$

where the Fock matrix elements are defined as

$$f_{pq} = h_{pq} + \sum_{j}\underbrace{\left[\langle p|J_j|q\rangle - \langle p|K_j|q\rangle\right]}_{\langle pj||qj\rangle} \tag{2.105}$$

The MP2 Hylleraas functional thus becomes,

$$E^{(2)}_{MP} = \sum_{ij}^{val}\sum_{ab}^{virt} \tilde{t}^{ij*}_{ab}\left[2\langle ij||ab\rangle + \left(\sum_{c}^{virt}\left(f_{ac}t^{ij}_{cb} + f_{cb}t^{ij}_{ac}\right) - \sum_{k}^{val}\left(f_{ik}t^{kj}_{ab} + f_{kj}t^{ik}_{ab}\right)\right)\right] \tag{2.106}$$

$$= \sum_{ij}^{val}\sum_{ab}^{virt} \tilde{t}^{ij*}_{ab}\left[\langle ij||ab\rangle + \left(\langle ij||ab\rangle + \sum_{c}^{virt}\left(f_{ac}t^{ij}_{cb} + f_{cb}t^{ij}_{ac}\right) - \sum_{k}^{val}\left(f_{ik}t^{kj}_{ab} + f_{kj}t^{ik}_{ab}\right)\right)\right] \tag{2.107}$$

$$= \sum_{ij}^{val}\sum_{ab}^{virt} \tilde{t}^{ij*}_{ab}\left(\langle ij||ab\rangle + R^{ij}_{ab}\right) \tag{2.108}$$

Thus, the Hylleraas functional is now expressed explicitly in terms of the MP2 double excitation amplitudes, and the so-called *residual* equations are defined as

$$R^{ij}_{ab} = \langle ij||ab\rangle + \sum_{c}^{virt}\left(f_{ac}t^{ij}_{cb} + f_{cb}t^{ij}_{ac}\right) - \sum_{k}^{val}\left(f_{ik}t^{kj}_{ab} + f_{kj}t^{ik}_{ab}\right) \tag{2.109}$$

The Hylleraas functional (Equation (2.108)) is then minimised with respect to the MP2 double excitation amplitudes

$$\frac{\partial E^{(2)}_{MP}}{\partial \tilde{t}^{ij}_{ab}} = R^{ij}_{ab} := 0 \tag{2.110}$$

As mentioned earlier, when the Fock matrix is non-diagonal, the amplitudes have to be determined iteratively until the residuals R^{ij}_{ab} of the second-order energy vanish. In the special case where the Fock matrix is diagonal *i.e.* if we were using the canonical HF orbitals so that $f_{pq} = \delta_{pq}\varepsilon_p$, the solution to the residual equations reduces to the first-order amplitudes derived from the canonical MP2 formulation

$$t^{ij}_{ab} = \frac{\langle ij||ab\rangle}{\varepsilon_i + \varepsilon_j - \varepsilon_a - \varepsilon_b} \tag{2.111}$$

In orbital invariant MP2 formulation, minimising the Hylleraas functional provides optimised amplitudes for which the residuals vanish leading to the standard MP2 energy expression

$$E^{(2)}_{MP} = \sum_{ij}^{val}\sum_{ab}^{virt} \tilde{t}^{ij*}_{ab}\langle ij||ab\rangle \tag{2.112}$$

2.9 Fundamentals of Local Correlation Approach

V. Fock showed that the single determinantal many-electron wavefunction is invariant to the basis chosen for its molecular orbitals as long as the orbitals remain orthonormal, and the occupied and unoccupied orbitals do not couple *i.e.* $f_{aj} = 0$[97]. Therefore, the energy of the wavefunction remains unchanged by unitary transformations among its molecular orbitals. The advantage of the canonical HF orbitals is that they diagonalise the Fock matrix, and thus solving the HF equations simply becomes an eigenvalue problem. We also observed in the previous chapter that the closed-shell MP2 amplitudes can be determined straightforwardly in one step when using canonical orbitals. However, despite being the simplest correlation method, conventional MP2 scales as $O(N^5)$. Needless to say, advanced correlation methods scale even more steeply.

To address this scalability issue, various approximations have been developed to reduce the computational cost of post-HF methods while preserving their accuracy. The most successful of these approximations are rooted in exploiting the locality of electron correlation and can be loosely classified into two categories. The first category consists of fragmentation approaches, where the system of interest is partitioned into fragments and total correlation is approximated by the sum of contributions from each fragment[51,98,99]. The second category treats the whole system at once by introducing local approximations. The concept of local correlation methods originated with Pulay's work[71]. Such methods are motivated by the well-known fact that since the dynamical correlation energy decreases as $\frac{1}{r_{ij}^6}$ as the interelectronic distance r_{ij} increases, electron correlation is a short-range phenomenon, especially in insulators. Therefore, the steep scaling of conventional wavefunction methods is not physically justified. Since electron correlation is short-ranged, we can limit the correlation treatment to only those pairs of electrons that are spatially close to each other. However, we cannot achieve this using the canonical orbitals because they remain delocalised over large parts of the molecule, so in the canonical orbital picture, every electron is spatially close to every other electron. However, by taking advantage of the invariance of the wavefunction and the total energy with respect to the molecular orbital basis, we can unitarily transform the canonical occupied molecular orbitals such that the spatial extent of the orbitals is minimised with respect to some metric. This way, we can generate localised molecular orbitals (LMOs) that can then be used to screen pairs based on interelectronic distances or pair correlation energies. All pairs beyond a certain distance or

with a pair correlation energy below a certain threshold can be either neglected or treated at a lower level of theory. This is known as pair approximation, and it leads to significant reductions in computational cost compared to conventional methods. The pair approximation is based on Nesbet's theorem[100], which says that the exact total correlation energy E_{corr} can be expressed as a sum of pair correlation energies e_{ij}

$$E_{corr} = \sum_{ij}^{pairs} e_{ij} \tag{2.113}$$

We recall that the first-order MP2 wavefunction is generated by excitations from pairs of occupied orbitals (Equation (2.92)). When the virtual space is also localised, the integral $\langle ij||ab\rangle$ exhibits exponential decay with increasing distance between the orbitals. Consequently, contributions to the wavefunction from excitations $i \longrightarrow a$ and $j \longrightarrow b$ are significant only when orbitals i and j are spatially close to a and b. Thus, we can confine the excitations from every LMO i to a subset of localised virtual orbitals a that are in close spatial proximity to i. This subset forms a domain of virtual orbitals $a \in [i]$ for orbital i. The combination of domains from two occupied orbitals constitutes a pair domain $[ij] \equiv [i] \cup [j]$, and excitations in the wavefunction ψ_{ij}^{ab} are constrained to the pair domain $[ij]$. This strategy is known as domain approximation. The size of the domains can be expanded by including more virtual orbitals. In the limit of incorporating all possible pairs and complete domains, the canonical correlation energy is recovered. The accuracy of such a method relies on local approximations, specifically the number of included pairs and the sizes of their domains. The domain sizes required to reach a desired accuracy depend crucially on the choice of the localised virtual orbitals. However, asymptotically, the number of pairs and the sizes of the pair domains become independent of the system size and this paves the way for a low-order or linearly scaling method[101–103].

The efficiency and accuracy of local correlation methods are sensitive to local approximations. For example, pairs can be classified as 'strong', 'weak' and 'distant' based on either a distance criterion or pair energy criteria, but the latter shows a faster convergence than the former[104]. Similarly, the convergence of the correlation energy with respect to the domain sizes is also important. In subsequent sections, the commonly employed constructions of LMOs and local virtual spaces are briefly described.

2.10 Localised Occupied Space

The occupied molecular orbitals represent the electron density; thus the locality of the occupied orbitals is closely related to the electronic structure of the system. Therefore, LMOs are regarded as providing a chemically intuitive picture of the electronic structure and bonding in the system. LMOs $\mathbf{\Phi}^{loc}$ can be obtained by applying a unitary transformation $\mathbf{U}^{loc}$ on the canonical molecular orbitals $\mathbf{\Phi}^{can}$.

$$|i\rangle \equiv \left|\phi_i^{loc}\right\rangle = \sum_k^{val} \left|\phi_k^{can}\right\rangle U_{ki}^{loc} \tag{2.114}$$

While the transformation matrix $\mathbf{U}^{loc}$ can be generated by projecting the canonical occupied orbitals onto a predefined set of local functions, such as the atomic orbitals, the most successful approaches for constructing LMOs are iterative schemes where $\mathbf{U}^{loc}$ optimises a localisation functional. The most commonly used functionals are briefly described below.

2.10.1 Foster-Boys (FB)

The FB localisation minimises the spread or the spatial extent of an orbital. It turns out that this is equivalent to minimising the sum of orbital variances[105]

$$\mathcal{L}_{FB} = \sum_k^{\{x,y,z\}} \sum_i^{val} \left(\langle \phi_i | r_k^2 | \phi_i \rangle - \langle \phi_i | r_k | \phi_i \rangle^2 \right) \tag{2.115}$$

FB localisation produces what are known as *banana* LMOs, which are linear combinations of σ and π orbitals. Formally, the iterative FB procedure scales as N^3.

2.10.2 Edmiston-Ruedenberg (ER)

The ER scheme aims to minimise the interorbital Coulomb repulsion or exchange energy between the orbitals. This is equivalent to maximising the intraorbital repulsion, also known as the electronic self-repulsion energy[106]

$$\mathcal{L}_{ER} = \sum_i^{val} \langle \phi_i \phi_i | \phi_i \phi_i \rangle \tag{2.116}$$

ER localisation is favoured over FB for π-bonded systems because it effectively maintains the distinction between σ and π bonds in double bonds. While the conventional implementation of the ER scheme using Jacobi sweeps scales as N^5, adopting a more modern DIIS-like approach[107] can significantly reduce this to cubic scaling or even lower, provided that we start with sufficiently local initial guess orbitals.

2.10.3 Pipek-Mezey (PM)

The PM localisation relies on atomic charges, unlike the FB and ER methods. The original definition of the PM functional uses Mulliken population charges, but other population definitions may also be employed[108]. LMOs are constructed by maximising the sum of squares of partial charges q_{Ai}

$$\mathcal{L}_{PM} = \sum_{A}^{atoms} \sum_{i}^{val} q_{Ai}^2 \tag{2.117}$$

The objective of this functional is to build LMOs such that they reside on as few atoms as possible. Contrary to FB and similarly to ER, the PM localisation preserves the separation between σ and π orbitals in linear and planar systems. The PM scheme formally scales as N^4 with the number of occupied orbitals N, and it scales cubically with the basis set size.

2.10.4 Intrinsic Bond Orbitals (IBOs)

Mulliken population analysis is highly basis set dependent, and it results in poor localisation when diffuse atomic orbitals are used. This is because, contrary to minimal basis AOs, the assignment of AOs to atoms becomes ambiguous in large basis sets with diffuse functions. This issue can be resolved using Knizia's Intrinsic Atomic Orbitals (IAOs) $|\rho\rangle$, which are a set of AOs resembling minimal basis AOs[109]. IAOs are built by defining a set of perturbed core and valence AOs that can exactly describe the occupied space of the previously computed SCF wavefunction. Importantly, IAOs are independent of the basis set, ensuring that the partial charges derived from them are well-suited for an unbiased population analysis. Performing PM localisation using partial charges derived from IAOs generates IBOs. The functional to obtain IBOs can then be expressed as

$$\mathcal{L}_{IBO} = \sum_{A}^{atoms} \sum_{i}^{val} \left(\sum_{\rho \in A} \langle \phi_i | \rho \rangle \langle \rho | \phi_i \rangle \right)^2 \tag{2.118}$$

2.10.5 Cholesky Orbitals

All the methods described so far define the locality of orbitals using a functional, and the iterative optimisation of those functionals results in the generation of LMOs. In this section, we explore a non-iterative localisation scheme where the locality of LMOs is inherited from the one-particle density matrix. We will later adapt this scheme for periodic systems.

Recalling that MOs are expanded in AO basis as

$$\phi_i(\mathbf{r}) = \sum_{\mu} C_{\mu i}\, \mu(\mathbf{r}) \tag{2.119}$$

where the MOs are orthonormal and the overlap between AOs is denoted by $S_{\mu\nu} = \langle \mu | \nu \rangle$. The one-particle density matrix for a closed-shell system is defined as

$$D_{\mu\nu} = 2 \sum_{i}^{N/2} C_{\mu i} C_{\nu i}^{*} \tag{2.120}$$

This density matrix describes the interaction between AOs, with a higher magnitude indicating a stronger interaction. Because MOs are expressed as linear combinations of AOs, the regions of strong interaction between AOs determine the locality of MOs. Consequently, the sparsity of the one-particle density matrix indirectly characterises the locality of MOs.

Moreover, density $\rho(\mathbf{r}, \mathbf{r}')$ is directly related to the HOMO-LUMO gap g in molecules and, equivalently, the band gap in solids[110].

$$\begin{aligned} \rho(\mathbf{r}, \mathbf{r}') &\sim e^{-g|\mathbf{r}-\mathbf{r}'|} \quad (g > 0) \\ \rho(\mathbf{r}, \mathbf{r}') &\sim \frac{1}{|\mathbf{x}-\mathbf{x}'|\,|\mathbf{y}-\mathbf{y}'|\,|\mathbf{z}-\mathbf{z}'|} \quad (g = 0) \end{aligned} \tag{2.121}$$

For insulating systems ($g > 0$), the density decays exponentially with distance $|\mathbf{r} - \mathbf{r}'|$. In other words, in insulators, the density is localised. Therefore, for systems that are appreciably larger than the decay length dictated by the band gap, the one-particle density matrix is expected to be sparse. This establishes a close relationship between the density matrix and the orbital localisation.

Utilising the fact that the density matrix is positive semidefinite with a rank equal to the number

of occupied orbitals, Aquilante *et al.*proposed using the Cholesky decomposition of the density matrix to generate localised orbitals[111].

$$D_{\mu\nu} = 2\sum_{i}^{N/2} L_{\mu i} L_{\nu i}^{*} \tag{2.122}$$

Here, **L** denotes a lower triangular matrix obtained from Cholesky decomposition. The resulting localised orbitals, which we refer to as Cholesky orbitals $\phi_i^{cho}(\mathbf{r})$, are expressed as

$$\phi_i^{cho}(\mathbf{r}) = \sum_{\mu} \mu(\mathbf{r}) L_{\mu i} \tag{2.123}$$

Cholesky decomposition presents a non-iterative method for constructing localised orbitals, which avoids the convergence issues associated with previously discussed iterative localisation techniques. Since Cholesky orbitals do not require an initial guess, the diagonalisation of the Fock matrix to obtain canonical orbitals can be bypassed entirely. Additionally, Cholesky decomposition is a well-established and numerically efficient algorithm that can be easily adapted for linear-scaling applications. Although Cholesky MOs may not be as well localised as the localised MOs obtained through iterative methods, they are significantly better than the highly delocalised canonical orbitals. Therefore, they can still be valuable for achieving linear scaling in local correlation methods. Furthermore, using Cholesky MOs as an initial guess in iterative schemes can help reduce the number of iterations required for convergence[111].

2.11 Local Virtual Space

The efficiency of local correlation methods depends significantly on the convergence of correlation energy relative to the sizes of virtual orbital domains. This is particularly important because the virtual space is often much larger than the occupied space, especially when using high-quality basis sets. Therefore, it is highly desirable to compress the virtual space as much as possible, highlighting the importance of selecting appropriate virtual orbitals. The simplest type of localised virtual orbitals can be obtained like LMOs by applying a localisation criterion. These local virtual orbitals are useful due to their orthonormality. However, research has shown that much smaller domains may be needed to achieve a certain level of accuracy if the orthogonality of the orbitals is forfeited. This can be done by using different types of virtual

orbitals that are not created through a localisation functional but are instead inherently local by design. This section will focus on such intrinsically local virtual spaces, which are spanned by Projected Atomic Orbitals (PAOs) and Pair Natural Orbitals (PNOs).

2.11.1 Projected Atomic Orbitals (PAOs)

Introduced by Pulay in 1983, PAOs are the simplest type of inherently local virtual orbitals[71]. PAOs $|\breve{\mu}\rangle$ are constructed by projecting a suitable set of atomic orbitals $\left|\phi_{\breve{\mu}}^{AO}\right\rangle$ against the localised occupied space $|i\rangle$

$$|\breve{\mu}\rangle = \left[1 - \sum_{i}^{occ} |i\rangle \langle i|\right] \left|\phi_{\breve{\mu}}^{AO}\right\rangle \tag{2.124}$$

where the projection operator $\hat{P}$ is defined as

$$\hat{P} = 1 - \sum_{i}^{occ} |i\rangle \langle i| \tag{2.125}$$

The purpose of $\hat{P}$ is to remove the components of the AO basis that constitute the LMOs. The linear combination of the remaining components of the AO basis forms the PAOs. Therefore, PAOs are orthogonal to LMOs: $\langle \breve{\mu}|i\rangle = 0$ for all $\breve{\mu}, i$. By expanding the LMOs $|i\rangle$ in the AO basis, the projection operator can be expressed as

$$\hat{P} = 1 - \sum_{\mu\nu} \sum_{i}^{occ} |\mu\rangle C_{\mu i} C_{\nu i}^{*} \langle \nu| \tag{2.126}$$

Generally, the atomic orbitals $\left|\phi_{\breve{\mu}}^{AO}\right\rangle$ can be constructed as a linear combination of a group of AOs belonging to a centre A

$$\left|\phi_{\breve{\mu}}^{AO}\right\rangle = \sum_{\kappa \in A} |\nu\rangle C_{\kappa\breve{\mu}}^{AO} \tag{2.127}$$

Here, the coefficient matrix $\mathbf{C^{AO}}$ is block diagonal, and every non-zero block corresponds to one centre. However, typically, the AO basis itself is projected such that each AO acts as a centre. Thus, in the AO basis, $\mathbf{C^{AO}}$ becomes diagonal since $C_{\kappa\breve{\mu}}^{AO} = \delta_{\kappa\breve{\mu}}$. Thus, projecting the

AO basis against the LMOs expanded in the AO basis (Equation (2.126)) gives

$$\begin{aligned} |\check{\mu}\rangle &= \left[1 - \sum_{\mu\nu}\sum_{i}^{occ} |\mu\rangle\, C_{\mu i} C^{*}_{\nu i}\, \langle\nu|\right] \sum_{\kappa} |\nu\rangle\, C^{AO}_{\kappa\check{\mu}} \\ &= \sum_{\kappa}\left[|\nu\rangle - \sum_{\mu\nu}\sum_{i}^{occ} |\mu\rangle\, C_{\mu i} C^{*}_{\nu i} S_{\nu\kappa}\right] \delta_{\kappa\check{\mu}} \end{aligned} \tag{2.128}$$

where $S_{\nu\kappa} = \langle\nu|\kappa\rangle$. In general, the PAOs can be expanded in the AO basis as

$$|\check{\mu}\rangle = \sum_{\mu} |\mu\rangle\, P_{\mu\check{\mu}} \tag{2.129}$$

where the coefficient matrix $\mathbf{P}$ is obtained as

$$\mathbf{P} = \left(\mathbf{1} - \mathbf{C_0 C_0^{\dagger} S}\right) \mathbf{C^{AO}} = \mathbf{C_v C_v^{\dagger} S C^{AO}} = \mathbf{C_v Q} \tag{2.130}$$

where $\mathbf{C_0}$ represents the coefficients of expansion of LMOs, $\mathbf{C_v}$ corresponds to the canonical virtual orbitals and $\mathbf{S}$ is the usual AO overlap matrix. Thus, each PAO can be uniquely expanded in terms of the canonical virtual orbitals as

$$|\check{\mu}\rangle = \sum_{b}^{virt} \left|\phi_b^{can}\right\rangle Q_{b\check{\mu}} \tag{2.131}$$

where the transformation matrix $\mathbf{Q} = \mathbf{C_v^{\dagger} S C^{AO}}$ is rectangular with dimensions $N_{virt} \times N_{AO}$. Thus, we get N_{AO} number of PAOs which are non-orthogonal with overlap

$$S_{\check{\mu}\check{\nu}} = P^{*}_{\mu\check{\mu}} S_{\mu\nu} P_{\nu\check{\nu}} \tag{2.132}$$

The PAO overlap matrix is spin-dependent and is symmetric, positive semi-definite. It has exactly N_{virt} non-zero eigenvalues and N_{occ} zero eigenvalues. PAOs provide a single set of non-orthogonal virtual orbitals for the entire occupied space. Since there are more PAOs than the number of virtual orbitals, PAOs form a redundant set. While PAOs can be uniquely expressed in the canonical virtual basis, due to their redundancy, there is no unique expansion of the

canonical virtual orbitals in terms of PAOs.

$$\left|\phi_c^{can}\right\rangle = \sum_{\breve{\mu}}^{PAOs} |\breve{\mu}\rangle\, C_{\breve{\mu}c} \tag{2.133}$$

$$= \sum_{\breve{\mu}}^{PAOs} \sum_{b}^{virt} \left|\phi_b^{can}\right\rangle Q_{b\breve{\mu}} C_{\breve{\mu}c} \tag{2.134}$$

$$= \sum_{\breve{\mu}}^{PAOs} \sum_{b}^{virt} \left|\phi_b^{can}\right\rangle \delta_{bc} \tag{2.135}$$

where we have used Equation (2.131). Since PAOs form a non-orthogonal set, a biorthogonal dual basis is used to expand the virtual orbitals in terms of the PAOs. The expansion coefficients $C_{\breve{\mu}c}$ are therefore contravariant vectors. These coefficients are determined by solving the linear equations given by Equation (2.135) or simply solving for $Q_{b\breve{\mu}}C_{\breve{\mu}c} = \delta_{bc}$. However, PAOs being linearly dependent, this system of linear equations remains underdetermined, leading to infinitely many solutions for the vectors $C_{\breve{\mu}c}$. Therefore, an approximate solution is obtained by taking the Moore-Penrose pseudoinverse of $Q_{b\breve{\mu}}$. The solution then corresponds to the minimum 2-norm $\left\|C_{\breve{\mu}c}\right\|$. Finally, once the domains of PAOs are constructed for each pair of LMOs, the linear dependencies in individual domains can be removed by discarding vectors with singular values using singular value decomposition.

2.11.2 Pair Natural Orbitals (PNOs)

As mentioned in Section 2.4, natural orbitals diagonalise the spin-free one-particle density matrix defined by Equation (2.36) and provide the most rapid convergence for the expansion of the CI wavefunction[83]. The utility of natural orbitals is particularly evident in two-electron systems due to the ease of their construction. In a one-electron basis of arbitrary dimension M, the CI wavefunction for a two-electron system would typically consist of $\frac{M(M+1)}{2}$ configurations. In contrast, using natural orbitals reduces this to M configurations. This idea underpinned the development of Pair Natural Orbitals (PNOs) by Edmiston and Krauss[112,113]. PNOs are obtained by diagonalising the virtual block of pair density matrices. While PNOs are true natural orbitals only for two-electron subsystems formed by pairs, they still serve as an effective basis for expanding the many-electron wavefunction. This is evidenced by the significantly faster convergence of configurations in the PNO basis compared to those based on canonical virtual orbitals.

As PNOs are specific to each pair of orbitals, obtaining them directly would require determining the pair densities, which, in turn, would require solving the equations of the targeted theory independently for every orbital pair in the system. However, the computational overhead of this direct calculation negates any potential savings over the original calculation in the basis of canonical virtual orbitals. Consequently, in practice, approximate PNOs are often employed, which have been shown to yield nearly equivalent performance [114]. Since MP2 already captures the most significant contributions to the correlation energy, PNOs can be efficiently approximated using the MP2 pair densities.

We start with the MP2 amplitudes given by Equation (2.111) for a given pair of occupied canonical orbitals $|i\rangle$ and $|j\rangle$. Although PNOs can be obtained from any arbitrary set of occupied orbitals, those constructed from LMOs are particularly well localised. When LMOs are used for the occupied basis, the orbital energies ε_i and ε_j get replaced by the Fock operators f_{ii} and f_{jj} respectively in the LMO basis. The off-diagonal terms $g^{ij}_{ab} = \sum_{k\neq i} f_{ik} t^{kj}_{ab}$ are then neglected in the MP2 residual Equation (2.109), in other words, the amplitudes matrix is asssumed to be diagonal. This gives us the *semi-canonical* MP2 amplitudes

$$t^{ij}_{ab} = \frac{\langle ij||ab\rangle}{f_{ii} + f_{jj} - \varepsilon_a - \varepsilon_b} \tag{2.136}$$

The amplitudes t^{ij}_{ab} are denoted in matrix form as $\mathbf{T}^{ij}$. The pair density matrices $\mathbf{D}^{ij}$ can then be defined in terms of the amplitudes $\mathbf{T}^{ij}$ and their contravariant counterparts $\tilde{\mathbf{T}}^{ij}$ as

$$\mathbf{D}^{ij} = \frac{1}{1+\delta_{ij}}\left(\tilde{\mathbf{T}}^{ij\dagger}\mathbf{T}^{ij} + \tilde{\mathbf{T}}^{ij}\mathbf{T}^{ij\dagger}\right) \tag{2.137}$$

The elements of the pair density matrices are expressed as

$$D^{ab}_{ij} = 2\sum_{c}(\tilde{t}^{ac}_{ij} t^{bc}_{ij} + \tilde{t}^{ca}_{ij} t^{ij}_{cb}) \tag{2.138}$$

diagonalising $\mathbf{D}^{ij}$ gives a set of PNOs $\tilde{a}^{ij}$ as eigenvectors for every LMO pair ij

$$\mathbf{D}^{ij}\mathbf{d}^{ij}_{\tilde{a}} = n^{ij}_{\tilde{a}}\mathbf{d}^{ij}_{\tilde{a}} \tag{2.139}$$

where $n^{ij}_{\tilde{a}}$ is the occupation number corresponding to PNO $\tilde{a}^{ij}$. PNOs are expanded in terms of

canonical virtual orbitals a as

$$\left|\tilde{a}^{ij}\right\rangle = \sum_{a} d^{ij}_{a\tilde{a}} \left|a\right\rangle \tag{2.140}$$

Similarly, the canonical virtual orbitals can be expressed in the PNO basis as

$$\left|a\right\rangle = \sum_{\tilde{a}} c^{ij}_{\tilde{a}a} \left|\tilde{a}^{ij}\right\rangle \tag{2.141}$$

PNOs possess some interesting properties. They are orthogonal to the set of occupied orbitals. While the PNOs associated with a specific pair of LMOs form an orthonormal set, those corresponding to different pairs do not, resulting in an overlap between them

$$S^{ij,kl}_{\tilde{a}\tilde{b}} = \left\langle \tilde{a}^{ij} \middle| \tilde{b}^{ij} \right\rangle = (\mathbf{d}^{ij\dagger}\mathbf{d}^{kl})_{\tilde{a}\tilde{b}} \tag{2.142}$$

PNOs are localised in the region of the corresponding pair. The occupation number associated with a PNO serves as a measure of its relevance towards correlation. The higher the occupation number, the greater the PNO's contribution to correlation. This allows us to truncate the PNO domains by defining an occupation number threshold T_{PNO}. While a calculation in the full PNO basis actually costs more than a canonical calculation, discarding PNOs with occupation numbers $n^{ij}_{\tilde{a}} \geq T_{PNO}$ provides computational savings. The larger the truncation threshold, the smaller the PNO domain sizes and the less expensive the calculation becomes. Moreover, the number of PNOs retained after truncation is independent of system size, which dramatically reduces the scaling of a method. However, truncating the PNO basis introduces PNO truncation error, which is the difference between the energy obtained using the truncated PNO basis and the full PNO basis equivalent to the canonical limit. Interestingly, the rate of convergence of the PNO truncation error relative to the truncation threshold T_{PNO} can be exploited to extrapolate to the canonical limit, a topic explored further in this thesis.

2.11.2.1 Orbital-Specific Virtuals (OSVs)

As the name indicates, instead of the pair-specific representation, Orbital-Specific Virtuals (OSVs) provide orbital-specific representation of the virtual space. OSVs are actually identical to PNOs for diagonal pairs ii. Thus, they can be obtained by diagonalising the diagonal pair density matrices $\mathbf{D}^{ii}$, which is equivalent to the diagonalisation of amplitude matrices

$\mathbf{T}^{ii}$. OSVs for a given occupied orbital i form orbital domains $[i]_{OSV}$. The pair domains required in local correlation schemes are then formed as the combination of the orbital domains, $[ij]_{OSV} = [i]_{OSV} \cup [j]_{OSV}$, and then orthonormalised. The average size of OSV pair domains, however, is generally larger than PNO pair domains. The size of PNO pair domains shrinks with increasing distance between i and j, but that of OSV domains does not, consequently requiring much higher computational effort. Thus, in terms of pair domain sizes, the order is PAOs > OSVs > PNOs among the three discussed local virtual orbitals.

Although, not suitable for direct use, OSVs can be employed at an intermediate stage in a PNO-based implementation. This approach may be referred to as the OSV-PNO hybrid approach. In the TURBOMOLE program,[115] the hybrid OSV-PNO approach starts with the construction of PAOs, which are consequently transformed into the OSV basis, which is truncated using a threshold. Then the truncated set of OSVs is used to obtain estimates of pair correlation energies. Based on these estimates, a list of significant pairs is determined. Then, only for the significant pairs, orthonormalised OSV pair domains are formed, which are called pre-PNOs. Consequently, approximate MP2 amplitudes and pair density matrices are constructed in the pre-PNO basis. Those pair density matrices are then diagonalised to obtain PNOs, the domains of which are then truncated using a user-defined occupation number threshold T_{PNO}. The relevant equations are then solved in the truncated PNO basis. Such a hybrid approach avoids two major problems. First, by employing PAOs, the direct transformation from AO to PNO, which can lead to a severe memory bottleneck, can be overcome. Secondly, although pair domains can be built in the PAO basis, their sizes are typically very large, which makes the transformation to the PNO basis costly and potentially memory-greedy. This can be avoided by introducing the OSV basis in the intermediate step, since the OSV pair domains are much smaller than the PAO pair domains. Our work extends this hybrid OSV-PNO approach to periodic systems at the MP2 level.

2.12 Conclusions

MP2 theory provides one of the simplest electron-electron correlation treatments. The conventional formulation of MP2, however, uses the canonical orbitals obtained from HF theory. Since the canonical orbitals remain delocalised throughout the system, they are not suitable

for a local correlation treatment. The concept of orbital rotations through unitary transformations is key to obtaining a local description of the occupied and virtual spaces. We described various procedures that may be used to obtain localised occupied orbitals. Most of these procedures rely on optimising a functional to deduce the unitary transformation which can be used to localise the occupied orbitals. However, a relatively crude but efficient localisation may be obtained through a Cholesky factorisation of the one-particle density matrix, which does not involve optimising any functional. PNOs are inherently local virtual orbitals and provide the most compact description of virtual space. The MP2 theory can be generalised to an orbital-invariant formulation as seen in Section 2.8 to employ localised occupied and virtual orbital descriptions. We extend the orbital-invariant MP2 theory to periodic systems in Chapter 3, where we utilise a Cholesky factorisation scheme to localise the occupied space and employ PNOs for the virtual space of periodic systems.

3 | Periodic PNO-MP2

In this chapter, we present our periodic PNO-MP2 method for a local correlation treatment of periodic systems. We first introduce the fundamental concepts from solid-state physics–namely, the Bloch theorem, reciprocal space, periodic boundary conditions, and the notion of a supercell in Section 3.1. We extend the technique of linear combination of atomic orbitals (LCAO) to crystalline solids and introduce crystalline single-particle states in terms of the Bloch functions in Section 3.2. These single-particle states are analogous to MOs, and we refer to them as Bloch orbitals, while Bloch functions are periodic analogues of AOs in molecules. We then describe the properties of Bloch functions using the idea of supercell AOs. In Sections 3.3 and 3.4, we formulate HF theory and canonical MP2 theory, respectively, for periodic systems. In Section 3.4.1, we derive the two-electron Coulomb repulsion integrals between Bloch orbitals in terms of supercell AOs. We then introduce Wannier functions and their properties, focusing in particular on their inherent gauge freedom, in Section 3.5. We then introduce a new method to localise Wannier functions in Section 3.6. Subsequently, we introduce our periodic local MP2 approach, which utilises localised occupied space defined by Wannier functions in Section 3.7. We extend the hybrid PAO–OSV–PNO scheme under periodic boundary conditions for a local description of the virtual space, as outlined in Section 3.8 through Section 3.10. Although not applied to 2D and 3D systems in this work, Section 3.11 discusses the periodic density fitting approximation and the challenges in achieving convergence of lattice summations arising from long-range electrostatic interactions.

3.1 Bloch Theorem and Periodic Boundary Conditions

Periodic systems, by definition, exhibit an important symmetry property of translational invariance. Using this property effectively, the otherwise intractable computational problem of calculating the electronic structure and properties of crystals can become feasible. This section recapitulates the terminology needed to address a periodic system and some important concepts arising from its translational invariance property.

A periodic lattice can be characterised by vectors $\mathbf{R}$ that allow translation between any two

lattice points

$$\mathbf{R} = n_1\mathbf{a_1} + n_2\mathbf{a_2} + n_3\mathbf{a_3} \tag{3.1}$$

where $\mathbf{a_1}$, $\mathbf{a_2}$, and $\mathbf{a_3}$ are the basis vectors oriented in three non-coplanar directions, and $n_1, n_2, n_3 \in \mathbb{Z}$.

A *primitive* unit cell contains only one lattice point. The entire space can be filled with lattice points by translating this unit cell using the translation vectors $\mathbf{R}$. Unit cells with more than one lattice point can also be defined; they may be referred to as non-primitive unit cells. However, the choice of a unit cell is not unique. All unit cells that contain the same number of lattice points are equivalent to each other.

The potential of a periodic system has the same periodicity as the lattice of the system, which means that the potential energy does not change under any translation using a lattice vector $\mathbf{R}$ as

$$V(\mathbf{r} - \mathbf{R}) = V(\mathbf{r}) \tag{3.2}$$

Therefore, the Hamiltonian $\hat{H}(\mathbf{r})$ of the periodic system is also translationally invariant

$$\hat{H}(\mathbf{r}) = -\frac{1}{2}\nabla^2 + V(\mathbf{r}) \tag{3.3}$$

$$\hat{H}(\mathbf{r} + \mathbf{R}) = \hat{H}(\mathbf{r}) \tag{3.4}$$

The translation operator $\hat{T}_\mathbf{R}$ when applied to a general function $f(\mathbf{r})$ shifts the argument of the function by $\mathbf{R}$

$$\hat{T}_\mathbf{R} f(\mathbf{r}) = f(\mathbf{r} + \mathbf{R}) \tag{3.5}$$

Since the Hamiltonian $\hat{H}(\mathbf{r})$ has the periodicity of the lattice, and every translation operator $\hat{T}_\mathbf{R}$ commutes with every other translation operator $\hat{T}_{\mathbf{R}'}$, it can be shown that $\hat{H}(\mathbf{r})$ commutes with every $\hat{T}_\mathbf{R}$

$$\hat{T}_\mathbf{R}\hat{H}(\mathbf{r})\psi(\mathbf{r}) = \hat{H}(\mathbf{r} + \mathbf{R})\psi(\mathbf{r}) = \hat{H}(\mathbf{r})\psi(\mathbf{r} + \mathbf{R}) = \hat{H}(\mathbf{r})\hat{T}_\mathbf{R}\psi(\mathbf{r}) \tag{3.6}$$

$$\left[\hat{H}(\mathbf{r}), \hat{T}_\mathbf{R}\right] = 0 \tag{3.7}$$

Thus, from a fundamental theorem of quantum mechanics, the eigenstates of the Hamiltonian $\hat{H}(\mathbf{r})$ can simultaneously be the eigenstates of all the translation operators $\hat{T}_\mathbf{R}$ defined by lattice

translation vectors $\mathbf{R}$

$$\hat{H}(\mathbf{r})\psi(\mathbf{r}) = \varepsilon\psi(\mathbf{r}) \implies \hat{T}_{\mathbf{R}}\psi(\mathbf{r}) = \lambda(\mathbf{R})\psi(\mathbf{r}) \tag{3.8}$$

Successive application of translation operators provides a relationship between their eigenvalues

$$\hat{T}_{\mathbf{R}}\hat{T}_{\mathbf{R}'}\psi(\mathbf{r}) = \hat{T}_{\mathbf{R}'}\hat{T}_{\mathbf{R}}\psi(\mathbf{r}) = \hat{T}_{\mathbf{R}+\mathbf{R}'}\psi(\mathbf{r}) = \lambda(\mathbf{R}+\mathbf{R}')\psi(\mathbf{r}) = \lambda(\mathbf{R})\lambda(\mathbf{R}')\psi(\mathbf{r}) \tag{3.9}$$

$$\text{Thus,}\quad \lambda(\mathbf{R}+\mathbf{R}') = \lambda(\mathbf{R})\lambda(\mathbf{R}') \tag{3.10}$$

For $\mathbf{R} = \mathbf{a_i}$ $(i = 1, 2, 3)$, Equation (3.10) can be satisfied if the eigenvalues have the form

$$\lambda(\mathbf{a_i}) = e^{2\pi i x_i} \tag{3.11}$$

where $x_i \in \mathbb{C}$[1]. For a general $\mathbf{R}$ given by Equation (3.1), the eigenvalue becomes

$$\lambda(\mathbf{R}) = \lambda(\mathbf{a_1})^{n_1}\lambda(\mathbf{a_2})^{n_2}\lambda(\mathbf{a_3})^{n_3} = e^{2\pi i n_1 x_1}e^{2\pi i n_2 x_2}e^{2\pi i n_3 x_3} \tag{3.12}$$

Equation (3.12) can be compactly expressed as

$$\lambda(\mathbf{R}) = e^{i\mathbf{k}\cdot\mathbf{R}} \tag{3.13}$$

where $\mathbf{k}$ is known as a wavevector and is defined as

$$\mathbf{k} = x_1\mathbf{b_1} + x_2\mathbf{b_2} + x_3\mathbf{b_3} \tag{3.14}$$

$$\mathbf{b_i} = \frac{2\pi}{\Omega}\mathbf{a_j} \times \mathbf{a_k} \quad ; \quad \Omega = \mathbf{a_1} \cdot (\mathbf{a_2} \times \mathbf{a_3}) \tag{3.15}$$

so that $\mathbf{b_i}$ satisfy the relation $\mathbf{b_i} \cdot \mathbf{a_j} = 2\pi\delta_{ij}$, and Ω is the volume of the unit cell in real space.

Thus, the eigenstates of the Hamiltonian can be chosen such that they are simultaneously also the eigenstates of every translation operator $\hat{T}_{\mathbf{R}}$ with eigenvalues $e^{i\mathbf{k}\cdot\mathbf{R}}$

$$\hat{T}_{\mathbf{R}}\psi_{n\mathbf{k}}(\mathbf{r}) = \psi_{n\mathbf{k}}(\mathbf{r}+\mathbf{R}) = \lambda(\mathbf{R})\psi_{n\mathbf{k}}(\mathbf{r}) = e^{i\mathbf{k}\cdot\mathbf{R}}\psi_{n\mathbf{k}}(\mathbf{r}) \tag{3.16}$$

[1] For a suitable choice of boundary conditions, it can be shown that $x_i \in \mathbb{R}$

$$\text{Thus,}\quad \psi_{n\mathbf{k}}(\mathbf{r}+\mathbf{R}) = e^{i\mathbf{k}\cdot\mathbf{R}}\psi_{n\mathbf{k}}(\mathbf{r}) \tag{3.17}$$

where n is called the *band index* and it labels the independent eigenstates (*bands*) that occur for a given $\mathbf{k}$. Within a given band n, the eigenstates $\psi_{n\mathbf{k}}(\mathbf{r})$ and the eigenvalues $\varepsilon_{n\mathbf{k}}$ vary smoothly with $\mathbf{k}$. Equation (3.17) is a form of the **Bloch theorem**, which provides a relation between the eigenstates of the Hamiltonian at equivalent points in the lattice. The functions $\psi_{n\mathbf{k}}(\mathbf{r})$ that satisfy Equation (3.17) are known as Bloch functions. The Bloch theorem can also be stated as follows: The eigenstates of the one-electron Hamiltonian (Equation (3.3)) described by a periodic potential can be expressed in the form of a travelling plane wave modulated by a periodic function $u_{n\mathbf{k}}(\mathbf{r})$ which has the same periodicity as the lattice

$$\psi_{n\mathbf{k}}(\mathbf{r}) = e^{i\mathbf{k}\cdot\mathbf{r}}u_{n\mathbf{k}}(\mathbf{r}),\quad \text{where}\quad u_{n\mathbf{k}}(\mathbf{r}) = u_{n\mathbf{k}}(\mathbf{r}+\mathbf{R}) \tag{3.18}$$

A periodic function $f(\mathbf{r})$ with the periodicity of the lattice can be expanded as a discrete Fourier series

$$f(\mathbf{r}) = \sum_{\mathbf{G}} f_{\mathbf{G}} e^{i\mathbf{G}\cdot\mathbf{r}} \tag{3.19}$$

where $\mathbf{G}$ are the wavevectors of the plane waves used for expansion and $f_{\mathbf{G}}$ are the expansion coefficients. Since $f(\mathbf{r})$ has the same periodicity as the lattice,

$$f(\mathbf{r}+\mathbf{R}) = \sum_{\mathbf{G}} f_{\mathbf{G}} e^{i\mathbf{G}\cdot\mathbf{R}} e^{i\mathbf{G}\cdot\mathbf{r}} = \sum_{\mathbf{G}} f_{\mathbf{G}} e^{i\mathbf{G}\cdot\mathbf{r}} = f(\mathbf{r}) \tag{3.20}$$

$$\text{Thus,}\quad e^{i\mathbf{G}\cdot\mathbf{R}} = 1 \tag{3.21}$$

For Equation (3.21) to be true for every $\mathbf{G}$ and $\mathbf{R}$,

$$\mathbf{G}\cdot\mathbf{R} = 2\pi n \quad \text{where}\quad n \in \mathbb{Z} \tag{3.22}$$

It can be shown that any vector $\mathbf{G}$ that satisfies Equation (3.22) can be expressed as

$$\mathbf{G} = m_1\mathbf{b_1} + m_2\mathbf{b_2} + m_3\mathbf{b_3} \tag{3.23}$$

where $m_1, m_2, m_3 \in \mathbb{Z}$ and $\mathbf{b_i}$ are defined in Equation (3.15). The set of all wavevectors given by Equation (3.23) defines a *reciprocal lattice* in the *reciprocal space*, also known as the $\mathbf{k}$-*space*,

which in turn is defined by Equation (3.14). Vectors $\mathbf{b_i}$ form the basis for the reciprocal lattice. To differentiate from the reciprocal lattice, the real space lattice given by Equation (3.1) may be referred to as the direct lattice. The reciprocal lattice is simply a Fourier transform of the direct lattice.

The translation of a wavevector $\mathbf{k}$ by a reciprocal lattice vector $\mathbf{G}$ elucidates an interesting property of Bloch functions in the reciprocal space.

$$\psi_{n(\mathbf{k}+\mathbf{G})}(\mathbf{r}+\mathbf{R}) = e^{i(\mathbf{k}+\mathbf{G})\cdot\mathbf{R}}\psi_{n(\mathbf{k}+\mathbf{G})}(\mathbf{r}) = e^{i\mathbf{k}\cdot\mathbf{R}}\psi_{n(\mathbf{k}+\mathbf{G})}(\mathbf{r}) \tag{3.24}$$

where we have used Equation (3.21). Comparing Equation (3.17) with Equation (3.24), we observe that both $\mathbf{k}$ and $\mathbf{k}+\mathbf{G}$ obey the same translational property; therefore, both $\mathbf{k}$ and $\mathbf{k}+\mathbf{G}$ can refer to the same wavevector $\mathbf{k}$. Thus, Bloch functions and the corresponding eigenvalues have the periodicity of the reciprocal lattice

$$\psi_{n(\mathbf{k}+\mathbf{G})}(\mathbf{r}) = \psi_{n\mathbf{k}}(\mathbf{r}) \tag{3.25}$$

$$\varepsilon_{n(\mathbf{k}+\mathbf{G})} = \varepsilon_{n\mathbf{k}} \tag{3.26}$$

Since Bloch functions are unique only up to a reciprocal lattice vector $\mathbf{G}$, the analysis can be restricted to a single primitive unit cell of the reciprocal lattice, known as the *first Brillouin zone (BZ)*.[2] An arbitrary function $\phi_n(\mathbf{r})$ can then be expanded in the basis of Bloch functions by integrating over all wavevectors $\mathbf{k}$ in the *BZ* as

$$\phi_n(\mathbf{r}) = \frac{1}{\mathcal{N}}\int_{BZ} d\mathbf{k}\; C_{n\mathbf{k}}\;\psi_{n\mathbf{k}}(\mathbf{r}) \tag{3.27}$$

where $\mathcal{N}$ is a normalisation constant and $C_{n\mathbf{k}}$ are the expansion coefficients.

Bloch functions extend infinitely throughout the crystal lattice and do not decay to zero at infinity[3]. In practice, normalising a wavefunction with infinite extent is a problem. To overcome

[2] A primitive unit cell in the reciprocal lattice contains only one reciprocal lattice site. Analogously to the direct lattice, many equivalent choices of a unit cell are possible for the reciprocal lattice, of which a particularly useful one is obtained using the Wigner-Seitz construction. Unit cells obtained using the Wigner-Seitz construction are known as *Brillouin zones*. The Brillouin zone that contains the origin of the reciprocal lattice is known as the *first Brillouin zone*.

[3] In the linear combination of atomic orbitals framework (*vide infra*), this requires taking an infinite sum over the direct lattice vectors.

this issue, we introduce the concept of a *supercell*. A supercell is a finite crystal consisting of $N_{uc} = N_1 \times N_2 \times N_3$[4] cells, and by taking the limit of an infinite supercell *i.e.* $N_{uc} \to \infty$, we can approach the thermodynamic limit of a solid. The periodicity of the solid can be retained by imposing the periodic boundary conditions, known as the **Born-von Kármán boundary conditions**, which can be stated as follows for any $m \in \mathbb{Z}$

$$\psi_{n\mathbf{k}}(\mathbf{r} + mN_j\mathbf{a}_j) = \psi_{n\mathbf{k}}(\mathbf{r}) \quad (j = 1, 2, 3) \tag{3.28}$$

But according to the Bloch theorem (Equation (3.17))

$$\psi_{n\mathbf{k}}(\mathbf{r} + mN_j\mathbf{a}_j) = e^{imN_j\mathbf{k}\cdot\mathbf{a}_j}\,\psi_{n\mathbf{k}}(\mathbf{r}) = e^{imN_j\mathbf{k}_j\mathbf{a}_j}\,\psi_{n\mathbf{k}}(\mathbf{r}) \tag{3.29}$$

By comparing Equation (3.28) and Equation (3.29), we realize that

$$e^{imN_j\mathbf{k}_j\mathbf{a}_j} = 1 \tag{3.30}$$

Equation (3.30) can be satisfied by defining the wavevector components $\mathbf{k}_j$ as follows

$$\mathbf{k}_j = \frac{n_j}{N_j}\mathbf{b}_j \quad \text{where} \quad n_j \in \mathbb{Z} \tag{3.31}$$

Using the above definition, we get N_{uc} wavevectors in every reciprocal lattice unit cell having the form

$$\mathbf{k} = \frac{n_1}{N_1}\mathbf{b}_1 + \frac{n_2}{N_2}\mathbf{b}_2 + \frac{n_3}{N_3}\mathbf{b}_3 \tag{3.32}$$

To restrict the analysis to the *BZ*, we can choose n_j such that $\frac{-N_j}{2} \leq n_j \leq \frac{N_j}{2}$. Thus, as a consequence of the Born-von Kármán (BvK) boundary conditions, the analysis of the wavevector space in *BZ* becomes discretised and, as a result, the integration in Equation (3.27) becomes a sum over the N_{uc} **k**-points. In the thermodynamic limit, $N_{uc} \to \infty$, the number of **k**-points tends to infinity so that **k** becomes a continuous variable. In this way, we get the same number of **k**-points in the *BZ*, $N_{\mathbf{k}}$, as the number of unit cells in the supercell, N_{uc}, on which the BvK boundary conditions are applied ($N_{\mathbf{k}} = N_{uc}$).

The accuracy of calculations in practice relies on the number of **k**-points sampled within the

[4]Here, N_1, N_2 and N_3 refer to the number of cells in x, y and z directions, respectively.

BZ. The number of **k**-points required to achieve a desired accuracy mainly depends on the size of the simulation cell and the band gap. When the simulation cell is large, the reciprocal cell becomes small, thus reducing the integration region for **k** in Equation (3.27) to a small volume. Consequently, only a small number of sampling **k**-points is necessary. For a sufficiently large simulation cell, a single **k**-point may be enough. The integral in Equation (3.27) accounts for the system's periodicity by incorporating all possible wavevectors **k** corresponding to various real space variations (repetitions). These variations include those representing twice the lattice's periodicity as well as infinitely slow variation corresponding to the non-periodic case. In the case of a non-periodic system, where the periodicity itself is an approximation, there is no need to evaluate the integral exactly, and a single **k**-point may be sufficient. The **k**-point that corresponds to an infinitely slow variation in real space is the central point of the *BZ*, known as the Γ-point. Therefore, for large simulation cells and non-periodic systems, a Γ-point calculation is usually adequate. Metallic or semiconducting systems with small band gaps typically require a higher number of **k**-points to accurately describe the Fermi surface. Generally, addressing the convergence of an observable with **k**-point sampling is a standard practice.

The $N_{\mathbf{k}}$ **k**-points in the *BZ* can be sampled in various ways.[5] In this work, we employ the Monkhorst-Pack (MP) **k**-point sampling.[116] The MP scheme generates a set of special **k**-points forming a regular grid in the *BZ*. Using the MP scheme, the integers n_j in Equation (3.32) for q_j number of **k**-points in the j^{th} direction are obtained as

$$n_j = \frac{2r - q_j - 1}{2q_j} \quad \text{where} \quad r = 1, 2, .., q_j \tag{3.33}$$

In practice, the actual number of **k**-points required for a calculation also depend on the system's symmetry. When there is additional symmetry to exploit within the *BZ*, the calculations can be performed for the *irreducible Brillouin zone (IBZ)*, which is a region within the *BZ* that completely characterises the periodic system. Thus, additional symmetries reduce the number of **k**-points necessary for a calculation. Most reciprocal space calculations at least have time-reversal symmetry ($+\mathbf{k} = -\mathbf{k}$). For example, for a $(3 \times 3 \times 3)$ **k**-point grid, one only needs 14 of all 27 **k**-points for a calculation when time reversal symmetry is exploited.

[5] For example, in $1D$, a set of 4 **k**-points can be evenly distributed, as either $(-0.25, 0, 0.25, 0.5)$ or $(-0.375, -0.125, 0.125, 0.375)$.

3.2 Linear Combination of Atomic Orbitals in Crystals

Under BvK boundary conditions applied to a supercell containing $N_{\mathbf{k}}$ unit cells each of volume V, the real space is finite with volume $\mathcal{V} = N_{\mathbf{k}}V$. A non-periodic function $\beta(\mathbf{r}) \in \mathbb{R}^3$ may extend beyond the boundaries of the supercell. However, we can define a function $\tilde{\beta}(\mathbf{r})$ which has the periodicity of the supercell as

$$\tilde{\beta}(\mathbf{r}) = \sum_{L}^{\infty} \beta(\mathbf{r} - \mathbf{R}_L) \tag{3.34}$$

Thus, $\tilde{\beta}(\mathbf{r})$ is periodic, and it is defined in the volume $\mathcal{V}$ of the supercell. The AOs $\mu_l(\mathbf{r})$ corresponding to each atom in an infinite crystal are non-periodic functions. A periodic representation of AOs, known as supercell AOs, can be derived using Equation (3.34).

$$\tilde{\mu}_l(\mathbf{r}) = \sum_{L}^{\infty} \mu_l(\mathbf{r} - \mathbf{R}_L) \tag{3.35}$$

A supercell AO $\tilde{\mu}_l(\mathbf{r})$ is an AO centred in the unit cell l combined with all its periodic images $\mu_l(\mathbf{r} - \mathbf{R}_L)$ under the periodic boundary conditions. Thus, the supercell AOs exhibit the periodicity of the supercell.

In reciprocal space, Bloch functions $\mu_{\mathbf{k}}(\mathbf{r})$ form the basis equivalent to AOs in molecules. Analogous to the deduction of MOs in molecules using the theory of linear combination of atomic orbitals (LCAO), a crystalline orbital $i_{\mathbf{k}}(\mathbf{r})$ (single-particle state in a crystal) can be expanded as a linear combination of Bloch functions

$$i_{\mathbf{k}}(\mathbf{r}) = \sum_{\mu} C_{\mu i}^{\mathbf{k}}\, \mu_{\mathbf{k}}(\mathbf{r}) \tag{3.36}$$

where $\mathbf{k}$ is a general wavevector in the first BZ and $C_{\mu i}^{\mathbf{k}}$ are the expansion coefficients. The LCAO wavefunction is spanned by the set of AOs located on each atom within an infinite material. A Bloch function, denoted as $\mu_{\mathbf{k}}(\mathbf{r})$, is constructed by combining AOs $\mu_l(\mathbf{r})$ from all the unit cells in the infinite crystal, where each cell is indexed by l

$$\mu_{\mathbf{k}}(\mathbf{r}) = \frac{1}{\sqrt{N_{\mathbf{k}}}} \sum_{l}^{\infty} e^{-i\mathbf{k}\cdot\mathbf{R}_l} \mu_l(\mathbf{r}) \tag{3.37}$$

where $\mu_l(\mathbf{r}) \equiv \mu(\mathbf{r} - \mathbf{R}_l)$ is an AO located in the unit cell given by lattice vector $\mathbf{R}_l$. Under periodic boundary conditions, the infinite sum over lattice vectors in Equation (3.37) reduces to a finite sum over the $N_\mathbf{k}$ distinct lattice vectors that lie in the volume $\mathcal{V}$ of the supercell

$$\mu_\mathbf{k}(\mathbf{r}) = \frac{1}{\sqrt{N_\mathbf{k}}} \sum_l^{N_\mathbf{k}} e^{-i\mathbf{k}\cdot\mathbf{R}_l} \tilde{\mu}_l(\mathbf{r}) \tag{3.38}$$

These Bloch functions form an orthonormal basis with respect to the wavevector $\mathbf{k}$, and hence the overlap between the Bloch functions is block diagonal

$$\langle \mu_\mathbf{k} | \nu_{\mathbf{k}'} \rangle = \delta_{\mathbf{k}\mathbf{k}'} S^\mathbf{k}_{\mu\nu} \tag{3.39}$$

$$\begin{gathered} S^\mathbf{k}_{\mu\nu} = \sum_l^{N_\mathbf{k}} e^{-i\mathbf{k}\cdot\mathbf{R}_l} S^l_{\mu\nu} \\ \text{where,} \quad S^l_{\mu\nu} = \langle \tilde{\mu}(\mathbf{r} - \mathbf{R}_l) | \tilde{\nu}(\mathbf{r}) \rangle_\mathcal{V} \end{gathered} \tag{3.40}$$

The integral $S^l_{\mu\nu}$ is defined over the volume $\mathcal{V}$ of the supercell, and it is evaluated by unwrapping it onto $\mathbb{R}^3$ as

$$S^l_{\mu\nu} = \sum_{LM}^{\infty} \int_\mathcal{V} \mu(\mathbf{r} - \mathbf{R}_l - \mathbf{R}_L) \nu(\mathbf{r} - \mathbf{R}_M) d\mathbf{r} \tag{3.41}$$

By changing variables such that $\mathbf{r}' = \mathbf{r} - \mathbf{R}_M$ and $\int d\mathbf{r}' = \sum_M \int_\mathcal{V} d\mathbf{r}$, we get

$$S^l_{\mu\nu} = \sum_L^{\infty} \int \mu(\mathbf{r}' - \mathbf{R}_l - \mathbf{R}_L + \mathbf{R}_M) \nu(\mathbf{r}') d\mathbf{r}' \tag{3.42}$$

The integral is now defined over $\mathbb{R}^3$. The infinite summation over $\mathbf{R}_L$ can be translated to an arbitrary centre $\mathbf{R}_M$ and the dummy variable $\mathbf{r}'$ may be replaced by $\mathbf{r}$ for simplicity of notation

$$S^l_{\mu\nu} = \sum_L^{\infty} \int \mu(\mathbf{r} - \mathbf{R}_l - \mathbf{R}_L) \nu(\mathbf{r}) d\mathbf{r} \tag{3.43}$$

In practice, the non-periodic functions $\mu(\mathbf{r})$ are finite in extent, and their contributions decay more rapidly than the decay rate of $\frac{1}{r^2}$ of Gaussian AOs. Hence, the summation over L can be truncated to discard insignificant contributions from distant functions.

3.3 Periodic Hartree-Fock Theory

While the Bloch functions can be expanded using various types of basis functions such as plane waves, GTOs, and others, we restrict the discussion to GTOs, which are employed in this work. Detailed discussions on the properties and numerical aspects of GTOs can be found in the literature[117–119]. Under BvK periodic boundary conditions applied to a supercell containing $N_{\mathbf{k}}$ unit cells, Bloch functions can be expanded in terms of GTOs as

$$\mu_{\mathbf{k}}(\mathbf{r}) = \frac{1}{\sqrt{N_{\mathbf{k}}}} \sum_{l}^{N_{\mathbf{k}}} \sum_{L}^{\infty} e^{i\mathbf{k}\cdot\mathbf{R}_{l+L}} \mu_{l+L}(\mathbf{r}) \tag{3.44}$$

Here, l labels a unit cell in the supercell, and L labels a supercell under periodic boundary conditions. Henceforth, we refer to the **crystalline single-particle states** $i_{\mathbf{k}}(\mathbf{r})$ defined in Equation (3.36) as **Bloch orbitals**. Using Equation (3.44), the full expansion of a Bloch orbital then reads

$$i_{\mathbf{k}}(\mathbf{r}) = \frac{1}{\sqrt{N_{\mathbf{k}}}} \sum_{\mu} C^{\mathbf{k}}_{\mu i} \sum_{l}^{N_{\mathbf{k}}} \sum_{L}^{\infty} e^{i\mathbf{k}\cdot\mathbf{R}_{l+L}} \mu_{l+L}(\mathbf{r}) \tag{3.45}$$

The HF equations given by Equation (2.25) can then be solved to obtain the optimal Bloch orbitals

$$\hat{f} \sum_{\nu} C^{\mathbf{k}}_{\nu i} \nu_{\mathbf{k}}(\mathbf{r}) = \varepsilon^{\mathbf{k}}_{i} \sum_{\nu} C^{\mathbf{k}}_{\nu i} \nu_{\mathbf{k}}(\mathbf{r}) \tag{3.46}$$

Multiplying by $\mu_{\mathbf{k}}(\mathbf{r})$ from left and integrating over the volume $\mathcal{V}$ of BvK supercell gives

$$\sum_{\nu} C^{\mathbf{k}}_{\nu i} \int_{\mathcal{V}} d^3\mathbf{r}\, \mu^{*}_{\mathbf{k}}(\mathbf{r})\, \hat{f}\, \nu_{\mathbf{k}}(\mathbf{r}) = \varepsilon^{\mathbf{k}}_{i} \sum_{\nu} C^{\mathbf{k}}_{\nu i} \int_{\mathcal{V}} d^3\mathbf{r}\, \mu^{*}_{\mathbf{k}}(\mathbf{r})\, \nu_{\mathbf{k}}(\mathbf{r}) \tag{3.47}$$

which can be compactly written in matrix form as

$$\mathbf{F}^{\mathbf{k}}\mathbf{C}^{\mathbf{k}} = \varepsilon^{\mathbf{k}}\mathbf{S}^{\mathbf{k}}\mathbf{C}^{\mathbf{k}} \tag{3.48}$$

When represented in the Bloch orbital basis, the overlap and the Fock matrices take a block diagonal form where each block corresponds to a wavevector $\mathbf{k}$ and has the dimensions of the one-electron basis, here the GTOs. The Bloch orbitals are normalised,

$$C^{\mathbf{k}*}_{\mu i} S^{\mathbf{k}}_{\mu\nu} C^{\mathbf{k}}_{\nu i} = \delta_{ij} \tag{3.49}$$

Thus, the HF equations for periodic systems can be solved independently for each wavevector $\mathbf{k}$. The Fock matrix elements can then be expressed in the basis of Bloch functions $\{\mu_{\mathbf{k}}\}$ as

$$F^{\mathbf{k}}_{\mu\nu} = \langle \mu_{\mathbf{k}} | \hat{f} | \nu_{\mathbf{k}'} \rangle_{\mathcal{V}} = T^{\mathbf{k}}_{\mu\nu} + Z^{\mathbf{k}}_{\mu\nu} + J^{\mathbf{k}}_{\mu\nu} + K^{\mathbf{k}}_{\mu\nu} \tag{3.50}$$

The calculation of the kinetic energy term $T^{\mathbf{k}}_{\mu\nu}$ is carried out in the same way as in the molecular case, the two Coulomb terms, $Z^{\mathbf{k}}_{\mu\nu}$ and $J^{\mathbf{k}}_{\mu\nu}$ can be evaluated using a combined density fitting and a fast multipole scheme[120,121], and the evaluation of the exchange term $K^{\mathbf{k}}_{\mu\nu}$ is described in Ref. 122.

3.4 Periodic Canonical MP2 Theory

We now extend the MP2 equations to periodic systems in the basis of Bloch orbitals. Given a HF wavefunction for n electrons per unit cell, the total MP2 energy can be obtained by minimising the Hylleraas functional (Equation (2.101)) defined over the BvK supercell of volume $\mathcal{V}$ as

$$E_{MP2} = 2 \left\langle \Phi^{(1)} \middle| \hat{U}_{MP} \middle| \psi_{HF} \right\rangle_{\mathcal{V}} + \left\langle \Phi^{(1)} \middle| \hat{F} - E^{(0)}_{MP} \middle| \Phi^{(1)} \right\rangle_{\mathcal{V}} \tag{3.51}$$

where $|\psi_{HF}\rangle$ and $\hat{F}$ are the HF wavefunction and Hamiltonian, respectively. $\hat{U}_{MP}$ is the perturbation operator, $\left|\Phi^{(1)}\right\rangle$ is the first-order wavefunction, and $E^{(0)}_{MP}$ is the zeroth-order energy. Due to Brillouin's theorem and the rules for evaluating matrix elements, $\left\langle \Phi^{(1)} \middle| \hat{U}_{MP} \middle| \psi_{HF} \right\rangle_{\mathcal{V}}$ is non-zero only if $|\psi_{HF}\rangle$ and $\left|\Phi^{(1)}\right\rangle$ differ by exactly two orbitals

$$\left\langle \Phi^{(1)} \middle| \hat{U}_{MP} \middle| \psi_{HF} \right\rangle_{\mathcal{V}} = \sum_{i_{\mathbf{k}_1} j_{\mathbf{k}_2}} \sum_{a_{\mathbf{k}_3} b_{\mathbf{k}_4}} \langle i_{\mathbf{k}_1} j_{\mathbf{k}_2} \| a_{\mathbf{k}_3} b_{\mathbf{k}_4} \rangle_{\mathcal{V}} \tag{3.52}$$

$$= \sum_{i_{\mathbf{k}_1} j_{\mathbf{k}_2}} \sum_{a_{\mathbf{k}_3} b_{\mathbf{k}_4}} \left(\langle i_{\mathbf{k}_1} j_{\mathbf{k}_2} | r_{12}^{-1} | a_{\mathbf{k}_3} b_{\mathbf{k}_4} \rangle_{\mathcal{V}} - \langle i_{\mathbf{k}_1} j_{\mathbf{k}_2} | r_{12}^{-1} | b_{\mathbf{k}_4} a_{\mathbf{k}_3} \rangle_{\mathcal{V}} \right). \tag{3.53}$$

The corresponding second-order amplitudes $t^{i_{\mathbf{k}_1} j_{\mathbf{k}_2}}_{a_{\mathbf{k}_3} b_{\mathbf{k}_4}}$ are then obtained as

$$t^{i_{\mathbf{k}_1} j_{\mathbf{k}_2}}_{a_{\mathbf{k}_3} b_{\mathbf{k}_4}} = \frac{\langle i_{\mathbf{k}_1} j_{\mathbf{k}_2} \| a_{\mathbf{k}_3} b_{\mathbf{k}_4} \rangle_{\mathcal{V}}}{\varepsilon^{\mathbf{k}_1}_i + \varepsilon^{\mathbf{k}_2}_j - \varepsilon^{\mathbf{k}_3}_a - \varepsilon^{\mathbf{k}_4}_b} \tag{3.54}$$

The total MP2 correlation energy is expressed as

$$E_{MP2} = \frac{1}{4} \sum_{i_{\mathbf{k}_1} j_{\mathbf{k}_2}} \sum_{a_{\mathbf{k}_3} b_{\mathbf{k}_4}} t_{a_{\mathbf{k}_3} b_{\mathbf{k}_4}}^{i_{\mathbf{k}_1} j_{\mathbf{k}_2}} \langle i_{\mathbf{k}_1} j_{\mathbf{k}_2} \| a_{\mathbf{k}_3} b_{\mathbf{k}_4} \rangle_{\mathcal{V}} \tag{3.55}$$

The MP2 correlation energy per unit cell is then given by

$$E_{MP2}^{cell} = -\frac{1}{4N_{\mathbf{k}}} \sum_{i_{\mathbf{k}_1} j_{\mathbf{k}_2}} \sum_{a_{\mathbf{k}_3} b_{\mathbf{k}_4}} \frac{|\langle i_{\mathbf{k}_1} j_{\mathbf{k}_2} \| a_{\mathbf{k}_3} b_{\mathbf{k}_4} \rangle_{\mathcal{V}}|^2}{\varepsilon_a^{\mathbf{k}_3} + \varepsilon_b^{\mathbf{k}_4} - \varepsilon_i^{\mathbf{k}_1} - \varepsilon_j^{\mathbf{k}_2}} \tag{3.56}$$

Thus, the integrals are evaluated for every combination of **k**-points. Sampling just one **k**-point gives us the Γ-point approximation, which is equivalent to applying the BvK boundary conditions to a single unit cell, so that $N_{\mathbf{k}} = 1$, and this simplifies the expression for correlation energy per unit cell to

$$E_{MP2}^{cell} = -\frac{1}{4} \sum_{ijab} \frac{|\langle ij \| ab \rangle_{\mathcal{V}}|^2}{\varepsilon_a + \varepsilon_b - \varepsilon_i - \varepsilon_j} \tag{3.57}$$

3.4.1 Coulomb Integrals Between Bloch Orbitals

The electron repulsion integrals (ERIs) between the Bloch orbitals under BvK boundary conditions are evaluated as

$$\langle i_{\mathbf{k}_1} j_{\mathbf{k}_2} | r_{12}^{-1} | a_{\mathbf{k}_3} b_{\mathbf{k}_4} \rangle_{\mathcal{V}} = \frac{1}{N_{\mathbf{k}}^2} \sum_{lmno}^{N_{\mathbf{k}}} e^{i(\mathbf{k}_1 \cdot \mathbf{R}_l + \mathbf{k}_2 \cdot \mathbf{R}_m - \mathbf{k}_3 \cdot \mathbf{R}_n - \mathbf{k}_4 \cdot \mathbf{R}_o)} \left\langle \tilde{i}_l^{\mathbf{k}_1} \tilde{j}_m^{\mathbf{k}_2} \middle| r_{12}^{-1} \middle| \tilde{a}_n^{\mathbf{k}_3} \tilde{b}_o^{\mathbf{k}_4} \right\rangle_{\mathcal{V}} \tag{3.58}$$

where $\tilde{i}_l^{\mathbf{k}_1}(\mathbf{r})$ is given by a linear combination of supercell AOs $\tilde{\mu}_l(\mathbf{r})$ as

$$\tilde{i}_l^{\mathbf{k}_1}(\mathbf{r}) \equiv \sum_{\mu} C_{\mu i}^{\mathbf{k}} \, \tilde{\mu}_l(\mathbf{r}) \tag{3.59}$$

We now shift the origin of the integration in Equation (3.58) to cell o such that we get new variables $\mathbf{r}_1' \equiv \mathbf{x}_1 - \mathbf{R}_o$ and $\mathbf{r}_2' \equiv \mathbf{x}_2 - \mathbf{R}_o$. Then, the new coordinate transformed lattice vectors are $\mathbf{R}_{l'} \equiv \mathbf{R}_l - \mathbf{R}_o$, $\mathbf{R}_{m'} \equiv \mathbf{R}_m - \mathbf{R}_o$, and $\mathbf{R}_{n'} \equiv \mathbf{R}_n - \mathbf{R}_o$. Expressing the old variables in terms of the new variables, we get the Coulomb integral

$$\langle i_{\mathbf{k}_1} j_{\mathbf{k}_2} | r_{12}^{-1} | a_{\mathbf{k}_3} b_{\mathbf{k}_4} \rangle_{\mathcal{V}} = \frac{1}{N_{\mathbf{k}}^2} \sum_{l'm'n'o}^{N_{\mathbf{k}}} e^{i(\mathbf{k}_1 \cdot \mathbf{R}_{l'} + \mathbf{k}_2 \cdot \mathbf{R}_{m'} - \mathbf{k}_3 \cdot \mathbf{R}_{n'})} e^{i((\mathbf{k}_1 + \mathbf{k}_2 - \mathbf{k}_3 - \mathbf{k}_4) \cdot \mathbf{R}_o)} \left\langle \tilde{i}_{l'}^{\mathbf{k}_1} \tilde{j}_{m'}^{\mathbf{k}_2} \middle| r_{12}^{-1} \middle| \tilde{a}_{n'}^{\mathbf{k}_3} \tilde{b}^{\mathbf{k}_4} \right\rangle_{\mathcal{V}} \tag{3.60}$$

where we have separated the phase factor corresponding to the origin cell o. But the overall phase with respect to the origin must be equal to one so that,

$$e^{i((\mathbf{k}_1+\mathbf{k}_2-\mathbf{k}_3-\mathbf{k}_4)\cdot\mathbf{R}_o)} = 1 \implies \sum_{o}^{N_\mathbf{k}} e^{i((\mathbf{k}_1+\mathbf{k}_2-\mathbf{k}_3-\mathbf{k}_4)\cdot\mathbf{R}_o)} = N_\mathbf{k} \tag{3.61}$$

This imposes the constraint $\mathbf{k}_1 - \mathbf{k}_3 = \mathbf{k}_4 - \mathbf{k}_2 + \mathbf{G}$ or equivalently, $\mathbf{k}_1 + \mathbf{k}_2 - \mathbf{k}_3 - \mathbf{k}_4 = \mathbf{G}$, which stems from conservation of crystal momentum. Thus, simultaneous excitations from two orbitals are only allowed upto the difference of a reciprocal lattice vector. Therefore,

$$\langle i_{\mathbf{k}_1} j_{\mathbf{k}_2} | r_{12}^{-1} | a_{\mathbf{k}_3} b_{\mathbf{k}_4} \rangle_\mathcal{V} = \delta_{\mathbf{k}_1-\mathbf{k}_3,\mathbf{k}_4-\mathbf{k}_2+\mathbf{G}} \frac{1}{N_\mathbf{k}} \sum_{l'm'n'}^{N_\mathbf{k}} e^{i(\mathbf{k}_1\cdot\mathbf{R}_{l'}+\mathbf{k}_2\cdot\mathbf{R}_{m'}-\mathbf{k}_3\cdot\mathbf{R}_{n'})} \left\langle \tilde{i}_{l'}^{\mathbf{k}_1} \tilde{j}_{m'}^{\mathbf{k}_2} \middle| r_{12}^{-1} \middle| \tilde{a}_{n'}^{\mathbf{k}_3} \tilde{b}^{\mathbf{k}_4} \right\rangle_\mathcal{V} \tag{3.62}$$

For convenience, we drop the primes on the dummy indices for the cells,

$$l', m', n' \leftarrow l, m, n \tag{3.63}$$

and expand the integral $\left\langle \tilde{i}_l^{\mathbf{k}_1} \tilde{j}_m^{\mathbf{k}_2} \middle| r_{12}^{-1} \middle| \tilde{a}_n^{\mathbf{k}_3} \tilde{b}^{\mathbf{k}_4} \right\rangle_\mathcal{V}$ in terms of the periodic images of the supercell. The expansion applies not only to $\tilde{i}_l^{\mathbf{k}_1}(\mathbf{r})$, but also to the Coulomb repulsion operator r_{12}^{-1}, which also extends beyond the cell boundaries, wrapping around infinite number of times.

$$\left\langle \tilde{i}_l^{\mathbf{k}_1} \tilde{j}_m^{\mathbf{k}_2} \middle| r_{12}^{-1} \middle| \tilde{a}_n^{\mathbf{k}_3} \tilde{b}^{\mathbf{k}_4} \right\rangle_\mathcal{V} = \sum_{LMNOP}^{\infty} \int_\mathcal{V} d\mathbf{r_1} \int_\mathcal{V} d\mathbf{r_2}\, i_l^{\mathbf{k}_1}(\mathbf{r}_1 - \mathbf{R}_L) j_l^{\mathbf{k}_2}(\mathbf{r}_2 - \mathbf{R}_M) \frac{1}{|\mathbf{r}_1 - \mathbf{r}_2 - \mathbf{R}_P|} a_l^{\mathbf{k}_3}(\mathbf{r}_1 - \mathbf{R}_N) b^{\mathbf{k}_4}(\mathbf{r}_2 - \mathbf{R}_O) \tag{3.64}$$

We shift the origin of the sums to the supercell indexed by O, and apply a change of variables $\mathbf{r}'_1 \equiv \mathbf{x}_1 - \mathbf{R}_P - \mathbf{R}_O$ and $\mathbf{r}'_2 \equiv \mathbf{x}_2 - \mathbf{R}_O$. Then, the new coordinate transformed supercell lattice vectors are $\mathbf{R}_{L'} \equiv \mathbf{R}_L - \mathbf{R}_O - \mathbf{R}_P$, $\mathbf{R}_{M'} \equiv \mathbf{R}_M - \mathbf{R}_O - \mathbf{R}_P$, and $\mathbf{R}_{N'} \equiv \mathbf{R}_N - \mathbf{R}_O - \mathbf{R}_P$. The integral then becomes

$$\left\langle \tilde{i}_l^{\mathbf{k}_1} \tilde{j}_m^{\mathbf{k}_2} \middle| r_{12}^{-1} \middle| \tilde{a}_n^{\mathbf{k}_3} \tilde{b}^{\mathbf{k}_4} \right\rangle_\mathcal{V} = \sum_{L'M'N'OP'}^{\infty} \int_\mathcal{V} d\mathbf{r'}_1 \int_\mathcal{V} d\mathbf{r'}_2\, i_l^{\mathbf{k}_1}(\mathbf{r'}_1 - \mathbf{R}_{L'}) j_l^{\mathbf{k}_2}(\mathbf{r'}_2 - \mathbf{R}_{M'}) \frac{1}{|\mathbf{r'}_1 - \mathbf{r'}_2|} a_l^{\mathbf{k}_3}(\mathbf{r'}_1 - \mathbf{R}_{N'}) b^{\mathbf{k}_4}(\mathbf{r'}_2) \tag{3.65}$$

We can then unwrap the periodic integral onto $\mathbb{R}^3$ using $\sum_P \int_\mathcal{V} d\mathbf{r'}_1 = \int d\mathbf{r'}_1$, and $\sum_O \int_\mathcal{V} d\mathbf{r'}_2 = \int d\mathbf{r'}_2$ to get

$$\left\langle \tilde{i}_l^{\mathbf{k}_1} \tilde{j}_m^{\mathbf{k}_2} \middle| r_{12}^{-1} \middle| \tilde{a}_n^{\mathbf{k}_3} \tilde{b}^{\mathbf{k}_4} \right\rangle_\mathcal{V} = \sum_{L'M'N'}^{\infty} \int d\mathbf{r'}_1 \int_\mathcal{V} d\mathbf{r'}_2\, i_l^{\mathbf{k}_1}(\mathbf{r'}_1 - \mathbf{R}_{L'}) j_l^{\mathbf{k}_2}(\mathbf{r'}_2 - \mathbf{R}_{M'}) \frac{1}{|\mathbf{r'}_1 - \mathbf{r'}_2|} a_l^{\mathbf{k}_3}(\mathbf{r'}_1 - \mathbf{R}_{N'}) b^{\mathbf{k}_4}(\mathbf{r'}_2) \tag{3.66}$$

We can again drop the primes over the dummy variables for convenience, and express the integrals as

$$\left\langle \tilde{i}_l^{\mathbf{k}_1} \tilde{j}_m^{\mathbf{k}_2} \middle| r_{12}^{-1} \middle| \tilde{a}_n^{\mathbf{k}_3} \tilde{b}^{\mathbf{k}_4} \right\rangle_{\mathcal{V}} = \sum_{LMN}^{\infty} \left\langle i_{l+L}^{\mathbf{k}_1} j_{m+M}^{\mathbf{k}_2} \middle| r_{12}^{-1} \middle| a_{n+N}^{\mathbf{k}_3} b^{\mathbf{k}_4} \right\rangle \tag{3.67}$$

Finally, we can express the Coulomb integrals over Bloch orbitals as

$$\langle i_{\mathbf{k}_1} j_{\mathbf{k}_2} | r_{12}^{-1} | a_{\mathbf{k}_3} b_{\mathbf{k}_4} \rangle_{\mathcal{V}} = \delta_{\mathbf{k}_1 - \mathbf{k}_3, \mathbf{k}_4 - \mathbf{k}_2 + \mathbf{G}} \frac{1}{N_{\mathbf{k}}} \sum_{lmn}^{N_{\mathbf{k}}} e^{i(\mathbf{k}_1 \cdot \mathbf{R}_l + \mathbf{k}_2 \cdot \mathbf{R}_m - \mathbf{k}_3 \cdot \mathbf{R}_n)} \sum_{LMN}^{\infty} \left\langle i_{l+L}^{\mathbf{k}_1} j_{m+M}^{\mathbf{k}_2} \middle| r_{12}^{-1} \middle| a_{n+N}^{\mathbf{k}_3} b^{\mathbf{k}_4} \right\rangle \tag{3.68}$$

While the Bloch orbitals form an orthonormal set, $\langle p_{\mathbf{k}} | q_{\mathbf{k}'} \rangle = \delta_{pq} \delta_{\mathbf{k}\mathbf{k}'}$, the functions $\{p_l^{\mathbf{k}}\}$ do not

$$\left\langle p_l^{\mathbf{k}} \middle| q^{\mathbf{k}'} \right\rangle = \sum_{\mu\nu} C_{\mu p}^{\mathbf{k}} S_{\mu\nu}^{l} C_{\nu q}^{\mathbf{k}'} \quad \text{with} \quad p_l^{\mathbf{k}}(\mathbf{r}) = \sum_{\mu} C_{\mu p}^{\mathbf{k}}(\mathbf{r}) \tilde{\mu}_l(\mathbf{r}) \tag{3.69}$$

where, $S_{\mu\nu}^{l}$ is defined in Equation (3.43). In periodic systems, the contributions to the integrals in the Bloch orbital basis are spread over the entire crystal, unlike molecules, where they are located at one place. Therefore, the integrals decay at a slower rate than in molecules. Therefore, applying local approximations is generally not suitable in the Bloch orbital formulation.

3.5 Wannier Functions

Bloch orbitals are eigenstates of the translation operator and the electronic Hamiltonian. In this sense, they are localised in energy. However, they remain spatially delocalised throughout the supercell. Therefore, Bloch orbitals are not suitable for a local correlation treatment. We seek to have an orthogonal basis that spans the same space as the occupied Bloch orbitals, while retaining the system's translational symmetry. Such a basis is provided by Wannier functions, which can be obtained by the Fourier transform of the Bloch orbitals as

$$\tilde{i}(\mathbf{r} - \mathbf{R}_l) = \frac{1}{\sqrt{N_{\mathbf{k}}}} \sum_{\mathbf{k}}^{N_{\mathbf{k}}} i_{\mathbf{k}}(\mathbf{r}) e^{-i\mathbf{k} \cdot \mathbf{R}_l} \tag{3.70}$$

where $i_k(\mathbf{r})$ is a Bloch orbital defined in Equation (3.45). We get $N_{\mathbf{k}}$ Wannier functions, which span the same space as that spanned by the $N_{\mathbf{k}}$ Bloch orbitals. The Wannier function $\tilde{i}(\mathbf{r} - \mathbf{R}_l)$ is centred in the cell associated with lattice vector $\mathbf{R}_l$. Each of the $N_{\mathbf{k}}$ Wannier functions is assigned to a unique cell given by $\mathbf{R}_l$. Thus, while Bloch orbitals are characterised by wavevector $\mathbf{k}$ and band index i, Wannier functions are characterised by real space cell index l and band in-

dex i. Wannier functions corresponding to a given band in different cells are simply translation copies of each other. In other words, all Wannier functions can be generated by translating the set of Wannier functions centred in a reference cell.

$$\begin{aligned}\tilde{i}(\mathbf{r}-\mathbf{R}_l) &= \frac{1}{\sqrt{N_\mathbf{k}}}\sum_{\mathbf{k}}^{N_\mathbf{k}} i_\mathbf{k}(\mathbf{r})e^{-i\mathbf{k}\cdot\mathbf{R}_l} \\ &= \frac{1}{\sqrt{N_\mathbf{k}}}\sum_{\mathbf{k}}^{N_\mathbf{k}} i_\mathbf{k}(\mathbf{r}-\mathbf{R}_l) \\ &= \frac{1}{\sqrt{N_\mathbf{k}}}\sum_{\mathbf{k}}^{N_\mathbf{k}} e^{i\mathbf{k}\cdot\mathbf{0}} i_\mathbf{k}(\mathbf{r}-\mathbf{R}_l) \\ &= \tilde{i}(\mathbf{r}-\mathbf{R}_l-\mathbf{R}_0)\end{aligned} \tag{3.71}$$

where the cell with lattice vector $\mathbf{R}_0 = \mathbf{0}$ is chosen to be the reference cell. Unlike Bloch functions, Wannier functions are not eigenstates of the Hamiltonian, so they are not localised in energy, but they are usually spatially localised near their centres. Moreover, Wannier functions are real, provided Bloch functions fulfil time-reversal symmetry, $i_\mathbf{k} = i^*_{-\mathbf{k}}$. Due to the orthogonality of Bloch orbitals, Wannier functions retain the orthogonality between bands, and notably, they form an orthonormal set for a given band with respect to cells in the supercell

$$\begin{aligned}\int \tilde{i}^*(\mathbf{r}-\mathbf{R}_l)\tilde{j}(\mathbf{r}-\mathbf{R}_m)d^3(\mathbf{r}) &= \frac{1}{N_\mathbf{k}}\sum_{\mathbf{k},\mathbf{k}'}^{N_\mathbf{k}} \int e^{i\mathbf{k}\cdot\mathbf{R}_l} i^*_\mathbf{k}(\mathbf{r}) e^{-i\mathbf{k}'\cdot\mathbf{R}_m} j_{\mathbf{k}'}(\mathbf{r})d^3(\mathbf{r}) \\ &= \frac{1}{N_\mathbf{k}}\sum_{\mathbf{k},\mathbf{k}'}^{N_\mathbf{k}} e^{i\mathbf{k}\cdot\mathbf{R}_l} e^{-i\mathbf{k}'\cdot\mathbf{R}_m}\ \delta_{ij}\ \delta_{\mathbf{k}\mathbf{k}'} \\ &= \frac{1}{N_\mathbf{k}}\delta_{ij}\sum_{\mathbf{k}}^{N_\mathbf{k}} e^{i\mathbf{k}\cdot(\mathbf{R}_l-\mathbf{R}_m)} \\ &= \delta_{ij}\ \delta_{lm}\end{aligned} \tag{3.72}$$

The most interesting property of Wannier functions is that they are not uniquely defined. This is due to the inherent gauge freedom in Bloch functions, which are only defined up to an arbitrary phase $\phi(\mathbf{k})$. In other words, for every wavevector $\mathbf{k}$, the Bloch functions have phase indeterminacy. Therefore, a gauge transformation of a Bloch orbital for a given wavevector changes the resulting Wannier function.

$$i_\mathbf{k}(\mathbf{r}) \longrightarrow e^{i\phi(\mathbf{k})} i_\mathbf{k}(\mathbf{r}) \implies \text{different } \tilde{i}(\mathbf{r}) \tag{3.73}$$

The above gauge transformation can be generalised for a group of bands (which may be connected via degeneracies) through a unitary transformation $U^{\mathbf{k}}_{ji}$ which mixes the Bloch orbitals from the group of bands, resulting in generalised Wannier functions

$$\tilde{i}(\mathbf{r}) = \frac{1}{\sqrt{N_{\mathbf{k}}}} \sum_{\mathbf{k}}^{N_{\mathbf{k}}} \sum_{j} j_{\mathbf{k}}(\mathbf{r}) U^{\mathbf{k}}_{ji} \tag{3.74}$$

The generalised Wannier functions are even more strongly non-unique than those obtained by the Fourier transform of Bloch orbitals, as their locality depends on the relative phases of multiple bands. This phase indeterminacy in Bloch orbitals can be exploited to improve the locality of Wannier functions. Therefore, considering the local correlation treatment, we seek to obtain optimally localised Wannier functions that span the same space as the occupied Bloch orbitals. Localised MOs are commonly employed in molecular electronic structure calculations, and localised Wannier functions can be regarded as the periodic solid equivalent of such localised MOs. As discussed in Section 2.10, localised MOs are routinely computed by minimising some locality measures. Such an approach can also be extended to localise Wannier functions. To that end, several attempts have been made to compute Wannier functions with improved locality[123–131] but the algorithm introduced by Marzari and Vanderbilt has been the most widely used[132,133]. Their localisation algorithm iteratively minimises the Foster-Boys functional to obtain what are known as *maximally-localised Wannier functions*. In this work, we have developed a straightforward and non-iterative procedure to localise the Wannier functions using Cholesky decomposition as motivated by the discussion in Section 2.10.5.

3.6 Localised Wannier Orbitals

The central idea of our algorithm to obtain localised Wannier functions is to impose the locality of the Bloch orbitals at the Γ-point onto the corresponding Bloch orbitals for the other **k**-points. The localisation procedure consists of the following three steps:

1. We start by localising the Γ-point, which can be achieved by using one of the localisation schemes described in Section 2.10. As a first approximation, we simply compute Cholesky orbitals $\mathbf{L}^{\Gamma}$ from the density matrix $\mathbf{D}^{\Gamma}$ corresponding to the occupied manifold

at the Γ-point

$$D^{\Gamma}_{\mu\nu} = \sum_{i}^{occ} C^{\Gamma}_{\mu i} C^{\Gamma}_{\nu i} = \sum_{i}^{occ} L^{\Gamma}_{\mu i} L^{\Gamma}_{\nu i} \tag{3.75}$$

Here, $\mathbf{C}^{\Gamma}$ represents the coefficient matrix for expanding the occupied Bloch orbitals in terms of AOs. Because $C^{\Gamma}_{\mu i} \in \mathbb{R}$, the Bloch orbitals at the Γ-point are real. The dimension of the density matrix $\mathbf{D}^{\Gamma}$ corresponds to the number of AOs, but it has the rank of the number of occupied orbitals. Thus, $\mathbf{D}^{\Gamma}$ is positive semidefinite.

We apply a pivoted Cholesky decomposition to $\mathbf{D}^{\Gamma}$, yielding Cholesky vectors $\mathbf{L}^{\Gamma}$ associated with the occupied space. Consequently, the dimension of the matrix corresponding to the Cholesky vectors is equal to the number of occupied orbitals. This truncates the dimension of the AOs to match the rank of $\mathbf{D}^{\Gamma}$. As a result of this truncation, the Cholesky orbitals are localised.

2. We now enforce the locality of the Γ-point Bloch orbitals onto the other **k**-points by applying a unitary transformation that returns a coefficient matrix with the minimum least-squares difference from that of the Γ-point

$$\min_{\mathbf{U}^{\mathbf{k}}} \left\| L^{\Gamma}_{\nu i} - \sum_{j} C^{\mathbf{k}}_{\nu j} U^{\mathbf{k}}_{ji} \right\|^2 \tag{3.76}$$

where **U** is a unitary matrix that maps the **k**-point coefficients to that of the Γ-point. The coefficients of the Γ-point being real enforces the gauge of the coefficients of the other **k**-points to have minimal imaginary component. Finding **U** is an orthogonal procrustes problem which can be solved by performing Singular Value Decomposition (SVD) of the overlap matrix **M** given as

$$\begin{aligned} \mathbf{M}^{\mathbf{k}} &= \tilde{\mathbf{U}} \mathbf{\Sigma}^{\mathbf{k}} (\tilde{\mathbf{V}}^{\mathbf{k}})^{\dagger} \\ \text{where } \; M^{\mathbf{k}}_{ij} &= \sum_{\mu\nu} L^{\Gamma}_{\mu i} S^{\Gamma}_{\mu\nu} C^{\mathbf{k}}_{\nu j} \end{aligned} \tag{3.77}$$

Here, $\mathbf{S}^{\Gamma}$ represents the overlap between AOs at the Γ-point. This gives us the desired unitary transformation that maps between the coefficients of the Γ-point and those of a **k**-point

$$\mathbf{U}^{\mathbf{k}} = \tilde{\mathbf{V}}^{\mathbf{k}} (\tilde{\mathbf{U}}^{\mathbf{k}})^{\dagger} \tag{3.78}$$

The coefficients $\tilde{\mathbf{C}}^{\mathbf{k}}$ of the localised Bloch orbitals can thus be obtained as

$$\tilde{C}^{\mathbf{k}}_{\mu i} = \sum_{j} C^{\mathbf{k}}_{\mu j} U^{\mathbf{k}}_{ji} \tag{3.79}$$

The localised Bloch orbitals $\tilde{i}_{\mathbf{k}}$ are then given by

$$\tilde{i}_{\mathbf{k}} = \sum_{\mu} \tilde{C}^{\mathbf{k}}_{\mu i}\, \mu_{\mathbf{k}}(\mathbf{r}) \tag{3.80}$$

Since we have imposed the locality of the Γ-point Bloch orbitals onto each of the other **k**-points, the coefficients of Bloch orbitals are expected to vary smoothly with wavevector **k**.

3. Finally, we Fourier transform the smoothly varying Bloch orbitals to obtain localised Wannier functions

$$\tilde{i}_l(\mathbf{r}) = \frac{1}{\sqrt{N_{\mathbf{k}}}} \sum_{\mathbf{k}}^{N_{\mathbf{k}}} \tilde{i}_{\mathbf{k}} e^{-i\mathbf{k}\cdot\mathbf{R}_l} \tag{3.81}$$

which can be fully expanded in the LCAO basis using Equation (3.80) and Equation (3.44) as

$$\tilde{i}_l(\mathbf{r}) = \frac{1}{N_{\mathbf{k}}} \sum_{\mu}^{AOs} \sum_{l'}^{N_{\mathbf{k}}} \sum_{\mathbf{k}}^{N_{\mathbf{k}}} \tilde{\mu}_{l'}(\mathbf{r})\, e^{i\mathbf{k}\cdot\mathbf{R}_{l'}}\, \tilde{C}^{\mathbf{k}}_{\mu i}\, e^{-i\mathbf{k}\cdot\mathbf{R}_l} \tag{3.82}$$

Although the original Wannier functions have contributions from each of the $N_{\mathbf{k}}$ unit cells in the supercell, the Fourier transform of Bloch orbitals varying smoothly with **k** results in well-localised Wannier functions that are located primarily in one unit cell.

3.7 Periodic Local MP2 with Wannier Orbitals

Using Equation (2.109), the residual equation to obtain MP2 amplitudes in the basis of generalised Wannier orbitals can be expressed as

$$g^{\tilde{i}_{l_1}\tilde{j}_{l_2}}_{\tilde{a}_{l_3}\tilde{b}_{l_4}} + \sum_{\tilde{c}_{l_5}} \left(f^{\tilde{c}_{l_5}}_{\tilde{a}_{l_3}} t^{\tilde{i}_{l_1}\tilde{j}_{l_2}}_{\tilde{c}_{l_5}\tilde{b}_{l_4}} + f^{\tilde{c}_{l_5}}_{\tilde{b}_{l_4}} t^{\tilde{i}_{l_1}\tilde{j}_{l_2}}_{\tilde{a}_{l_3}\tilde{c}_{l_5}} \right) - \sum_{\tilde{k}_{l_5}} \left(f^{\tilde{k}_{l_5}}_{\tilde{i}_{l_1}} t^{\tilde{k}_{l_5}\tilde{j}_{l_2}}_{\tilde{a}_{l_3}\tilde{b}_{l_4}} + f^{\tilde{k}_{l_5}}_{\tilde{j}_{l_2}} t^{\tilde{i}_{l_1}\tilde{k}_{l_5}}_{\tilde{a}_{l_3}\tilde{b}_{l_4}} \right) = 0 \tag{3.83}$$

where, $g^{\tilde{i}_{l_1}\tilde{j}_{l_2}}_{\tilde{a}_{l_3}\tilde{b}_{l_4}} = \left\langle \tilde{i}_{l_1}\tilde{j}_{l_2} \middle\| \tilde{a}_{l_3}\tilde{b}_{l_4} \right\rangle_{\mathcal{V}}$ are the Coulomb repulsion integrals between Wannier orbitals. In principle, similar to the case of Bloch orbitals, the integrals in the Wannier orbital basis

extend beyond the supercell as periodic boundary conditions require Wannier orbitals to be periodic over the supercell:

$$\left\langle \tilde{i}_{l_1} \tilde{j}_{l_2} \middle| r_{12}^{-1} \middle| \tilde{a}_{l_3} \tilde{b}_{l_4} \right\rangle_{\mathcal{V}} = \sum_{L_2 L_3 L_4}^{\infty} \left\langle \tilde{i}_{l_1} \tilde{j}_{l_2+L_2} \middle| r_{12}^{-1} \middle| \tilde{a}_{l_3+L_3} \tilde{b}_{l_4+L_4} \right\rangle . \tag{3.84}$$

where we have shifted the centre of the sum to the supercell indexed L_2. The Fock matrices in the Wannier orbital basis are derived from the Fourier transform of the Fock matrices in the Bloch orbital basis

$$f_{p_l}^{q_m} = \langle \tilde{p}_l | \hat{F} | \tilde{q}_m \rangle = \frac{1}{N_{\mathbf{k}}} \sum_{\mathbf{k}} e^{i\mathbf{k}\cdot(\mathbf{R}_l - \mathbf{R}_m)} f_{p\mathbf{k}}^{q\mathbf{k}} = \sum_{\mathbf{k}} V_{\mathbf{k}l} f_{p\mathbf{k}}^{q\mathbf{k}} V_{\mathbf{k}m}^{*} \tag{3.85}$$

where $V_{\mathbf{k}l} = \frac{1}{\sqrt{N_{\mathbf{k}}}} e^{i\mathbf{k}\cdot\mathbf{R}_l}$ is an element of the the unitary matrix $\mathbf{V}$ which applies the Fourier transform. By choosing cell l_1 as the reference cell denoted as $\mathbf{0}$, the MP2 energy per unit cell is obtained as

$$E_{MP2} = \frac{1}{4N_{\mathbf{k}}} \sum_{\tilde{i}_{\mathbf{0}} \tilde{j}_{l_2}} \sum_{\tilde{a}_{l_3} \tilde{b}_{l_4}} g_{\tilde{a}_{l_3} \tilde{b}_{l_4}}^{\tilde{i}_{\mathbf{0}} \tilde{j}_{l_2}} t_{\tilde{a}_{l_3} \tilde{b}_{l_4}}^{\tilde{i}_{\mathbf{0}} \tilde{j}_{l_2}} \tag{3.86}$$

If the Wannier orbitals are sufficiently localised so that those within the supercell form an orthonormal set across the entire crystal,

$$\langle \tilde{p}_{l+L} | \tilde{q}_{m+M} \rangle = \delta_{pq}\, \delta_{lm}\, \delta_{LM}, \tag{3.87}$$

then we can ignore the periodic boundary conditions and focus solely on the supercell. Thus, all references to the BvK supercell may be dropped in the MP2 amplitudes equations, and local approximations can be introduced in the same way as for the molecular case. To ensure that Wannier orbitals closely adhere to orthogonality throughout the crystal, it is important to generate them using expanded supercells. In other words, if the supercell is not large enough, the Wannier orbitals may not be sufficiently localised, and in such a case, dropping the periodic boundary conditions may become a crude approximation.

3.8 BvK Supercell PAOs

We now turn to the local representation of the virtual space within the BvK supercell, beginning with PAOs. The real-space virtual orbitals, $|a_l\rangle$, are constructed by Fourier transforming the

virtual space Bloch orbitals obtained from a periodic HF calculation. The supercell PAOs, $|\check{\mu}_l\rangle$, are then determined by projecting the supercell AOs $|\tilde{\mu}_l\rangle$ onto this virtual space as

$$|\check{\mu}_l\rangle = \sum_{a_{l'}} |a_{l'}\rangle \langle a_{l'}|\tilde{\mu}_l\rangle \tag{3.88}$$

The supercell PAOs can be expanded in the AO basis using a coefficient matrix $\hat{\mathbf{C}}$

$$|\check{\mu}_l\rangle = \sum_{\nu_{l'}} |\nu_{l'}\rangle \hat{C}^{\mu_l}_{\nu_{l'}} \tag{3.89}$$

Similar to Equation (2.130), the coefficient matrix can be expressed as

$$\hat{C}^{\mu_l}_{\nu_{l'}} = \sum_{a_{n'}\kappa_n} C^{a_{n'}}_{\nu_{l'}} C^{a_{n'}}_{\kappa_n} S^{\kappa_n}_{\mu_l} \tag{3.90}$$

where, just as in Equation (3.43), the overlap integral $S^{\kappa_n}_{\mu_l}$ between (non-periodic) AOs $|\mu_{l+L}\rangle$ and $|\kappa_n\rangle$ is given as

$$S^{\kappa_n}_{\mu_l} = \sum_{L}^{\infty} \langle \mu_{l+L}|\kappa_n\rangle \tag{3.91}$$

Since the supercell AOs possess the periodicity of the lattice, PAOs also exhibit translational symmetry, $\hat{C}^{\mu_l}_{\nu_{l'}} = \hat{C}^{\mu_\mathbf{0}}_{\nu_{l'-l}}$. Similar to the molecular case, the supercell PAOs can be uniquely expressed in terms of the virtual orbitals as

$$|\check{\mu}_l\rangle = \sum_{a_{l'}} |a_{l'}\rangle \hat{C}^{a_{l'}}_{\mu_l} \quad \text{with} \quad \hat{C}^{a_{l'}}_{\mu_l} = \sum_{\kappa_n} C^{a_{l'}}_{\kappa_n} S^{\kappa_n}_{\mu_l} \tag{3.92}$$

Since PAOs form a non-orthogonal set, the virtual orbitals are expanded in a contravariant PAO basis given by coefficients $\tilde{C}^{\mu_l}_{a_{l'}}$ as

$$|a_{l'}\rangle = \sum_{\check{\mu}_l} |\check{\mu}_l\rangle \tilde{C}^{\mu_l}_{a_{l'}} \tag{3.93}$$

As discussed in Section 2.11.1, the contravariant coefficients $\tilde{C}^{\mu_l}_{a_{l'}}$ are obtained by taking the Moore-Penrose pseudoinverse of $\hat{C}^{a_{l'}}_{\mu_l}$.

3.9 BvK Supercell OSVs

As discussed in Section 2.11.2.1, OSVs serve as a means to accelerate the construction of PNOs. In this section, we outline how OSVs are generated under periodic boundary conditions as intermediates for PNOs. The OSV space for each Wannier orbital $\left|\tilde{i}_l\right\rangle$ is obtained by diagonalising the external density matrix for the Wannier orbital pair $\left|\tilde{i}_l\tilde{i}_l\right\rangle$. For each pair, the external density matrix is constructed using PAOs $|\breve{\mu}_l\rangle\ s \in \mathcal{D}_{\tilde{i}_l}$ selected using the principal domain approach[134]. The first-order (MP1) amplitudes required for the construction of the external density matrices are approximated by using a numerical Laplace transformation. This approach decouples nested summations that involve energy denominators from amplitude equations, making amplitude determination computationally efficient[95]. To do this, we require Laplace-transformed supercell PAOs $\left|\breve{\mu}_l^z\right\rangle$, which can be generated by projecting the supercell PAOs onto the canonical Bloch orbitals and multiplying by an exponential function as

$$\left|\breve{\mu}_l^z\right\rangle = \sum_{a_\mathbf{k}} |a_\mathbf{k}\rangle \langle a_\mathbf{k}|\tilde{\mu}_l\rangle\, e^{-(\varepsilon_a^\mathbf{k}-\varepsilon_F)t_z} \tag{3.94}$$

$$= \sum_{\nu_{l'}} |\nu_{l'}\rangle\, \hat{C}_{\nu_{l'}}^{\mu_l,z} \tag{3.95}$$

where, ε_F is the energy corresponding to the Fermi level and $\varepsilon_a^\mathbf{k}$ is the orbital eigenvalue corresponding to the canonical Bloch orbital $|a_\mathbf{k}\rangle$. t_z is the exponential coefficient of the quadrature grid point z. In the second line, we have expressed the overall transformation from AOs to Laplace transformed PAOs using the expansion coefficients $\hat{C}_{\nu_{l'}}^{\mu_l,z}$, which are defined to be

$$\hat{C}_{\nu_{l'}}^{\mu_l,z} = \sum_{a_n\kappa_m} \sum_{n'} C_{\nu_{l'}}^{a_{n'}}\ L_{n'n}^{a,z}\ C_{\kappa_m}^{a_n}\ S_{\mu_l}^{\kappa_m} \tag{3.96}$$

where $L_{n'n}^{a,z}$ is the contribution coming from the sum of the exponentials over all $\mathbf{k}$-points,

$$L_{n'n}^{a,z} = \sum_\mathbf{k}\ V_{\mathbf{k}n'}^*\ e^{-(\varepsilon_a^\mathbf{k}-\varepsilon_F)t_z}\ V_{\mathbf{k}n} \tag{3.97}$$

The Laplace transformed PAOs also retain the translational symmetry; therefore, $\left|\breve{\mu}_l^z\right\rangle$ are all translational copies of $\left|\breve{\mu}_\mathbf{0}^z\right\rangle$. The MP1 amplitudes $t_{\breve{\nu}\breve{\kappa}}^{\tilde{i}_l\tilde{i}_l}$ are then defined in terms of the two-electron integrals between the Wannier orbital pair and the Laplace transformed PAOs over the

BvK supercell weighted by a quadrature parameter w_z

$$t^{\tilde{i}_l\tilde{i}_l}_{\check{\nu}\check{\kappa}} = \sum_z w_z \left\langle \check{\nu}^z \check{\kappa}^z \middle| \tilde{i}_l \tilde{i}_l \right\rangle_{BvK} \tag{3.98}$$

The elements of the external pair density matrix are then obtained as

$$D^{\check{\nu}}_{\check{\mu}} = \sum_{\kappa} 4 t^{\tilde{i}_l\tilde{i}_l}_{\check{\mu}\check{\kappa}} \; t^{\tilde{i}_l\tilde{i}_l}_{\check{\nu}\check{\kappa}}. \tag{3.99}$$

diagonalising this density matrix yields as eigenvectors, OSVs $\{\bar{a}\}$, corresponding to the Wannier orbital $\left|\tilde{i}_l\right\rangle$, with their occupation numbers $n_{\bar{a}}$ obtained as eigenvalues

$$\sum_{\tilde{\nu}} D^{\check{\nu}}_{\check{\mu}} C^{\check{\nu}}_{\bar{a}} = \sum_{\check{\nu}} S^{\check{\nu}}_{\check{\mu}} C^{\check{\nu}}_{\bar{a}} n_{\bar{a}}, \tag{3.100}$$

where $S^{\check{\nu}}_{\check{\mu}}$ represents the overlap between PAOs, $|\check{\mu}\rangle$ and $|\check{\nu}\rangle$, integrated over the BvK supercell. The coefficients $C^{\check{\nu}}_{\bar{a}}$ define the transformation from PAOs $|\check{\nu}\rangle$ to OSVs $|\bar{a}\rangle$, and are specific to each Wannier orbital $\left|\tilde{i}_l\right\rangle$. Like PAOs, OSVs also retain translational symmetry–OSVs for every $\left|\tilde{i}_l\right\rangle$ are translational copies of the OSVs for $\left|\tilde{i}_{\mathbf{0}}\right\rangle$. Consequently, it is sufficient to compute the OSVs only for the reference cell. The OSV space is then truncated based on a user-defined threshold, retaining only those OSVs which correspond to occupation numbers greater than the specified threshold.

Having obtained PAOs and OSVs for every Wannier orbital, we construct initial PAO pair domains $\mathcal{D}_{\tilde{i}_{\mathbf{0}}\tilde{j}_l}$, and pair-specific virtuals $\{\bar{a}_{\tilde{i}_{\mathbf{0}}\tilde{j}_l}\}$ for each pair $\left|\tilde{i}_{\mathbf{0}}\tilde{j}_l\right\rangle$ by merging the respective PAO and OSV domains for Wannier orbitals $\left|\tilde{i}_{\mathbf{0}}\right\rangle$ and $\left|\tilde{j}_l\right\rangle$. The first-order amplitudes are then computed using the semi-canonical approximation. This means that the pair-specific virtuals become orthonormal and diagonalise the Fock matrix in the subspace formed by the OSVs corresponding to a given pair. This is practically achieved by orthogonalizing the orbitals in each subspace (typically, using SVD to remove linear dependencies), and then diagonalising the Fock matrix in the basis of the orthogonal orbitals so that, $f^{\bar{b}}_{\bar{a}} = \varepsilon_{\bar{a}}\delta^{\bar{b}}_{\bar{a}}$. Finally, the OSV-SOS-MP2 energy is computed to approximate pair energies, enabling the elimination of insignificant

pairs while also providing an estimate of their contribution to the total energy

$$E_{SOS}^{\tilde{i}_l\tilde{j}_m} = \sum_{\bar{a}\in[\tilde{i}_l]\bar{b}\in[\tilde{j}_m]} \frac{(g_{\bar{a}\bar{b}}^{\tilde{i}_l\tilde{j}_m})^2}{f_{\tilde{i}_l}^{\tilde{i}_l} + f_{\tilde{j}_m}^{\tilde{j}_m} - \varepsilon_{\bar{a}} - \varepsilon_{\bar{b}}} = \sum_{\bar{a}\in[\tilde{i}_l]\bar{b}\in[\tilde{j}_m]} t_{\bar{a}\bar{b}}^{\tilde{i}_l\tilde{j}_m}\, g_{\bar{a}\bar{b}}^{\tilde{i}_l\tilde{j}_m} \tag{3.101}$$

where, the first-order amplitudes $t_{\bar{a}\bar{b}}^{\tilde{i}_l\tilde{j}_m}$ are given as

$$t_{\bar{a}\bar{b}}^{\tilde{i}_l\tilde{j}_m} = \frac{g_{\bar{a}\bar{b}}^{\tilde{i}_l\tilde{j}_m}}{f_{\tilde{i}_l}^{\tilde{i}_l} + f_{\tilde{j}_m}^{\tilde{j}_m} - \varepsilon_{\bar{a}} - \varepsilon_{\bar{b}}}. \tag{3.102}$$

The OSV-SOS-MP2 energy excludes exchange contributions, and the Coulomb integrals can be efficiently evaluated using density fitting.

3.10 Periodic Local MP2 with PNOs

We then proceed to compute the external density matrices for each significant pair using the first-order amplitudes as

$$D_{\bar{a}\bar{b}}^{\tilde{i}_l\tilde{j}_m} = 2\sum_{\bar{c}} \left(t_{\bar{a}\bar{c}}^{\tilde{i}_l\tilde{j}_m}\, u_{\bar{b}\bar{c}}^{\tilde{i}_l\tilde{j}_m} + t_{\bar{c}\bar{a}}^{\tilde{i}_l\tilde{j}_m}\, u_{\bar{c}\bar{b}}^{\tilde{i}_l\tilde{j}_m} \right) \tag{3.103}$$

where,

$$u_{\bar{a}\bar{b}}^{\tilde{i}_l\tilde{j}_m} = 2t_{\bar{a}\bar{b}}^{\tilde{i}_l\tilde{j}_m} - t_{\bar{b}\bar{a}}^{\tilde{i}_l\tilde{j}_m}. \tag{3.104}$$

The eigenvectors $\{\tilde{a}\}$ for each pair obtained by diagonalising the external density matrices are our desired PNOs,

$$\sum_{\bar{c}} D_{\bar{b}\bar{c}}^{\tilde{i}_l\tilde{j}_m}\, C_{\bar{c}\tilde{a}}^{\tilde{i}_l\tilde{j}_m} = n_{\tilde{a}}^{\tilde{i}_l\tilde{j}_m}\, C_{\bar{b}\tilde{a}}^{\tilde{i}_l\tilde{j}_m}. \tag{3.105}$$

PNOs, the corresponding integrals and the amplitudes remain translationally invariant, so PNOs for a pair $\left|\tilde{i}_l\tilde{j}_m\right\rangle$ are translational copies of those corresponding to $\left|\tilde{i}_{\mathbf{0}}\tilde{j}_l\right\rangle$, so we only need to compute the PNOs for $\left|\tilde{i}_{\mathbf{0}}\tilde{j}_l\right\rangle$. It is then straightforward to apply the semi-canonical approximation to the PNO subspace and compute the PNO-SC-MP2 energy for each pair as

$$E_{SC}^{\tilde{i}_l\tilde{j}_m} = \sum_{\bar{a}\bar{b}\in[\tilde{i}_l\tilde{j}_m]} u_{\bar{a}\bar{b}}^{\tilde{i}_l\tilde{j}_m}\, g_{\bar{a}\bar{b}}^{\tilde{i}_l\tilde{j}_m} \tag{3.106}$$

The PNO space is then truncated based on a user-defined threshold, T_{PNO}. Only PNOs with occupation numbers greater than the threshold, $n_{\tilde{a}} > T_{PNO}$, are retained. The difference between

the PNO-SC-MP2 energy before and after truncating the PNO space provides an estimate of the contribution of the discarded PNOs to the total energy. This difference added to the OSV-SOS-MP2 energy estimate for discarded pairs is referred to as the Δ correction. The final residual equations for periodic PNO-MP2 are analogous to those of non-periodic PNO-MP2,

$$\begin{aligned} & g_{\tilde{a}\tilde{b}}^{\tilde{i}_{\mathbf{0}}\tilde{j}_l} + (\varepsilon_{\tilde{a}} + \varepsilon_{\tilde{b}})\, t_{\tilde{a}\tilde{b}}^{\tilde{i}_{\mathbf{0}}\tilde{j}_l} \\ & - \sum_{k_m} \sum_{\tilde{c}\tilde{d}\in[k_m j_l]} S_{\tilde{a},\tilde{i}_{\mathbf{0}}\tilde{j}_l}^{\tilde{c},\tilde{k}_m\tilde{j}_l}\, S_{\tilde{b},\tilde{i}_{\mathbf{0}}\tilde{j}_l}^{\tilde{d},\tilde{k}_m\tilde{j}_l}\, t_{\tilde{c}\tilde{d}}^{\tilde{k}_m\tilde{j}_l}\, f_{\tilde{k}_m}^{\tilde{i}_{\mathbf{0}}} \\ & - \sum_{k_m} \sum_{\tilde{c}\tilde{d}\in[i_{\mathbf{0}}k_m]} S_{\tilde{a},\tilde{i}_{\mathbf{0}}\tilde{j}_l}^{\tilde{c},\tilde{i}_{\mathbf{0}}\tilde{k}_m}\, S_{\tilde{b},\tilde{i}_{\mathbf{0}}\tilde{j}_l}^{\tilde{d},\tilde{i}_{\mathbf{0}}\tilde{k}_m}\, t_{\tilde{c}\tilde{d}}^{\tilde{i}_{\mathbf{0}}\tilde{k}_m}\, f_{\tilde{k}_m}^{\tilde{j}_l} = 0 \end{aligned} \tag{3.107}$$

where $|\tilde{a}\rangle$ and $\left|\tilde{b}\right\rangle$ are PNOs in the domain of the pair $|i_{\mathbf{0}} j_l\rangle$, and $S_{\tilde{a},\tilde{i}_{\mathbf{0}}\tilde{j}_l}^{\tilde{c},\tilde{k}_m\tilde{j}_l}$ is the overlap between PNOs of two pairs, $|i_{\mathbf{0}} j_l\rangle$ and $|k_m j_l\rangle$. These residual equations are solved iteratively for every pair $|i_{\mathbf{0}} j_l\rangle$ to obtain fully optimised amplitudes in the truncated PNO basis. The correlation energy per unit cell is then evaluated as

$$E_{cell}^{(2)} = \sum_{\tilde{i}_{\mathbf{0}}\leq\tilde{j}_l} \sum_{\tilde{a}\tilde{b}\in[i_{\mathbf{0}} j_l]} (2g_{\tilde{a}\tilde{b}}^{\tilde{i}_{\mathbf{0}}\tilde{j}_l} - g_{\tilde{b}\tilde{a}}^{\tilde{i}_{\mathbf{0}}\tilde{j}_l})\, t_{\tilde{a}\tilde{b}}^{\tilde{i}_{\mathbf{0}}\tilde{j}_l} + \Delta \tag{3.108}$$

where, as mentioned previously, Δ is the correction term composed of energy estimates for discarded pairs and PNOs.

3.11 Periodic Density Fitting

In our periodic PNO-MP2 method, evaluating the two-electron integrals, also known as ERIs is one of the most computationally demanding steps. Density fitting (DF), also known as the Resolution of Identity (RI) approximation, is widely used to accelerate the computation of ERIs by simplifying the four-centre ERIs to three-centre and two-centre terms. While this method has been applied effectively in molecular systems, extending it to periodic systems introduces unique challenges, particularly in handling lattice summations. This section only outlines the primary challenge associated with periodic DF and summarises the core aspects of our DF approach. A detailed theoretical formulation of periodic DF adopted in our implementation can be found in the work of Burow *et al.*[120].

The DF approximation expresses the electron density $\rho(\mathbf{r})$ in terms of an auxiliary basis set as

$$\rho(\mathbf{r}) \approx \tilde{\rho}(\mathbf{r}) = \sum_{\nu} c_{\nu} \nu(\mathbf{r}) \tag{3.109}$$

where c_ν are fitting coefficients and $\nu(\mathbf{r})$ are the auxiliary basis functions. The coefficients are determined by minimising the Coulomb error function

$$D = \int \int (\rho(\mathbf{r}) - \tilde{\rho}(\mathbf{r})) g(\mathbf{r}, \mathbf{r}') (\rho(\mathbf{r}') - \tilde{\rho}(\mathbf{r}')) \, d\mathbf{r} \, d\mathbf{r}' \tag{3.110}$$

where $g(\mathbf{r}, \mathbf{r}') = \frac{1}{|\mathbf{r}-\mathbf{r}'|}$ is the Coulomb metric. The fitting condition leads to a system of linear equations

$$\mathbf{V}\mathbf{c} = \xi \tag{3.111}$$

where the elements of the matrix $\mathbf{V}$ and the right-hand side ξ are given by

$$V_{\mu\nu} = \int \int \mu(\mathbf{r}) g(\mathbf{r}, \mathbf{r}') \nu(\mathbf{r}') \, d\mathbf{r} \, d\mathbf{r}' \tag{3.112}$$

$$\xi_{\mu} = \int \int \rho(\mathbf{r}) g(\mathbf{r}, \mathbf{r}') \mu(\mathbf{r}') \, d\mathbf{r} \, d\mathbf{r}' \tag{3.113}$$

This system of linear equations must be solved to determine the fitting coefficients c_ν.

Using DF, the two-electron Coulomb repulsion integrals in a local MP2 treatment are expressed as

$$(ia|jb) \approx \sum_{PQ}^{[ij]_{fit}} (ia|Q)[\mathbf{V}^{-1}]_{PQ}(P|jb) \quad \text{with} \quad [\mathbf{V}]_{PQ} = (P|Q) \tag{3.114}$$

where, $|a\rangle$ and $|b\rangle$ are localised virtual orbitals, and the summation over auxiliary functions P and Q is limited to those that are in the domain, $[ij]_{fit}$, of localised occupied orbitals $|i\rangle$ and $|j\rangle$.

Long-range interactions play a crucial role in determining the total energy and electronic structure in periodic systems. When atom-centred basis functions are used in periodic systems, these long-range interactions may be characterised by non-overlapping orbitals, and are essentially electrostatic in nature. The Coulomb metric inherently includes these long-range contributions. The three longest-range electrostatic interactions are of type: charge-charge, charge-dipole, and dipole-dipole interactions. Each of these interactions exhibits a characteristic decay behaviour with distance R, which affects the convergence of their lattice summation[135,136]. Charge-charge

interactions decay as $1/R$, charge-dipole interactions as $1/R^2$, while dipole-dipole interactions decay as $1/R^3$. In a periodic lattice, the number of interacting pairs at a distance R increases with the surface area of a hypersphere in the respective dimension. Thus, in 1D, the number of pairs grow linearly with R, while in 2D, the number of pairs grows quadratically with R, and in 3D, the growth is cubic with R. Consequently, the lattice sum of electrostatic interactions behaves differently depending on the dimensionality. Charge-charge interactions remain divergent in 1D, 2D and 3D. The divergence arises because the strength of the interaction decreases too slowly compared to the growth in the number of interaction pairs. Although charge-dipole interactions decay more rapidly as $1/R^2$, their lattice sums can sometimes still pose a challenge in 3D systems and therefore often must be eliminated or corrected for in practical computations. Dipole-dipole interactions, with a decay rate of $1/R^3$, are typically convergent in 1D and 2D systems. In 3D systems, however, the convergence of dipole-dipole interactions becomes conditional and depends on the lattice summation method or the unit cell definition.

The total charge distribution in a periodic system is given by

$$\rho_{\text{crystal}} = \sum_l \rho_l \tag{3.115}$$

where ρ_l represents the local charge density centred in unit cell l. This total charge distribution can be approximated by an auxiliary charge distribution $\tilde{\rho}_{\text{crystal}}$ as

$$\rho_{\text{crystal}} \approx \tilde{\rho}_{\text{crystal}} = \sum_l \tilde{\rho}_l = \sum_\alpha c_\alpha \alpha_l \tag{3.116}$$

ERIs in MP2 theory only involve chargeless densities of the form $\rho(\mathbf{r}) = |ia\rangle$, representing excitations from occupied orbital $|i\rangle$ to virtual orbital $|a\rangle$, so there are no charge-charge interactions. In the DF approximation, the densities are expanded using an auxiliary basis set, which can inadvertently introduce charged components, leading to divergence in MP2 integrals due to lattice summation. To mitigate this, it is essential to ensure that the fitted densities remain charge-neutral. This is achieved by decomposing the auxiliary charge density into charged and chargeless components

$$\tilde{\rho} = \tilde{\rho}^{(c)} + \tilde{\rho}^{(n)} \tag{3.117}$$

where $\tilde{\rho}^{(c)}$ is the charged component and $\tilde{\rho}^{(n)}$ is the chargeless component. Then the particular

linear combination of s-type functions which are typically associated with a charge is projected out using the projector **P** defined as

$$\mathbf{P} = \mathbf{1} - \mathbf{n}\mathbf{n}^T \tag{3.118}$$

where **n** are normalised charge vectors constructed using the charges of auxiliary basis functions as described by Burow *et al.* in Ref. 120. The expression for density-fitted integrals in local MP2 framework given by Equation (3.114) then becomes

$$(ia|jb) \approx \sum_{PQ}^{[ij]_{fit}} (ia|Q)[\tilde{\mathbf{V}}^{-1}]_{PQ}(P|jb) \quad \text{where} \quad \tilde{\mathbf{V}} = \mathbf{PVP}. \tag{3.119}$$

By removing charged components, the fitted density retains its charge neutrality, preventing divergence of integrals.

For DF in periodic HF calculations in TURBOMOLE, certain contributions of the charged component are reintroduced into the fitted chargeless density[120], ensuring that the external potential is cancelled exactly. In contrast, since the density functions are inherently chargeless in MP2 due to the orthogonality between the occupied and virtual spaces, the charged component is not reintroduced into the final fitted density.

Despite enforcing charge neutrality, dipole–dipole interactions remain challenging in periodic systems due to the conditional convergence of finite lattice sums. In particular, 3D periodic systems with a unit cell possessing a non-zero dipole moment require additional correction terms to ensure the convergence of density-fitted Coulomb integrals. To address this, we adopt a dipole correction scheme based on the approach of Kudin and Scuseria[137], wherein a fictitious surface layer of point charges is introduced on the boundary of the supercell. This surface charge distribution is designed to cancel the net dipole moment of the supercell, effectively eliminating the surface error that arises from truncating the lattice summation. Implementation of this correction scheme is currently in progress within the Tew group.

3.12 Conclusions

We presented a domain-based PNO-MP2 local correlation theory formulated with BvK periodic boundary conditions. Localised Wannier functions are obtained via a straightforward Cholesky decomposition of the Γ-point one-particle density matrix. Analogously to the molec-

ular implementation, PNOs are generated through a PAO–OSV–PNO cascade, with periodic PAOs and OSVs serving as intermediates. The resulting Wannier orbitals, PAOs, OSVs, PNOs, and ERIs all preserve the translational invariance of the periodic system.

We also discussed challenges in applying local density fitting to periodic systems, particularly the slow convergence of lattice summations for long-range electrostatic interactions. Due to these limitations, the periodic PNO-MP2 method in this work is applied only to 1D and 2D systems (Chapter 4). We have adopted a chargeless local density fitting scheme to remove charge–charge interaction artefacts, and future developments will include surface-dipole corrections to mitigate convergence issues from dipole–dipole interactions.

4 | Calculations: Results and Discussion

In this chapter, the results of preliminary proof-of-concept periodic PNO-MP2 calculations for insulating systems are reported and analysed. Due to the preliminary nature of the implementation, timings for the calculations are not reported. These initial calculations were performed with the goal of ensuring proper functioning and testing the accuracy of the first implementation of the method in TURBOMOLE.

4.1 Cholesky Wannier Orbitals

Since localised Wannier orbitals serve as the basis for our periodic local MP2 implementation, it is essential to assess the effectiveness of the localisation scheme described in Section 3.6 before performing periodic PNO-MP2 calculations. To this end, we compare the values of a localisation metric based on the Pipek-Mezey (PM) scheme between both standard and Cholesky Wannier orbitals. Additionally, we visualise both types of orbitals: the standard Wannier orbitals, obtained through Fourier transformation of the Bloch orbitals obtained after SCF convergence, and the Cholesky-localised Wannier orbitals, derived using the proposed localisation approach.

The PM localisation metric (PM metric) is defined as the sum of squares of the partial charges, originally chosen as the Mulliken partial charges[108]. To generate localised Wannier functions, Jónsson *et al.* proposed a scheme where the PM metric $\langle O \rangle_{PM}$ is expressed in terms of the Mulliken charge $Q_i^{A_l}$ associated with a Wannier orbital $\tilde{i}$ centred on atom A in unit cell indexed by l[138]:

$$\langle O \rangle_{PM} = \sum_{l,A,i} \left| Q_i^{A_l} \right|^p = \sum_{l,A,i} \left\langle \tilde{i}_{\mathbf{0}} \middle| \hat{P}_{A_l} \middle| \tilde{i}_{\mathbf{0}} \right\rangle^p \tag{4.1}$$

Here, the operator $\hat{P}_{A_l}$, which projects onto the basis of supercell AOs centred on atom A_l is defined as

$$\hat{P}_{A_l} = \sum_{\mu \in A} \sum_{\nu} \sum_{l'} |\tilde{\mu}_l\rangle \, (S^{-1})^{\nu,l'}_{\mu,l} \, \langle \tilde{\nu}_{l'}| \tag{4.2}$$

where $S^{\nu,l'}_{\mu,l}$ is the overlap between supercell AOs $\tilde{\mu}_l$ and $\tilde{\nu}_{l'}$. However, Mulliken partial charges are known to be basis set dependent and are undefined for non-minimal basis sets, limiting their applicability. To overcome this issue, Zhu and Tew introduced a charge metric for Wan-

nier functions based on Intrinsic Atomic Orbitals (IAOs), which provides consistent charge definitions across different basis sets[139]. In this framework, Bloch IAOs are used to exactly represent the occupied Bloch orbitals. The PM projection operator in the Bloch IAO basis is then given as

$$\hat{P}^{IAO}_{A_l} = \sum_{\rho \in A} \sum_{\sigma} \sum_{l'} \left|\tilde{\rho}^{IAO}_{l}\right\rangle (S^{-1})^{\sigma,l'}_{\rho,l} \left\langle \tilde{\sigma}^{IAO}_{l'}\right| \tag{4.3}$$

where, $S^{\sigma,l'}_{\rho,l} = \left\langle \tilde{\rho}^{IAO}_{l} \middle| \tilde{\sigma}^{IAO}_{l'} \right\rangle$ is the overlap between real space IAOs $\tilde{\rho}_l$ and $\tilde{\sigma}'_l$. This overlap matrix is obtained by Fourier transforming the corresponding matrix in $\mathbf{k}$-space, denoted as $\mathbf{S}^{\mathbf{k}(IAO)}$.

Table 4.1 presents the IAO-based PM metric values computed for the SCF-converged Wannier orbitals and the Cholesky-localised Wannier orbitals of *Polyethylene*, a 1D polymer, and a 3D rhombohedral lattice of *Silicon*. The values of the PM metric, $\langle O \rangle_{PM}$ (SCF), obtained directly from Wannierization of SCF-converged Bloch orbitals, are notably small. Moreover, these values can fluctuate arbitrarily between separate runs of the same calculation due to variations in the gauge of Bloch functions. However, $\langle O \rangle_{PM}$ (SCF) values never exceed, and are consistently much smaller than, the corresponding $\langle O \rangle_{PM}$ (Cholesky) values obtained from Cholesky-localised Wannier orbitals.

Applying the Cholesky localisation scheme significantly increases the PM metric in all cases, indicating improved orbital localisation. The Wannier orbitals for both systems are depicted in Figures 4.1 to 4.4. A comparison of the Wannier orbitals before and after localisation demonstrates that the Cholesky localisation method effectively localises the Wannier orbitals in these non-metallic systems.

System	$\langle O \rangle_{PM}$ SCF	$\langle O \rangle_{PM}$ Cholesky
Polyethylene	6.78×10^{-4}	0.41
Silicon	5.09×10^{-2}	9.73

Table 4.1: PM metric for unoptimised and Cholesky localised Wannier orbitals of Polyethylene and Silicon

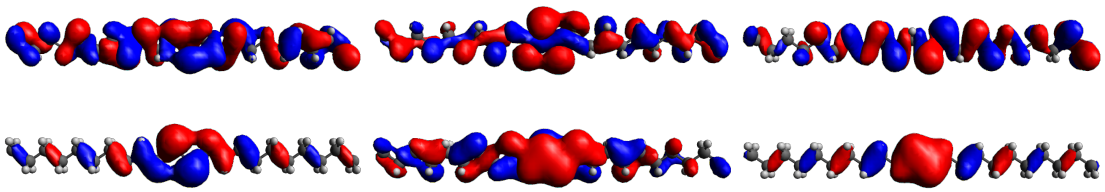


Figure 4.1: SCF-converged Wannier orbitals for an 11-unit polyethylene chain, plotted with an isosurface value of 0.01.

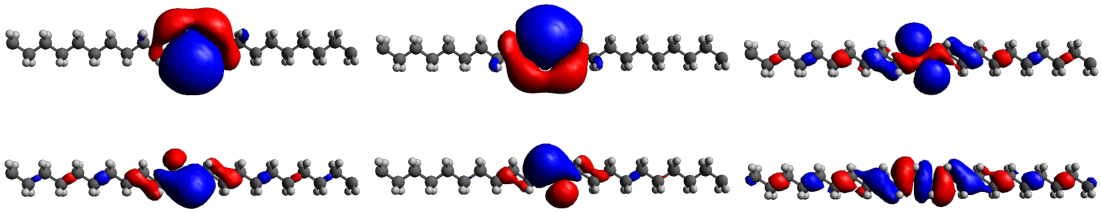


Figure 4.2: Cholesky-localised Wannier orbitals for an 11-unit polyethylene chain, plotted with an isosurface value of 0.01.

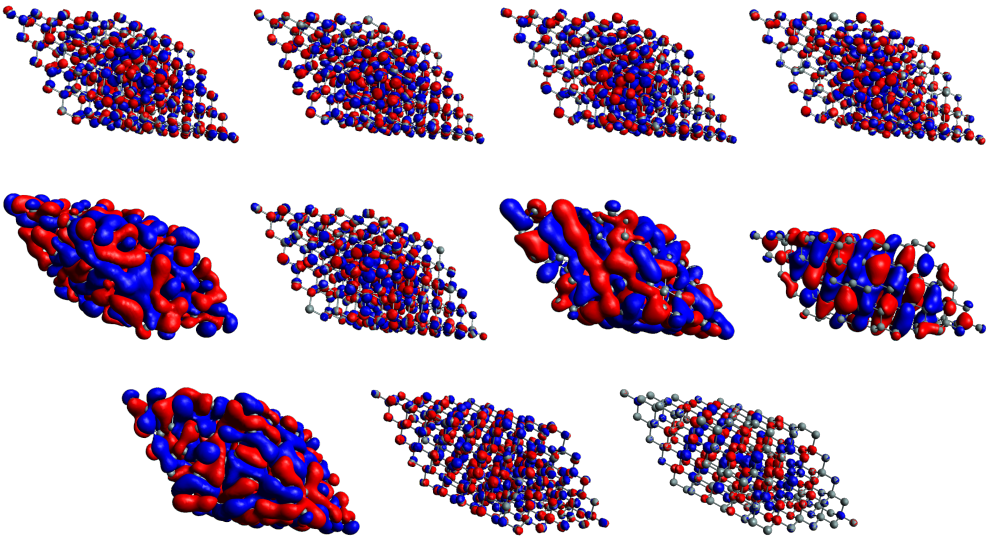


Figure 4.3: SCF-converged Wannier orbitals for a $5 \times 5 \times 5$ silicon lattice, plotted with an isosurface value of 0.001.

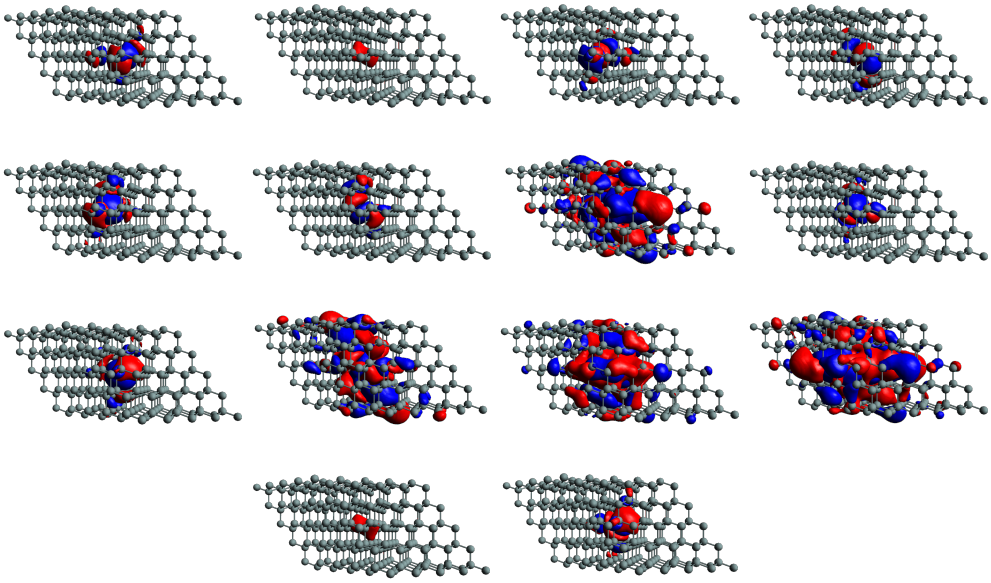


Figure 4.4: Cholesky-localised Wannier orbitals for a $5 \times 5 \times 5$ silicon lattice, plotted with an isosurface value of 0.001.

4.2 Correlation Energy Per Cell: Periodic vs Molecular

This section aims to validate the correctness of our initial periodic PNO-MP2 implementation by benchmarking it against molecular calculations using an embedding approach. To examine this, we compare the energy per unit cell obtained from periodic PNO-MP2 calculations with that extracted from a large, finite molecular crystal. To extract the energy per cell of bulk material from molecular calculations, we evaluate the energy of the central unit cell within an extended molecular system. As the molecular system grows in size, the environment surrounding the central unit cell increasingly resembles the periodic bulk, and its energy converges to the true periodic limit–corresponding to the energy per cell from a periodic calculation with well-converged **k**-point sampling. To mitigate edge effects inherent to finite systems, we employ simple formulae based on the decomposition of the total energies into contributions from the centre, edges, and corners. We apply this benchmarking procedure to the 1D polymer, *Polyethylene*, and 2D *Xe* and *CO* lattices.

1. *Polyethylene*: Calculations for this 1D polymer were conducted using def-SVP and pob-TZVP basis sets. The periodic calculations were conducted using an odd number of **k**-points ranging from 7 to 27 and 11 to 27 for pob-TZVP and def-SVP basis sets, respectively. Similarly, molecular calculations were performed for polymer chains with

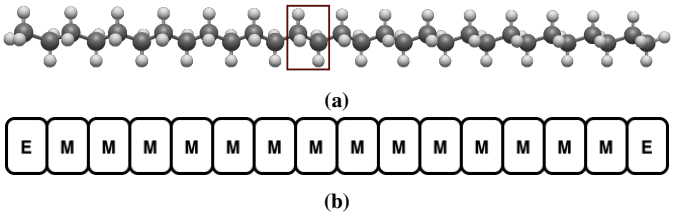


Figure 4.5: (a)Illustration of a polyethylene molecule with a total length equivalent to 15 repeating units of the monomer, ethylene (C_2H_2). The red box indicates the unit cell employed in periodic calculations or the monomer unit employed in molecular calculations. (b) Decomposition of a finite 1D molecular chain into middle (M) and edge (E) cells.

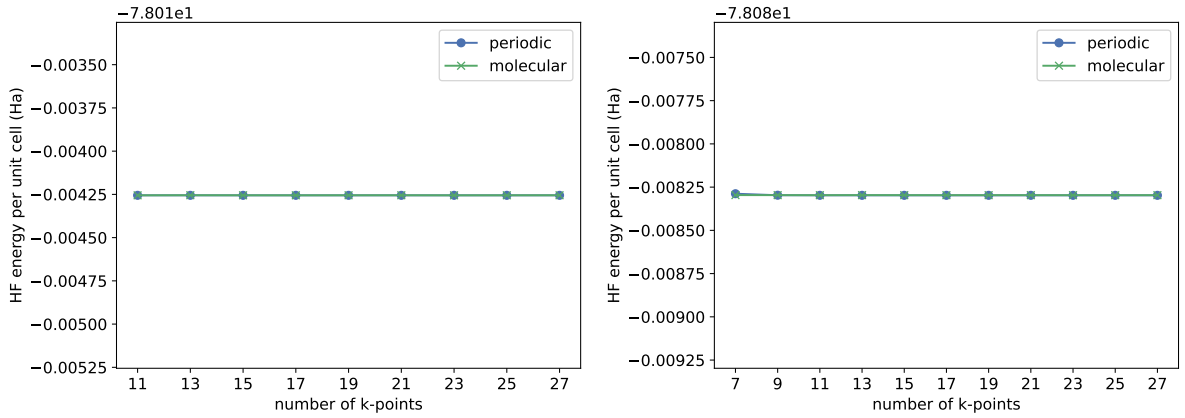
lengths ranging from 7 to 27 and 11 to 27 repeating monomer units, respectively, for pob-TZVP and def-SVP basis sets, with hydrogen atoms adjusted at both ends of the chain for proper termination. One such polymer chain is illustrated in Figure 4.5, with the monomer unit and the unit cell highlighted by a box. Periodic calculations were carried out using this unit cell, which has a length of 2.53Å in the periodic direction. All PNO-MP2 calculations were performed for PNO thresholds ranging from 10^{-5} (loose) to 10^{-9} (tight) in increments of 0.1. To extract the correlation energy per unit cell from molecular calculations, we employ a simple decomposition scheme as illustrated in Figure 4.5b. This scheme aims to mitigate the edge effects, so the total correlation energy E_n is partitioned into contributions from the two chain ends (edges) and the bulk (middle) region as follows:

$$E_n = 2E_e + (n-2)E_m \implies E_m = \frac{E_{n+2} - E_n}{2} \tag{4.4}$$

where E_e and E_m denote the correlation energy contributions from the edge and middle (bulk) units, respectively. Since our periodic calculations are performed using successively odd numbers of **k**-points, this decomposition allows us to approximate the bulk energy per unit cell, E_m, as the slope of a linear fit to the total correlation energies of two extended polymers differing by two monomer units.

As shown in Figure 4.6, the correlation energies per cell obtained from periodic calculations are effectively identical to those obtained from molecular HF calculations, and the values are already converged at the smallest **k**-point sampling, showing negligible changes in subsequent calculations.

To assess the accuracy of our molecular calculations, we compare the correlation energies



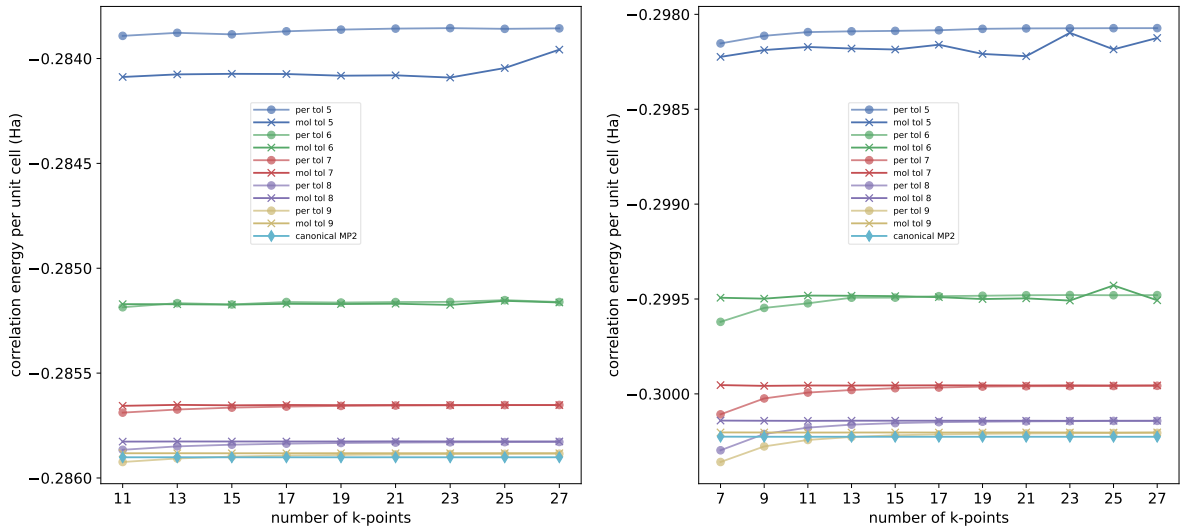
(a) def-SVP **(b)** pob-TZVP

Figure 4.6: Comparison of HF energy per unit cell (in Ha) between periodic and molecular results of Polyethylene, plotted as a function of the number of **k**-points for (a) def-SVP and (b) pob-TZVP basis sets

per unit obtained from PNO-MP2 calculations against those obtained from the canonical MP2 calculations for all extended molecules of polyethylene. The canonical MP2 calculations were carried out using the `ricc2` module of TURBOMOLE. Energies are plotted as a function of the number of **k**-points or unit cells in Figure 4.7. The canonical MP2 correlation energy per cell remains essentially constant across polymer chains of increasing length. For both basis sets, as expected, tighter PNO thresholds of 10^{-7}, 10^{-8}, and 10^{-9} yield energies that are in excellent agreement with canonical MP2 results.

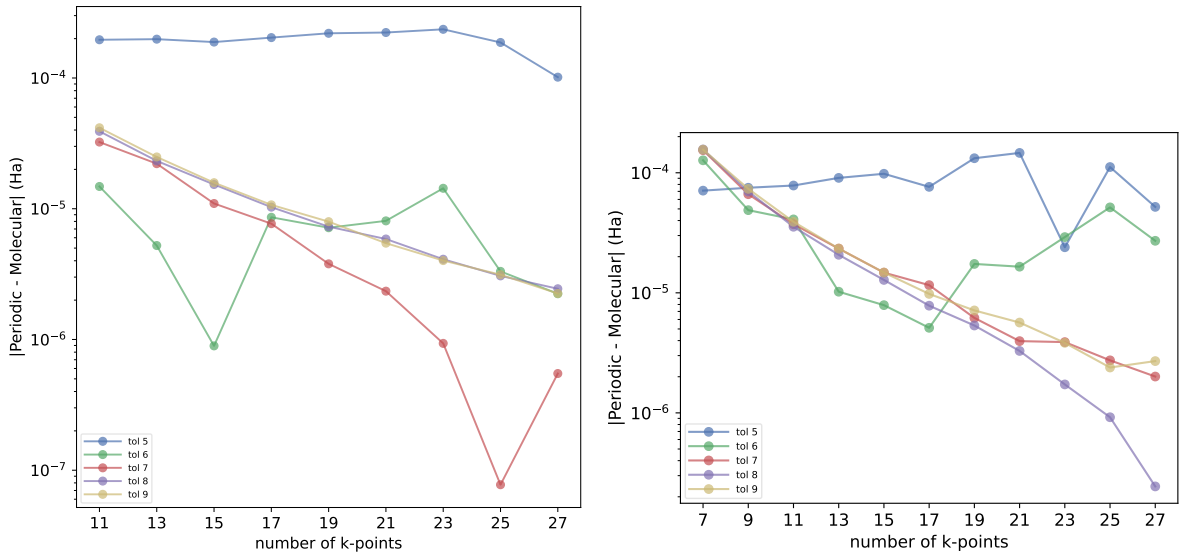
Overall, the molecular and periodic approaches show excellent agreement. As illustrated in Figure 4.8, the absolute deviation in correlation energy per cell between the periodic and molecular methods is on the order of 10^{-5} Ha or smaller when using at least 17 **k**-points. This deviation systematically decreases with increasing the number of **k**-points for tighter PNO thresholds of 10^{-7} to 10^{-9}. In contrast, looser thresholds show larger differences due to the increased truncation of PNO domains. Since the domain approximation differs between periodic and molecular implementations, small discrepancies are expected. Nevertheless, the results confirm that the periodic implementation is functioning properly for 1D systems and reproduces the expected PNO truncation behaviour.

2. *Xe and CO surfaces*: To test the implementation on 2D systems, we performed calculations for Xe and CO lattices. A Xe surface was cut out from a 3D simple cubic crystal structure, such that the 2D Xe lattice has a unit cell length of 4.2Å in the two orthogonal, periodic directions. Xe being a heavy element, we used an effective-core potential for the



(a) def-SVP **(b)** pob-TZVP

Figure 4.7: Comparison of PNO-MP2 correlation energy per unit cell (in Ha) from periodic (per) and molecular (mol) calculations against canonical MP2 results of Polyethylene, plotted as a function of the number of **k**-points for (a) def-SVP and (b) pob-TZVP basis sets and PNO thresholds in the range of 10^{-5} and 10^{-9} which are indicated in the legend as 'tol 5', 'tol 6', and so on.



(a) def-SVP **(b)** pob-TZVP

Figure 4.8: Absolute deviation in PNO-MP2 correlation energy per unit cell (Ha) between periodic and molecular calculations of Polyethylene, plotted as a function of the number of **k**-points for (a) def-SVP and (b) pob-TZVP basis sets and PNO thresholds in the range of 10^{-5} and 10^{-9} which are indicated in the legend as 'tol 5', 'tol 6', and so on.

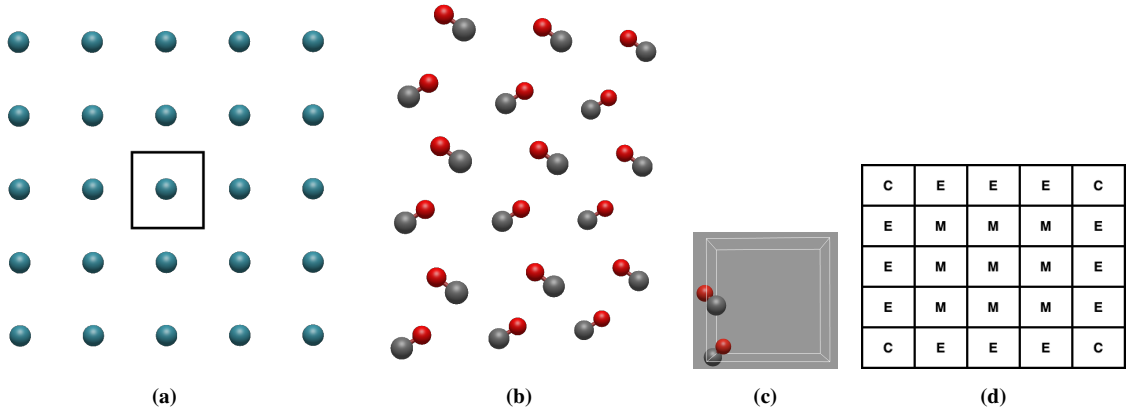


Figure 4.9: (a) Xe 5×5 lattice with unit cell highlighted by a square. (b) CO lattice of dimension 3×3 with its unit cell shown in (c). (d) Decomposition of a finite 2D periodic system into corners (C), edges (E) and middle (M) cells.

$1s2s2p3s3p3d$ electrons and the basis set def-SVP, to describe the remaining orbitals, of which $4s4p$ remained frozen, and only $4d5s5p$ were treated explicitly at post-HF level. The HF procedure for Xe employed the universal Coulomb fitting auxiliary basis sets [140], while the PNO-MP2 calculations utilised the auxiliary basis sets optimised for the def-SVP atomic orbital basis set. Similarly, a 2D lattice of CO was cut out from a 3D face-centred cubic molecular crystal of CO where the C-O bond length is 1.14 Å. The unit cell length is 5.96 Å in the two orthogonal, periodic directions. The calculations for CO were carried out using the pob-TZVP basis set designed for solid-state calculations in Gaussian basis [141,142]. Similar to Xe, the universal Coulomb fitting auxiliary basis sets [140] were used for HF calculations of CO, and the auxiliary basis sets optimised for the def2-TZVP orbital basis sets were employed for PNO-MP2.

We perform periodic calculations using Monkhorst-Pack **k**-point meshes of various sizes and calculations for the corresponding molecular systems. In Table 4.2 and Table 4.3 for Xe and CO, respectively, the periodic PNO-MP2 correlation energies per unit cell, as well as the correlation energies per cell from molecular calculations, are reported for the PNO thresholds of 10^{-7} and 10^{-8}. To minimise edge effects from molecular calculations, we employed a very simple scheme of decomposing a finite, 2D square periodic lattice into corners, edges and middle cells as demonstrated for a 5×5 lattice in Figure 4.9d. The total correlation energy E_n of a system of size corresponding to n unit cells can then be decomposed as the sum of contributions from the corners E_c, edges E_m and the middle

E_m as

$$E_n = 4E_c + 4(n-2)E_e + (n-2)^2 E_m \tag{4.5}$$

The three variables $E_c, E_e,$ and E_m are easily determined using a set of three equations corresponding to different values of n. The quantity E_m can then be interpreted as the correlation per molecular unit. This helps minimise the finite size effects in our molecular calculations and allows for a direct comparison of E_m with the correlation energy per cell obtained from periodic calculations. The correlation energies per molecular unit obtained using this approach are reported in Table 4.2 and Table 4.3 as tuples representing the different values of n employed. For example, the tuple $(3, 5, 7)$ corresponds to E_m derived from calculations using the 3×3, 5×5 and 7×7 lattices.

The agreement between periodic and molecular calculations is excellent. For instance, the molecular and periodic correlation energy per cell for Xe differ by only about 2.8 mHa for the smallest 3×3 lattice. The difference decreases further with increasing lattice size, reaching just 0.7 mHa for the largest 9×9 lattice. After applying the scheme outlined above to minimise the edge effects, the discrepancy between molecular and periodic calculations is further reduced to approximately 0.1 mHa or lower. Since periodic calculations are expected to converge with increasing lattice size, we compare the energy obtained from $(3, 5, 7)$ and $(5, 7, 9)$ with the correlation energy per cell obtained from the largest periodic calculation corresponding to the 9×9 lattice for Xe. The agreement between molecular and periodic calculations is even better in the case of CO, perhaps due to using a larger basis set of triple-ζ quality. The difference is already as small as 0.1 mHa or lower for the 3×3 lattice of CO. The effect of the approach to minimise the edge effects is negligible in the case of CO, as the difference is already reduced to the order of 10^{-5} Ha for larger lattice sizes of 5×5 and 7×7. These results confirm that the periodic PNO-MP2 implementation performs reliably for both 1D and 2D systems.

4.3 Rolling Energy of BN Nanoscroll

In this section, we examine a 1D periodic insulator–BN nanoscroll, a spirally wrapped tubular structure resembling a multiwalled carbon nanotube. A nanoscroll represents an intermediate stage in the transformation of nanosheets into nanotubes. As a result, nanoscrolls are expected

Xe lattice size	10^{-7} molecular	10^{-7} periodic	10^{-8} molecular	10^{-8} periodic
3×3	-0.527996	-0.530753	-0.528073	-0.530879
5×5	-0.528660	-0.530048	-0.528759	-0.530142
7×7	-0.528953	-0.529865	-0.529060	-0.530002
9×9	-0.529158	-0.529881	-0.529235	-0.529969
$(3,5,7)$	-0.529709		-0.529831	
$(5,7,9)$	-0.530113		-0.529892	

Table 4.2: Molecular and periodic PNO-MP2 correlation energies per repeating unit calculated for PNO thresholds 10^{-7} and 10^{-8} for the 2D Xe lattice, along with correlation energy per repeating unit obtained after $(3,5,7)$ and $(5,7,9)$ decompositions for molecular calculations. All energies are in the units of Ha.

CO lattice size	10^{-7} molecular	10^{-7} periodic	10^{-8} molecular	10^{-8} periodic
3×3	-0.533419	-0.533529	-0.533523	-0.533622
5×5	-0.533464	-0.533494	-0.533570	-0.533586
7×7	-0.533479	-0.533487	-0.533585	-0.533578
$(3,5,7)$	-0.533506		-0.533613	

Table 4.3: Molecular and periodic PNO-MP2 correlation energies per repeating unit calculated for PNO thresholds 10^{-7} and 10^{-8} for the 2D CO lattice, along with correlation energy per repeating unit obtained after $(3,5,7)$ decomposition for molecular calculations. All energies are in the units of Ha.

to exhibit unique properties that blend characteristics of both nanosheets and nanotubes.

In this study, both the BN nanoscroll and the nanosheet feature a honeycomb arrangement of B and N atoms, with the sheet's edges saturated by hydrogen atoms. Figure 4.10 provides the illustrations of the nanoscroll and nanosheet, along with their respective unit cells used in periodic calculations. Each unit cell consists of 122 atoms (59 B, 59 N, and 4 H atoms). This system was previously studied by Pisani *et al.*[79], using a periodic local MP2 implementation in CRYSCOR, albeit for a different geometry corresponding to a different, slightly higher degree of rolling.

To assess the effectiveness of our periodic PNO-MP2 implementation, we compute the rolling energy of the BN nanoscroll relative to its unrolled BN nanosheet. As described in Ref. 79, the rolling energy consists of two competing contributions: a repulsive term arising from the deformation energy required to roll the nanosheet and an attractive term due to van der Waals interactions between adjacent regions of the scroll. Our objective is to determine whether the rolling is energetically favourable. To this end, we investigate the favorability of rolling at three

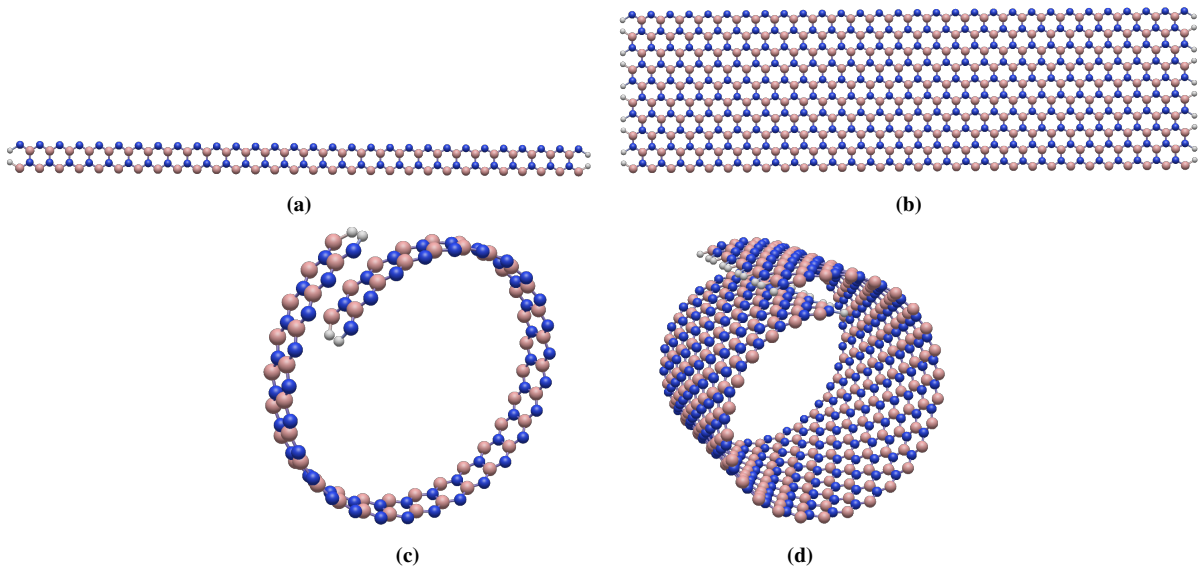


Figure 4.10: Illustrations of BN nanosheet and nanoscroll: (a) nanosheet unit cell (b) nanosheet consisting of 5 unit cells (c) nanoscroll unit cell (d) nanoscroll consisting of 5 unit cells

levels of theory: DFT, HF and HF+PNO-MP2. The relative performance of various methods can be properly examined by comparing between the methods, the error in rolling energy as a function of the degree of rolling. However, a higher degree of rolling leads to a greater number of interactions between regions that come into proximity with each other, rendering the calculation more expensive. Therefore, this work is limited to calculations with only a single, fixed degree of rolling. Moreover, highly accurate results for the rolling energies of the BN nanoscroll are not yet available; hence, it is not possible to calculate errors in rolling energy for various methods. So, we note that our results are not conclusive. The periodic local-MP2 calculations carried out by Pisani *et al.*[79] at a slightly higher degree of rolling than that considered here suggest that the rolling of the nanosheet is energetically favourable. The rolling energy E_{roll} per BN unit is evaluated as

$$E_{roll} = \frac{E_{scroll} - E_{sheet}}{59} \tag{4.6}$$

where E_{scroll} and E_{sheet} are the energies per unit cell of the nanoscroll and the nanosheet, respectively. Thus, the rolling energy must be negative for rolling to be energetically favourable.

The calculations were carried out for two different atomic orbital basis sets: def-SVP and pob-DZVP. For def-SVP, we used the corresponding Coulomb and exchange fitting basis sets for the HF calculations, as well as the corresponding auxiliary bases for the density fitting procedure

in the PNO-MP2 calculations. For pob-DZVP, universal bases were used for the Coulomb and exchange fitting at the HF level, while auxiliary bases optimised for def-SVP were utilised for density fitting in PNO-MP2 calculations. Electrons from the core 1s orbitals of B and N atoms were kept frozen in the PNO-MP2 correlation calculations. The PNO-MP2 calculations used equal thresholds to truncate the OSV and the PNO basis. For our DFT calculations, we employed the B3LYP functional[143,144], and applied the D2 correction[145] to account for dispersion interactions. The calculations were carried out for 5 and 7 **k**-points in the periodic direction. The rolling energy per BN unit of all calculations is reported in Table 4.4.

We observe that for the fixed degree of rolling considered here, even with the inclusion of dispersion corrections, the DFT calculations with the B3LYP functional and D2 dispersion correction predict rolling to be unfavourable. Although the rolling energy obtained from the HF calculations is slightly lower than that from DFT, HF also does not favour the rolling of the nanosheet. However, the rolling energy decreases by approximately 1 kJ/mol per BN unit when the basis set is changed from def-SVP to pob-DZVP. As an additional result, these calculations highlight the advantage of basis sets specifically designed for periodic calculations. Although both def-SVP and pob-DZVP are of double-ζ quality and thus comparable in size, the latter is optimised for solid-state calculations. The advantage is evident from the missing HF result for def-SVP with the smaller **k**-point mesh of 5, which is due to convergence issues arising from linear dependency in SCF calculations. Such issues are commonly encountered when molecular basis sets, such as def-SVP, are employed in periodic calculations.

The last two columns of Table 4.4 report the HF+PNO-MP2 rolling energies obtained for two different PNO thresholds. A periodic PNO-MP2 calculation with a **k**-point sampling size of 5, using the pob-DZVP basis and a loose PNO occupation threshold of 10^{-6}, reduces the rolling energy per BN unit by two orders of magnitude, but still predicts the rolling to be unfavourable. However, when a tighter PNO threshold of 10^{-7} is used, the rolling energy per BN unit shifts to -0.1 kJ/mol, making the nanoscroll energetically more stable than the nanosheet and thus rendering the rolling favourable.

For the pob-DZVP basis, the rolling energy decreases further to -1.4 kJ/mol per BN unit for a larger sample size of 7 **k**-points, even with the loose PNO threshold of 10^{-6}. Although calculations using the tighter threshold of 10^{-7} were not feasible for 7 **k**-points due to compu-

tational limitations, the trend suggests that the rolling energy would decrease even further with a tighter threshold. Notably, for the def-SVP basis set, the rolling energy remains positive at the HF+PNO-MP2 level. However, it decreases from 1.4 kJ/mol per BN unit to 0.9 kJ/mol per BN unit when the PNO threshold is tightened, indicating that further tightening may reverse the stability order, favouring the formation of the nanoscroll.

These results suggest that MP2 effectively captures dispersion interactions between adjacent sides of the nanoscroll, favouring the rolling of the nanosheet. Since the PNO-MP2 calculations did not employ very tight PNO thresholds, the computed rolling energies are likely not fully converged. Furthermore, the decrease in rolling energy observed for the pob-DZVP basis when increasing the **k**-point sampling from 5 to 7 suggests that the rolling energy may not be fully converged with respect to the number of **k**-points. Therefore, an accurate prediction of the rolling energy would require both larger **k**-point sampling and tighter PNO thresholds. Furthermore, as mentioned before, for a more thorough analysis, calculating the rolling energy at different levels of rolling remains important.

Degree of Rolling:

No. of cells or **k**-points	Basis	DFT	HF	PNO-MP2 10^{-6}	PNO-MP2 10^{-7}
5	def-SVP	2.9	unconverged	-	-
	pob-DZVP	1.8	1.7	0.02	-0.1
7	def-SVP	2.9	2.6	1.4	0.9
	pob-DZVP	1.8	1.7	-1.4	not feasible

Table 4.4: Rolling energy per BN unit in kJ/mol computed at DFT, HF and HF+PNO-MP2 level for two PNO thresholds, 10^{-6} and 10^{-7}. PNO-MP2 calculations for the *k*-point mesh of 5 were not possible for the def-SVP basis as the HF calculation remained unconverged (indicated by '-').

4.4 Notes on Implementation

This work presents a preliminary implementation of periodic PNO-MP2 in TURBOMOLE. A key component of this development is a newly implemented subroutine for constructing localised Wannier orbitals, which define the localised occupied space. To this end, the scheme described in Section 3.6 has been implemented. The first step involves localising the Γ-point Bloch orbitals using Cholesky decomposition–a relatively simple initial approximation. This

step may be further refined by replacing the Cholesky approach with a localisation functional. Although not covered in this thesis, Zhu and Tew[139] have since extended this approach by applying the Pipek–Mezey localisation functional, using the Cholesky-localised orbitals as an initial guess.

There are two complementary strategies for a periodic treatment of a crystal:

1. **BvK supercell approach:** This approach employs the periodic boundary conditions applied to a finite-sized simulation cell, which we call a supercell. The integrals are evaluated using lattice summation, and due to the imposed translational symmetry, only a limited number of electron pair interactions need to be considered. **Both the theoretical framework developed in this thesis and the calculations presented are based on the supercell approach**.

2. **Megacell approach:** Here, a large yet finite simulation cell, which we call a *megacell* is constructed, and translational symmetry is applied to the various entities (e.g., orbitals). The infinite crystal is approximated by summing pair energies over a sufficiently large range. This can be seen as a Γ-point calculation on a large supercell. Unlike the supercell approach, this method, in principle, involves an infinite number of pair contributions, as the lattice summation is carried out through explicit pairwise evaluation. This approach serves as an alternative to the supercell approach and is also being actively pursued within the Tew group.

When the lattice summation of integrals is performed efficiently, the supercell approach is generally computationally more favourable for periodic systems. However, the megacell approach becomes particularly advantageous in the study of localised phenomena, such as defects. In the BvK supercell framework, modelling a defect requires a large simulation cell to suppress spurious interactions between periodic images of the defect. In contrast, the megacell approach treats the defect as a truly local perturbation, naturally avoiding artificial periodic repetition and thereby enabling more realistic modelling of isolated defects.

Although the method for localising Wannier orbitals is functional and applicable to 3D periodic systems, the more efficient of the two periodic strategies–the supercell approach for periodic PNO-MP2–is currently limited to 1D and 2D systems. This restriction arises from convergence issues in the lattice summation of density-fitted integrals, as discussed in Section 3.11. Once

the dipole correction scheme is incorporated into the periodic local density fitting framework, 3D calculations are expected to become feasible. In contrast, the megacell approach, which performs pair energy summation over an extensive spatial range, does not suffer from the lattice summation problem. However, its primary challenge lies in reaching sufficiently large megacells to achieve convergence.

To further improve the efficiency of the evaluation of MP2 integrals in the supercell approach, we plan to adapt the periodic continuous fast multipole method (CFMM)[137,146] that is already in use in the periodic HF module in TURBOMOLE[120]. In CFMM, the Coulomb integrals are partitioned into near-field and far-field terms. The near-field terms, which are computationally dominant, are evaluated using direct integration via DF, and far-field terms are computed using multipole expansions with a dipole correction scheme when necessary, as described in Section 3.11.

Integral evaluation in the megacell approach may benefit from a multipole approximation for "distant" Wannier orbital pairs. Distant pairs are characterised by mutually non-overlapping orbital product densities, $\left\langle \rho_{ia_{l+L}} \middle| \rho_{j_{m+M}b_{n+N}} \right\rangle \approx 0$, where the spatial separation between the densities precludes significant overlap. The multipole expansion technique has been successfully employed in local treatments of molecular systems to achieve reduced or asymptotically linear scaling for the evaluation of Coulomb integrals[52,147]. This method has also been extended to periodic systems by Usvyat *et al.*[81], who highlight that careful consideration is required in defining the criterion for identifying distant pairs.

A key factor in achieving an efficient periodic implementation is the effective exploitation of translational invariance. Although the version of the code used for the calculations presented in this thesis did not fully leverage translational symmetry across all components, subsequent optimisations have addressed this limitation. Incorporating translational symmetry results in substantial performance gains, particularly enhancing the efficiency of the megacell approach. These improvements make 3D periodic PNO-MP2 calculations via the megacell strategy significantly more feasible.

4.5 Conclusions

In this work, we have introduced the periodic PNO-MP2 method, where PNOs represent pair-specific virtual spaces under BvK boundary conditions. The PNOs are obtained as eigenvectors of the doubles amplitude density matrices associated with Wannier orbital pairs.

We have also presented a novel scheme for constructing localised Wannier orbitals by localising the Γ-point Bloch orbitals using a straightforward Cholesky decomposition. The locality of the Γ-point is then enforced onto the Bloch orbitals at other **k**-points. Since Γ-point Bloch orbitals are real, this approach minimises phase variations in the remaining Bloch orbitals, ensuring smooth **k**-dependence and yielding well-localised Wannier orbitals upon Fourier transformation. This procedure was tested on a 1D polyethylene chain and a 3D silicon crystal. To assess localisation quality, we used a Pipek-Mezey (PM) metric based on intrinsic atomic orbitals (IAOs)[139]. For both systems, comparing the PM metric before and after localisation suggests that our approach is highly effective, and this result was further supported by visualisation of the Wannier orbitals.

Proof-of-principle calculations have been performed to demonstrate the capabilities of our periodic PNO-MP2 implementation. We tested the reliability of our implementation on 1D polyethylene chain, 2D CO, and Xe lattices. The correlation energy per unit cell obtained in these periodic calculations closely matches that of the molecular PNO-MP2 calculations. Notably, the results for the 2D CO and Xe lattices are particularly encouraging as the calculations were performed with relatively small **k**-point meshes. This agreement is expected to improve with finer meshes.

We applied our PNO-MP2 method to calculate the rolling energy of a BN nanoscroll. Using small **k**-point meshes of 5 and 7 and intermediate PNO thresholds of 10^{-6} and 10^{-7}, our PNO-MP2 calculations inverted the nanoscroll stability predicted by HF and DFT methods. This is an encouraging result, as it qualitatively aligns with the result obtained in 79, albeit at a different rolling radius, and is expected to become quantitatively more accurate with tighter PNO thresholds. Furthermore, since dispersion interactions are crucial in the case of BN nanoscroll, our results highlight the ability of PNO-MP2 to effectively capture such interactions.

Finally, we comment on the expected scaling behaviour of the periodic PNO-MP2 method, as

part of our implementation strategy based on the supercell approach. The overall scaling is determined by the most computationally demanding step, which–when translational symmetry is exploited–is the evaluation of three-centre integrals using DF. This step must be performed for every Wannier orbital in the reference unit cell and scales as $\mathcal{O}(N)$, where N is the number of Wannier orbitals in the unit cell. However, this step involves explicit lattice summations over supercells L, which can introduce a significant prefactor. Additionally, the size of DF domains–i.e., the regions over which each Wannier orbital interacts–may also introduce a large prefactor, particularly in small supercells where domains may extend across the entire supercell. As a result, the method may not exhibit linear scaling until the supercell is sufficiently large for the DF domains to remain spatially localised within the supercell. We therefore anticipate a transition from cubic to quadratic and eventually linear scaling as the supercell size increases.

The subsequent construction of PNOs and computation of pair energies primarily depend on the number of unique Wannier orbital pairs. Due to the translational symmetry of Wannier orbitals, the number of unique pairs $\{i_0 j_l\}$ grows linearly with N, since each reference orbital i_0 interacts with an asymptotically constant number of j_l. The remaining steps, including solving the residual equations in the PNO basis and computing the PNO-MP2 energy, also scale linearly with N.

These considerations suggest that the periodic PNO-MP2 method should exhibit asymptotic $\mathcal{O}(N)$ scaling, with the transition to linear scaling dependent on the size of the supercell relative to the extent of the DF domains.

5 | Extrapolation Schemes in PNO Methods

As highlighted previously, the cost of wavefunction methods depends on the size of the system as well as the size of the one-electron basis set. The steep scaling of these methods with respect to system size can be alleviated, at least in insulating systems, using local correlation approaches such as PNO methods. However, these methods also suffer from slow convergence of the correlation energy with the size of the AO basis. Typically, wavefunction methods scale as $O(M^4)$ with respect to the number of functions M in the atomic basis set, and the correlation energy converges only as M^{-1}. This slow convergence is caused by the cusp in the electronic wavefunction. The cusp arises as two electrons i and j approach each other, $r_{ij} \to 0$. It is extremely difficult to capture the cusp simply by using the antisymmetrised product of molecular orbitals. Therefore, very large atomic basis sets are required for the convergence of correlation energy, rendering high-accuracy calculations very expensive. The local correlation approaches cannot alleviate the steep scaling with the size of the atomic basis set. This problem can be addressed by using either explicitly correlated methods that regularise the Hamiltonian and accelerate convergence with respect to the basis set size or by using basis set extrapolation schemes to approach the basis set limit. In this chapter, we investigate extrapolation schemes in the context of PNOs at MP2, and CCSD(T) levels of theory. In doing so, we study the relationship between PNO truncation error and convergence of correlation energy towards the complete PNO space (CPS) or the canonical limit for a given basis set, as well as towards the complete basis set (CBS) limit. The work presented in this chapter has been published in two parts, in Ref. 1 and Ref. 2.

Truncating the PNO basis is equivalent to using a smaller set of AOs for each pair of occupied MOs. Thus, PNO truncation introduces a basis set incompleteness error in addition to the error due to the finite size of the AO basis set. Due to the combination of the two errors, employing standard basis set extrapolation techniques in PNO methods requires careful assessment. In the following sections, we present various extrapolation schemes for PNO-based methods to estimate both the canonical energy for a given basis set and the complete basis set limit. Subsequently, we analyse and discuss the results of benchmarking these extrapolation approaches.

5.1 Extrapolation of PNO-MP2 Energies

5.1.1 Extrapolation to the Canonical Limit

As described in Section 2.11.2, PNOs form a set of virtual orbitals for each pair ij of occupied MOs, and the size of the PNO basis can be tuned using the occupation number threshold T. The selected virtuals are the PNOs for a given pair with occupation numbers larger than T. Since the size of the PNO basis is typically small, and the number of retained PNOs is independent of the system size, the scaling and overall cost of the method are dramatically reduced. The error introduced by truncating the PNO basis can be computed as the difference between the energy calculated using the truncated PNO basis and the full canonical result. Figure 5.1 illustrates how the PNO truncation error behaves as a function of the PNO threshold T. The data for this plot were extracted from Ref. 148. We observe that the energy $E(T, X)$ as a function of T follows a power law

$$E(T, X) \approx E(X) + CT^{\alpha} \tag{5.1}$$

where $E(X)$ is the canonical result for a basis set characterised by the cardinal number X, and the constant of proportionality C and the exponent α are system and basis-set-dependent. The power law is described by three parameters C, α and $E(X)$. Therefore, to approach the canonical limit $E(X)$ of the basis set, the following formula can be deduced, which utilises the correlation energies $E(T_1, X)$, $E(T_2, X)$ and $E(T_3, X)$ calculated at three consecutive PNO thresholds T_1, T_2 and T_3, respectively.

$$E(X) = \frac{E(T_1, X)E(T_3, X) - E^2(T_2, X)}{E(T_1, X) + E(T_3, X) - 2E(T_2, X)} \tag{5.2}$$

We refer to this as the three-point **occupation number extrapolation** to the canonical limit.

5.1.2 Extrapolation to the Basis Set Limit

Instead of the canonical limit, we can also examine the error relative to the basis set limit as a function of the size of the PNO basis. Tew *et al.* showed that for a given basis set, the correlation energy converges as N^{-1} towards the basis set limit before saturating at the canonical limit[148].

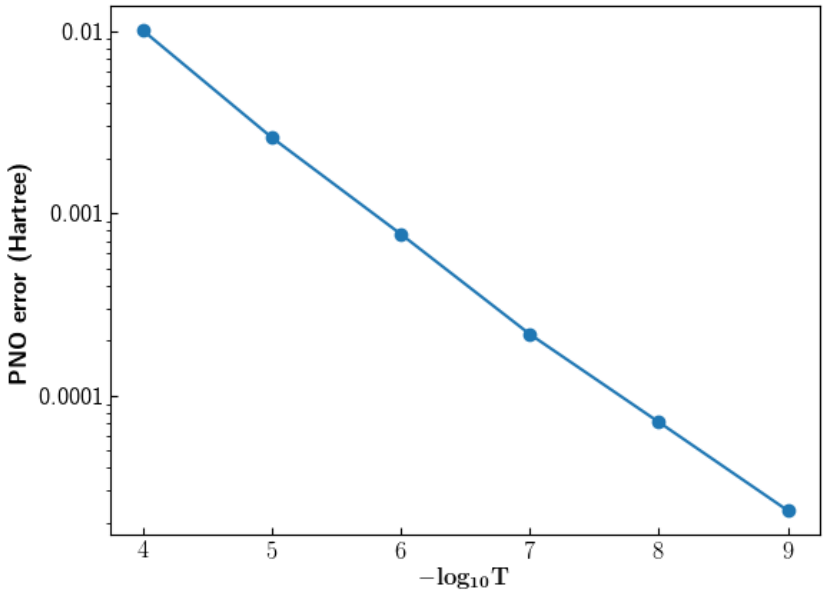


Figure 5.1: PNO truncation error for the MP2 correlation energy of formic acid using the cc-pVDZ-F12 basis, as a function of PNO threshold T. The data for this plot was extracted from previous work, which involved a test set of 105 reactions generated from a set of 106 molecules compiled by Bakowies.

This behaviour is illustrated in Figure 5.2 generated using data from Ref. 148 for three different basis sets. The size of the PNO basis increases from left to right in Figure 5.2a and from right to left in Figure 5.2b. Therefore, the rightmost points in Figure 5.2a and the leftmost points in Figure 5.2b represent the least or no truncation of the PNO basis, corresponding to the canonical correlation energies for the respective basis sets. Conversely, the y-intercept in Figure 5.2a and the right asymptote in Figure 5.2b represent the largest truncation of the PNO basis, which corresponds to minimal or no correlation energy. As we increase the size of the PNO basis by including functions with the next largest occupation numbers, the error in correlation energy with respect to the basis set limit decays as N^{-1} as depicted by the dotted line in Figure 5.2b. Including functions with insignificantly small occupation numbers has a negligible effect on the energy, which is evident from the plateau regions of the plots. The observed N^{-1} decay of correlation energy could be exploited to extrapolate to the basis set limit. Since the total correlation energy is given by the sum of pair correlation energies, the basis set error in the correlation energy $E^{ij}(N_{ij})$ for a given pair ij exhibits the same decay behaviour with respect to the size of the PNO basis N_{ij} for the pair. This behaviour can be expressed as

$$E^{ij}(N_{ij}) \approx E^{ij}_{\infty} + C_{ij}N^{-1}_{ij} \tag{5.3}$$

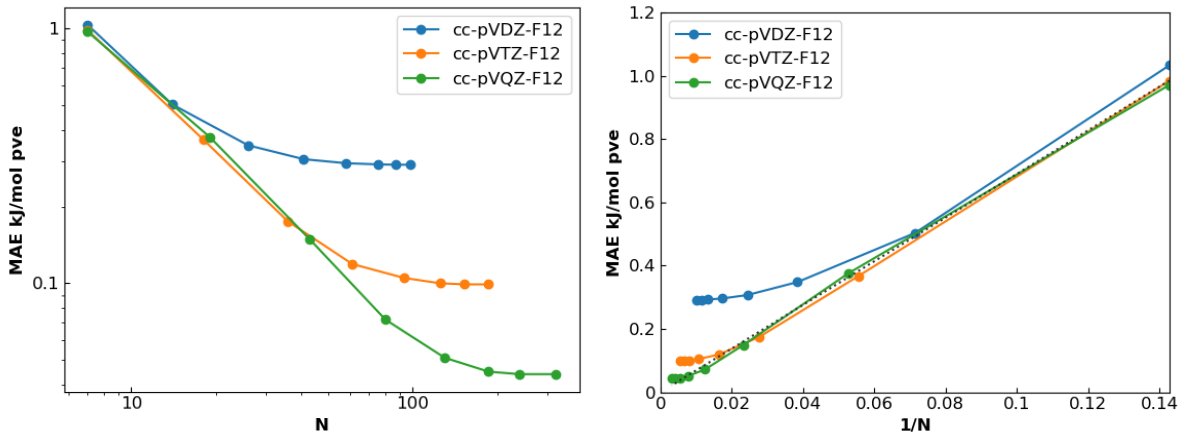


Figure 5.2: Mean Absolute Error in correlation energy in kJ/mol per valence electron as a function of (a) N and (b) $1/N$ for 105 reaction energies computed using PNO-MP2 method for cc-pVXZ-F12 (X=D,T,Q) basis sets where N is mean number of PNOs. Data points correspond to PNO thresholds of $-\log T = 3, 4, \ldots, 10$.

for sufficiently small N_{ij}, where E_∞^{ij} is the pair correlation energy at the basis set limit, and C_{ij} is a constant. It is then straightforward to derive the following two-point extrapolation formula to estimate the basis set limit, which would involve calculations using two different PNO thresholds corresponding to N_{ij} and M_{ij} number of functions in the retained PNO basis for the pair ij

$$E_\infty \approx \sum_{i \leq j} \frac{N_{ij} E^{ij}(N_{ij}) - M_{ij} E^{ij}(M_{ij})}{N_{ij} - M_{ij}}. \tag{5.4}$$

This approach is particularly attractive because it requires only a single basis set for the extrapolation. Moreover, the extrapolation relies on the decay behaviour of correlation energies corresponding to a small number of retained PNOs. As a result, relatively loose PNO thresholds should be employed for the calculations, making them more affordable.

In contrast, the standard basis set extrapolation method requires calculations using two basis sets in the same family with consecutive cardinal numbers X and Y. The standard extrapolation approach, first proposed by Helgaker *et al.*[149], relies on the decay behaviour of the basis set error in correlation energy $E(X)$ as a function of the basis set size represented by the cardinal number X of the basis set,

$$E(X) \approx E_\infty + CX^{-3}. \tag{5.5}$$

As previously noted, for a given atomic basis set of size M, the correlation energy slowly converges as M^{-1}. Since $M \propto X^3$, the convergence of correlation energy with respect to the

cardinal number follows an X^{-3} power law, as expressed in Equation (5.5). Thus, the following two-point formula can be derived to extrapolate to the basis set limit using basis sets with cardinal numbers X and $Y = X - 1$

$$E_\infty = \frac{X^3 E(X) - Y^3 E(Y)}{X^3 - Y^3}. \tag{5.6}$$

It is important to note that this extrapolation is designed for canonical energies $E(X)$ and $E(Y)$ corresponding to the two basis sets. However, in PNO methods, $E(X)$ and $E(Y)$ correspond to energies computed with a specific level of PNO truncation, determined by the user-defined PNO threshold. While the PNO truncation error is fixed by this threshold, it introduces varying levels of uncertainty into $E(X)$ and $E(Y)$. As a result, the quality of extrapolated energies may deteriorate when compared to extrapolating the canonical values. In this work, we aim to assess the impact of increasing PNO truncation error on the accuracy of X^{-3} extrapolated energies. Additionally, we compare the performance of X^{-3} and N_{ij}^{-1} extrapolation methods as a function of the PNO threshold.

5.1.3 Test Sets and Computational Details

We carry out numerical calculations on two test sets:

1. HCNOF set: the Bakowies test set[150], which consists of 106 molecules containing H, C, N, O, and F atoms. We also use a set of 105 linearly independent reactions created from the Bakowies test set by Tew *et al.*[148]

2. Cu set: also known as the CuNCDe33 set[151], this is a set of gas-phase noncovalent ligand dissociation reactions for Cu^+ complexes.

The HCNOF test set provides a broad representation of first-row chemistry. It includes molecules with a variety of bond types. The test set was designed to be "a fairly balanced set of neutral, singlet ground state molecules composed of these first-row elements, as complete as possible"[150]. This test set includes molecules that are either experimentally unknown or for which accurate thermochemical data are unavailable, thereby broadening the scope and representativeness of the data set. Additionally, it incorporates important fragments of larger organic molecules and small cyclic compounds to serve as representatives for larger, more complex systems that would be computationally prohibitive to study at the required high theoretical

levels. The HCNOF test set enables observing various effective convergence behaviours among molecules, which is critical for the analysis of extrapolation methods. Bakowies used the HCNOF set to examine the behaviour of Helagker's for correlation energies at the MP2 and CCSD levels of theory [150].

Transition metals are more challenging than main-group molecules due to relativistic effects, stronger electron correlation effects and the need for diffuse basis sets. This makes the Cu set a stringent test for local correlation methods. For the Cu test set, Minenkov *et al.* 151 benchmarked DLPNO-CCSD(T) with various treatments of relativity and CBS extrapolation against experimental data, and compared the results with the M06 density functional. The best agreement was obtained using DLPNO-CCSD(T) with scalar relativistic corrections, implemented either through effective core potentials (ECPs) or the Douglas–Kroll–Hess (DKH) Hamiltonian. In contrast, non-relativistic all-electron DLPNO-CCSD(T) consistently underestimated the Cu dissociation enthalpies. The M06 functional performed competitively, yielding results only slightly less accurate overall.

In this work, the selection of these test sets is also motivated by either the availability of basis set limit MP2 data or the feasibility of performing the necessary calculations to obtain such results. Basis set limit MP2 valence correlation energies for the HCNOF set are known to be within 99.95% [152] accuracy. We computed the same for the Cu set in this work using MP2-F12 theory using the aug-cc-pV5Z basis. The calculations employed the frozen core approximation, freezing the $1s$ orbitals for C, N, O, and F, and the $1s2s2p3s3p$ orbitals for Cu. The F12 correlation factor was represented as a linear combination of six Gaussians approximating a Slater-type function with an exponent of 1.0, a_0^{-1} [153].

For the complementary auxiliary basis sets, we used the optimised sets of Yousaf *et al.* for the main group atoms [154] and the def2-TZVPP Coulomb fitting basis for the Cu atom [155]. The density fitting approximation for the Fock and correlation integrals utilised the aug-cc-pV6Z basis sets for the main group atoms, while for Cu, the largest available sets optimised for the def2-QZVPP basis were employed [156]. Reference basis set limit correlation energies for the Cu set are provided in the appendix.

In our PNO-MP2 calculations to assess the extrapolation schemes, we used the aug-cc-pVXZ basis sets [157–159] with (X=D, T, Q). We focused on valence shell correlation energies, and the

frozen-core approximation was applied in all calculations. In the PNO-MP2 calculations, the IBO method with exponent 2 was used to localise the occupied orbitals[109]. The calculations were carried out for PNO thresholds ranging from 10^{-4} to 10^{-10} in increments of $1/10$. All calculations were performed using a developmental version of the TURBOMOLE program package[115].

The PNO-MP2 energies include a correction for discarded pairs of occupied orbitals, calculated as a byproduct of screening using the OSV-SOS-MP2 (orbital specific virtual scaled opposite spin) energy[160]. However, they do not account for the correction for discarded PNOs, referred to as the Δ correction. In our approach, the Δ correction is defined as the difference between the OSV-MP2 and PNO-MP2 semi-canonical pair energies. The Δ correction, defined as such, significantly reduces the PNO truncation error, as the OSV space is substantially larger than the PNO space for each pair.

Thus, PNO-MP2+Δ energies incorporate corrections for both discarded pairs and discarded PNOs, bringing them closer to canonical MP2 results. Consequently, it is methodologically consistent to apply Helgaker's X^{-3} basis set extrapolation to the PNO-MP2+Δ energies and N_{ij}^{-1} extrapolation to PNO-MP2 energies. For the N_{ij}^{-1} approach, PNO-MP2 pair energies computed using thresholds T and $10T$ are used, while the correction for discarded pairs is added separately. The X^{-3} extrapolation is applied to the PNO-MP2+Δ total correlation energies corresponding to the given T. For extrapolation to the canonical limit, we perform the three-point T^{α} extrapolation of PNO-MP2+Δ energies using thresholds T, $10T$, and $100T$.

We present results from six different computation approaches:

1. PNO-MP2
2. PNO-MP2+Δ
3. N_{ij}^{-1} extrapolation of PNO-MP2 pair energies to the complete basis set limit
4. Helgaker's X^{-3} extrapolation to the complete basis set limit applied to PNO-MP2+Δ energies
5. Three-point T^{α} extrapolation of PNO-MP2+Δ energies to the canonical limit
6. Double extrapolation, where the T^{α} extrapolated energies from approach 5 are further

Table 5.1: Mean absolute deviations from the basis set limit of total energies computed with and without using extrapolated PNO-MP2 correlation energies for aug-cc-pVXZ basis sets (kJ/mol per valence electron) for the HCNOF set.

				$-\log T$		
Method	Basis	4	5	6	7	8
PNO-MP2	DZ	31.5	27.2	26.5	26.3	26.3
	TZ	20.9	12.6	10.8	10.5	10.4
	QZ	19.0	8.5	5.5	4.9	4.8
PNO-MP2 (N_{ij}^{-1})	DZ	22.6	23.8	25.4	26.0	26.2
	TZ	10.4	7.3	8.9	9.9	10.3
	QZ	8.1	2.7	3.1	4.1	4.6
PNO-MP2+Δ	DZ	27.4	26.6	26.4	26.3	26.3
	TZ	12.3	10.8	10.5	10.4	10.4
	QZ	7.9	5.4	4.9	4.8	4.8
PNO-MP2+Δ (T^{α})	DZ	25.7	26.3	26.3	26.3	26.3
	TZ	9.2	10.4	10.4	10.4	10.4
	QZ	1.4	4.5	4.8	4.8	4.8
PNO-MP2+Δ (X^{-3})	(DT)	5.9	4.2	3.8	3.7	3.7
	(TQ)	4.7	1.4	0.8	0.7	0.7
PNO-MP2+Δ (T^{α}, X^{-3})	(DT)	2.3	3.7	3.7	3.7	3.7
	(TQ)	6.9	0.4	0.7	0.7	0.6

extrapolated to the basis set limit using the X^{-3} method

Errors are reported as mean absolute errors (MAE) in kJ/mol per valence electron for total energies and in kJ/mol for reaction energies. Additional statistical measures are provided in the supplementary material of Ref. 1.

5.1.4 Results and Discussion

Tables 5.1, 5.2, 5.3, and 5.4 report the basis set errors in total and relative energies for the two data sets analysed in this work.

Total energies to the basis set limit

We begin by examining the performance of the N_{ij}^{-1} and X^{-3} extrapolation methods, comparing their accuracy with that of PNO-MP2 and PNO-MP2+Δ values. We first focus on the basis set errors as a function of the average number of PNOs for total energies. The overall trends are illustrated in Figure 5.3a, which depicts the basis set errors in total energies for the HCNOF set. The PNO-MP2 and PNO-MP2+Δ values exhibit the anticipated trend: all basis sets display

Table 5.2: Mean absolute deviations from the basis set limit of total energies computed with and without using extrapolated PNO-MP2 correlation energies for aug-cc-pVXZ basis sets (kJ/mol per valence electron) for the Cu set. T^{α} extrapolation with PNO threshold 10^{-4} is not performed (indicated by '-') as calculation with PNO threshold 10^{-2} introduces large PNO truncation errors.

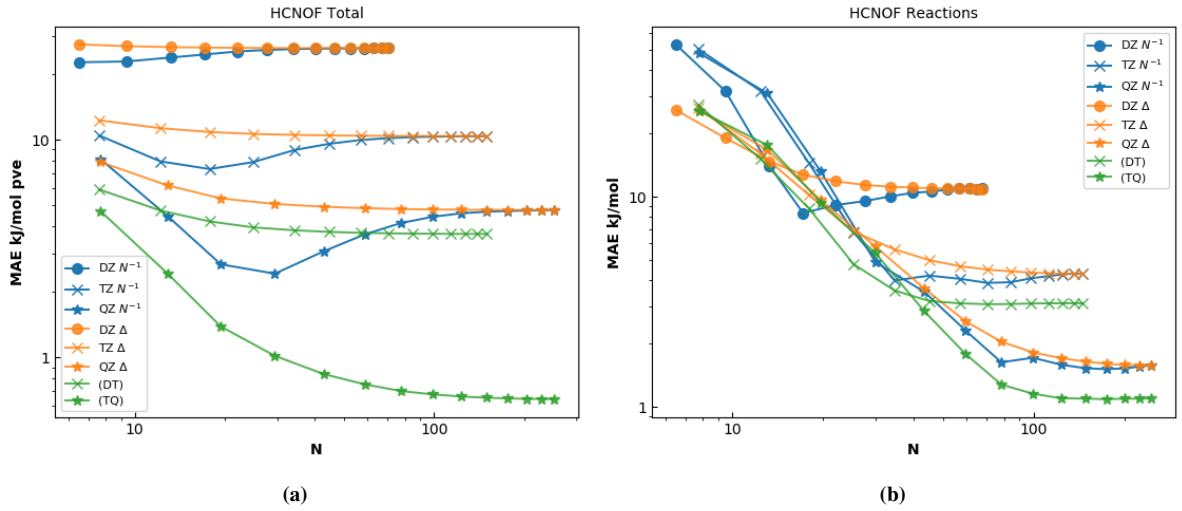
		$-\log T_{\mathrm{PNO}}$				
Method	Basis	4	5	6	7	8
PNO-MP2	DZ	31.6	26.8	25.8	25.8	25.6
	TZ	23.1	13.6	11.3	10.8	10.8
	QZ	21.3	9.8	5.9	5.1	5.0
PNO-MP2 (N^{-1})	DZ	22.9	22.8	24.6	25.3	25.5
	TZ	13.2	7.9	8.9	10.3	10.6
	QZ	11.1	3.6	3.0	4.2	4.8
PNO-MP2+Δ	DZ	26.8	25.9	25.6	25.6	25.5
	TZ	13.2	11.3	10.9	10.8	10.7
	QZ	9.2	5.8	5.1	5.0	5.0
PNO-MP2+Δ (T^{α})	DZ	–	25.7	25.5	25.5	25.5
	TZ	–	10.8	10.7	10.7	10.7
	QZ	–	4.4	5.0	4.9	4.9
PNO-MP2+Δ (X^{-3})	(DT)	7.4	5.2	4.7	4.5	4.5
	(TQ)	6.3	1.7	0.9	0.8	0.7
PNO-MP2+Δ (T^{α}, X^{-3})	(DT)	–	4.6	4.5	4.5	4.5
	(TQ)	–	0.4	0.8	0.7	0.7

Table 5.3: Mean absolute deviations from the basis set limit of reaction energies computed with and without using extrapolated PNO-MP2 correlation energies for aug-cc-pVXZ basis sets (kJ/mol) for the HCNOF set.

		$-\log T$				
Method	Basis	4	5	6	7	8
PNO-MP2	DZ	52.3	22.7	13.3	11.3	11.0
	TZ	54.6	21.9	8.8	5.2	4.5
	QZ	54.3	21.0	8.4	3.2	1.9
PNO-MP2 (N_{ij}^{-1})	DZ	53.2	14.0	9.1	10.0	10.6
	TZ	50.7	14.4	3.9	4.1	3.9
	QZ	48.2	13.2	3.5	1.6	1.6
PNO-MP2+Δ	DZ	25.9	14.7	11.8	11.2	10.9
	TZ	26.5	10.2	5.6	4.7	4.4
	QZ	25.7	9.6	3.7	2.0	1.7
PNO-MP2+Δ (T^{α})	DZ	27.0	11.6	10.8	11.0	10.9
	TZ	30.3	5.2	4.2	4.4	4.3
	QZ	80.1	6.4	1.7	1.6	1.6
PNO-MP2+Δ (X^{-3})	(DT)	27.5	8.8	3.6	3.1	3.1
	(TQ)	25.6	9.4	2.8	1.3	1.1
PNO-MP2+Δ (T^{α}, X^{-3})	(DT)	39.7	5.0	3.0	3.2	3.1
	(TQ)	134.9	10.7	1.5	1.3	1.1

Table 5.4: Mean absolute deviations from the basis set limit of reaction energies computed with and without using extrapolated PNO-MP2 correlation energies for aug-cc-pVXZ basis sets (kJ/mol) for the Cu set. T^{α} extrapolation with PNO threshold 10^{-4} is not performed (indicated by '-') as calculation with PNO threshold 10^{-2} introduces large PNO truncation errors.

		$-\log T$				
Method	Basis	4	5	6	7	8
PNO-MP2	DZ	29.7	11.6	3.4	2.5	2.6
	TZ	32.8	15.8	6.0	2.3	1.8
	QZ	29.8	14.7	5.8	1.7	0.6
PNO-MP2 (N^{-1})	DZ	27.1	7.8	2.6	2.8	2.7
	TZ	32.7	11.4	2.2	1.8	1.7
	QZ	30.5	11.7	1.5	0.9	0.7
PNO-MP2+Δ	DZ	10.7	3.5	2.5	2.5	2.6
	TZ	16.4	6.0	2.3	1.8	1.8
	QZ	14.5	5.2	1.4	0.6	0.6
PNO-MP2+Δ (T^{α})	DZ	–	3.1	2.9	2.7	2.6
	TZ	–	2.8	2.0	1.9	1.8
	QZ	–	4.6	0.9	0.7	0.6
PNO-MP2+Δ (X^{-3})	(DT)	18.9	7.2	2.8	1.9	1.7
	(TQ)	16.0	6.6	1.3	0.5	0.6
PNO-MP2+Δ (T^{α}, X^{-3})	(DT)	–	3.7	1.8	1.8	1.6
	(TQ)	–	7.3	1.3	0.6	0.7



(a) (b)

Figure 5.3: Mean Absolute Errors from basis set incompleteness in the correlation energy for (a) total and (b) reaction energies of the HCNOF set as a function of the average number of PNOs N, computed using three schemes: PNO-MP2 (N_{ij}^{-1}) extrapolation, PNO-MP2+Δ and X^{-3} extrapolation of PNO-MP2+Δ energies. Data points correspond to PNO thresholds of $-\log T = 3.5, 4, \ldots, 10$

significant errors at loose PNO thresholds, with errors gradually saturating to the canonical values as the number of PNOs increases. Since the Δ correction compensates for neglected PNOs, the PNO-MP2+Δ energies converge more quickly to the canonical values for each basis set. Naturally, the impact of the Δ correction is more pronounced at loose thresholds than at tight ones.

The N_{ij}^{-1} extrapolated total energies exhibit significantly smaller basis set errors compared to the PNO-MP2 canonical energies when using loose thresholds ($T \geq 10^{-6}$), confirming the anticipated extrapolation toward the basis set limit. For tight thresholds, the N_{ij}^{-1} extrapolation has minimal impact, as the data points used fall within the plateau regions of Figure 5.3a, where values are already similar and close to the canonical results. For total energies, the smallest basis set errors are obtained with $T = 10^{-5}$ and larger basis sets.

The X^{-3} extrapolation behaves consistently, showing a reduction in basis set errors across all PNO thresholds. Even at loose thresholds, the X^{-3} extrapolation lowers the basis set errors to values below the canonical results. Compared to the N_{ij}^{-1} extrapolation, the X^{-3} method systematically achieves smaller basis set errors, largely due to the advantage provided by the Δ correction.

Total energies to the canonical limit

Turning to the performance of the T^{α} extrapolation, the results in Tables 5.1 and 5.2 show that the three-point extrapolation effectively reduces the PNO truncation error, achieving an improvement comparable to tightening the PNO threshold by one to two orders of magnitude. Using $-\log_{10} T = 6$ or looser thresholds yields results that are remarkably close to the canonical limit. This substantial reduction in the PNO truncation error also enhances the performance of the subsequent X^{-3} extrapolation, particularly when applied with loose PNO thresholds.

Relative energies to the basis set limit

We now turn to the analysis of reaction energies. Accurate reaction energies can be obtained either from total energies that are tightly converged to the basis set limit or from the systematic cancellation of basis set errors in the energy differences of the reacting systems. The extent of error cancellation is expected to vary across the computational schemes employed in this study.

HCNOF set:

We first examine the basis set errors in reaction energies for the HCNOF set, as reported in Table 5.3 and illustrated in Figure 5.3b. We observe that despite improvements in total energies with larger basis sets, the PNO-MP2 and PNO-MP2+Δ calculations with loose thresholds ($T = 10^{-4}$ and 10^{-5}) yield very similar reaction energies for the three atomic basis sets. This is because the number of functions in the PNO basis, which remains nearly constant across the three basis sets for loose thresholds, plays a more critical role in distinguishing chemical environments than the refinement provided by larger atomic bases. To fully exploit the benefit of the TZ basis, a threshold of at least $T = 10^{-6}$ is required, while for the QZ basis, a threshold of $T = 10^{-7}$ or tighter is necessary.

This trend is also evident in the basis set errors obtained from X^{-3} extrapolated energies. Unlike total energies, Helgaker's extrapolation offers very little or no improvement in reaction energies when using a loose threshold. This suggests that while extrapolation consistently recovers more correlation energy, the broader distribution of basis set errors at looser thresholds leads to greater inaccuracies in reaction energies. For instance, results from (DT) extrapolation with $T = 10^{-5}$ are inferior to those from a direct TZ calculation with $T = 10^{-6}$. Similarly, (TQ) extrapolation with $T = 10^{-6}$ produces larger basis set errors compared to a direct QZ calculation with $T = 10^{-7}$. These findings emphasize the necessity of tight thresholds to harness the advantages of larger basis sets. Specifically, for a (TQ) extrapolation to be effective, a threshold of at least $T = 10^{-7}$ is required.

Cu set:

Examining the results for the binding energies of the Cu set in Table 5.4, we observe that the X^{-3} extrapolation is less consistent. Specifically, at a given PNO truncation threshold, the basis set errors do not always decrease systematically from DZ to TZ to QZ, and in many cases, the extrapolated values are worse than those obtained without extrapolation. The X^{-3} extrapolation shows a systematic improvement only when very tight thresholds ($T \leq 10^{-7}$) are used. The source of this unexpected behaviour remains unclear, but potential contributing factors include suboptimal basis set performance for Cu compared to main group elements and ambiguities in assigning the cardinal number X to a basis set containing both main group and transition metal atoms.

In contrast, the N_{ij}^{-1} extrapolation consistently reduces basis set errors across all PNO truncation thresholds. This extrapolation relies on the systematic reduction of basis set error with the number of functions within a given basis, rather than between different basis sets, resulting in smoother behaviour.

Relative energies to the canonical limit

The error due to PNO truncation is significantly diminished when the T^{α} three-point extrapolation is employed. This approach allows the advantage of larger basis sets to be realised by combining information from PNO calculations with loose thresholds, provided the thresholds are at least 10^{-3}, as required for T^{α} extrapolation with $T = 10^{-5}$. Similar to total energies, the T^{α} extrapolation reduces the PNO truncation error for reaction energies by an amount equivalent to tightening the threshold by one order of magnitude. This reduction carries over to the subsequent X^{-3} basis set extrapolation, yielding results that closely approach the canonical limit when using extrapolation with $T = 10^{-6}$.

Cost-performance comparison

When evaluating the absolute performance of various methods for a given computational cost, the results are more nuanced. The computational cost of PNO-MP2 calculations scales approximately quadratically with the size of the AO basis per atom and roughly doubles with each order of magnitude reduction in the PNO threshold. Consequently, the overall cost of each scheme is dictated by its most expensive calculation, typically the one involving the largest basis set and the tightest threshold.

For the DZ basis set or loose thresholds of $T \geq 10^{-5}$, the errors in N_{ij}^{-1} extrapolated reaction energies are either comparable to or slightly worse than the PNO-MP2+Δ energies. In such cases, the additional computational expense of N_{ij}^{-1} extrapolation is not justified. Notably, the Δ correction has no computational overhead and is essentially cost-free. However, for TZ or QZ basis sets with $T \leq 10^{-6}$, N_{ij}^{-1} extrapolation outperforms the standard PNO-MP2+Δ method for the HCNOF set, yielding errors of just 4 kJ/mol with a TZ basis and $T = 10^{-6}$.

To evaluate the relative performance of the X^{-3} and N_{ij}^{-1} extrapolation methods, we compare (DT) with TZ N_{ij}^{-1} and (TQ) with QZ N_{ij}^{-1} for each threshold. As shown in Figure 5.3b, for the

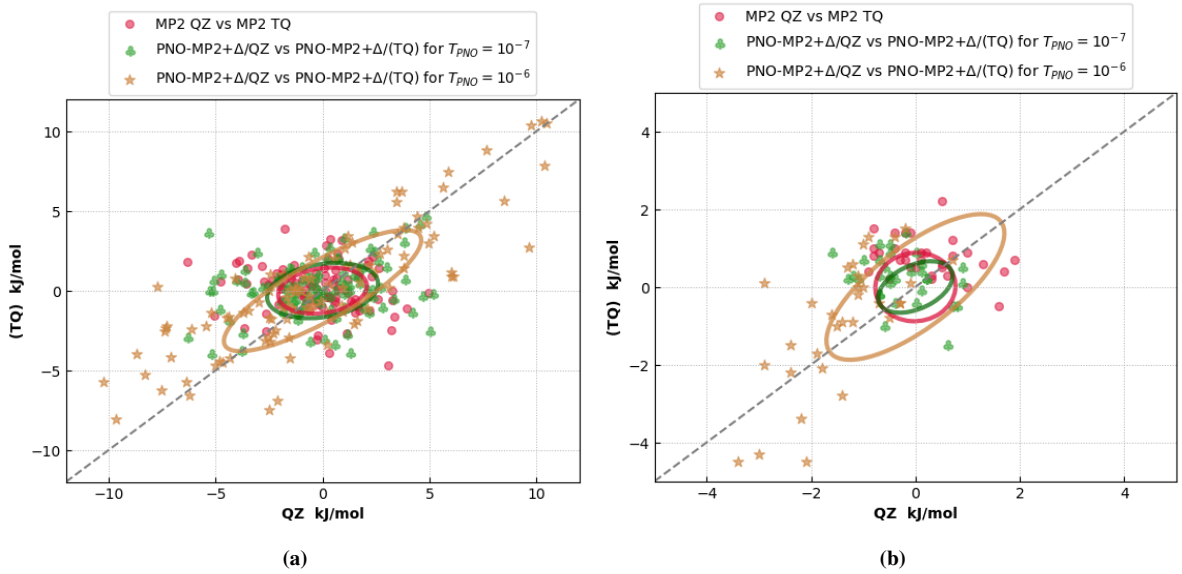


Figure 5.4: The correlation between QZ and (TQ) basis set errors for reaction energies of (a) the HCNOF set and (b) the Cu set, using canonical MP2 and PNO-MP2+Δ with $T_{\mathrm{PNO}} = 10^{-6}$ and 10^{-7}.

HCNOF reaction energies, the X^{-3} method provides significantly smaller errors than the N_{ij}^{-1} approach for loose thresholds, and marginally smaller errors for tight thresholds. For the Cu set, both methods yield similar results when tight thresholds are used. Overall, to achieve basis set errors with an MAE below 4 kJ/mol, the optimal combination of a TZ basis and $T = 10^{-6}$ is required for both extrapolation methods.

False basis set convergence in PNO methods

Our calculations highlight that the errors in reaction energies obtained for a given loose threshold are very similar across the DZ, TZ, and QZ basis sets, as well as for (DT) and (TQ) extrapolated values. Consequently, there is a risk of obtaining false convergence, where the energies appear to saturate with basis set size but retain large residual basis set errors due to the PNO truncation. Figure 5.4 illustrates the correlation between QZ and (TQ) basis set errors using PNO-MP2+Δ with $T_{\mathrm{PNO}} = 10^{-6}$ and 10^{-7}, alongside canonical MP2 for the two datasets. The zero-mean joint Gaussian distributions for the data sets are shown through ellipses encompassing the $\pm\sigma$ regions, which were computed from the zero-mean covariances.

Data points lying between the 45-degree dotted line and the x-axis indicate cases where extrapolation reduces the error, while data points outside this region correspond to situations where reaction energy basis set errors increase upon extrapolation. Points along the diagonal represent

false convergence, where the errors remain unchanged. For both the HCNOF and Cu sets, the covariances of the error distributions obtained using $T = 10^{-6}$ lie largely along the 45-degree axis, suggesting little improvement from QZ to (TQ) and a high risk of false convergence. This risk is significantly reduced when using $T = 10^{-7}$, where the joint distributions are close to the canonical values, and (TQ) provides a marked improvement over QZ.

5.2 Extrapolation of PNO-CCSD(T) Energies

Having studied the interplay between PNO truncation error and AO basis set error at MP2 level in weakly correlated systems, in the second half of this chapter, we analyse PNO truncation errors for strongly correlated systems at PNO-CCSD(T) level and provide recommendations for reliably extrapolating to the limit of a complete PNO space (CPS). Martin and colleagues conducted numerical studies evaluating the accuracy of PNO-CCSD(T) relative to canonical CCSD(T) in metal-organic systems[161]. Their findings indicate that for systems with moderate static correlation, PNO truncation errors can reach several kcal/mol when using standard thresholds of $T = 10^{-6.5}$ or $T = 10^{-7}$. While tightening the PNO threshold recovers the canonical result, achieving errors below 1 kcal/mol requires very tight thresholds of $T = 10^{-8}$ or lower. Similarly, Sandler *et al.* report significant PNO truncation errors in reaction barriers for both open- and closed-shell organic reactions when employing default thresholds[162]. Therefore, it is important to carefully control the PNO truncation error, especially when employing PNO methods for systems exhibiting moderate static correlation. As observed previously at MP2 level, controlling the PNO truncation error also becomes essential when using large basis sets as a dominant PNO truncation error may lead to false convergence of basis set error. In such cases, basis set extrapolation fails to recover the complete basis set (CBS) limit.

5.2.1 Extrapolation Error Models for PNO-CCSD(T)

Altun *et al.* investigated numerical fits for the behaviour of the PNO truncation error as a function of the threshold T and proposed the error model[163]

$$E(T) = E + B(\log_{10} T)^{\beta}, \tag{5.7}$$

where E represents the canonical energy without PNO truncation, and $E(T)$ is the energy computed using a PNO threshold T, typically within the range 10^{-5}–10^{-9}. However, this model does not fit any of our data. Also, Altun *et al.* did not use this model for extrapolation but instead employed a general two-point extrapolation formula:

$$E \approx E(T_1) + F(E(T_2) - E(T_1)), \tag{5.8}$$

which does not assume a specific error model. The factor F is determined for a given pair of thresholds by fitting to data, and they recommend $F = 1.5$ for (6,7) and (7,8) extrapolations, irrespective of the basis set. Here, (6,7) refers to extrapolation using $T_1 = 10^{-6}$ and $T_2 = 10^{-7}$.

As demonstrated in Section 5.1.4, applying a three-point extrapolation scheme to MP2 energies reduces the PNO truncation error in reaction energies to the equivalent of a 50-fold reduction in T, effectively eliminating the truncation error without the computational cost of very tight thresholds. However, initial attempts to apply this approach to PNO-CCSD and PNO-CCSD(T) energies were unsuccessful. The convergence of PNO-CCSD energies with T does not follow the MP2 error model due to the differing convergence behaviour of the ring and ladder terms in the CCSD amplitude equations.

By fixing $\alpha = 0.5$ in Equation (5.1), a two-point extrapolation formula can be derived:

$$E \approx \tilde{E} = \frac{T_2^\alpha E(T_1) - T_1^\alpha E(T_2)}{T_2^\alpha - T_1^\alpha}, \tag{5.9}$$

which can also be rewritten in the Schwenke[164] form:

$$E \approx E(T_1) + F(E(T_2) - E(T_1)), \quad F = \frac{T_1^\alpha}{T_1^\alpha - T_2^\alpha}. \tag{5.10}$$

Thus, by choosing $F = 1.5$ for (6,7) and (7,8) extrapolations, Altun *et al.* implicitly assume a polynomial error model with $\alpha = 0.4771$. Understanding the underlying error model enables applying extrapolations flexibly using different threshold choices, such as (6.5,7), where $F = 2.366$.

So, we investigate the error models described by Equation (5.1), as well as its variant with α fixed at 0.5, in the context of the PNO-CCSD(T) method. Our analysis is based on two

benchmark data sets: the ISOL24 set of Huenerbein *et al.*[165] and the MOBH35 set of Iron and Janes.[166]

The ISOL24 set consists of weakly correlated organic isomers containing up to 81 atoms. It presents a significant challenge for PNO methods, as it involves molecules with distinct chemical connectivity, spatial arrangements, and long-range dispersion interactions, limiting the potential for error cancellation in local approximations. Recently, Werner and Hansen reported basis set limit isomerization energies using PNO-LCCSD(T)-F12b theory,[167] providing a valuable reference for this study.

The MOBH35 set, which includes metal-organic reaction barriers, poses a different challenge due to the presence of significant static correlation. Semidalas and Martin[161] previously used this set to highlight the slow convergence of reaction barriers with respect to PNO threshold, as well as unexpectedly large discrepancies between different PNO implementations.

5.2.2 Computational Details, Structures and Basis Sets

All calculations were performed using the TURBOMOLE program package.[115] All reported timings were obtained on a single Intel(R) Xeon(R) Gold 6248R CPU @ 3.00GHz node with 48 cores, 380 GB RAM, and 1.8 TB SSD storage.

The structures for the ISOL24 set were obtained from the supporting information of Ref. 165. PNO-CCSD(T) calculations for these molecules were carried out using the cc-pVDZ, cc-pVTZ, and cc-pVQZ basis sets,[157], avoiding problems of internal basis set superposition errors in extended systems.

For the MOBH35 test set, molecular structures were taken from Ref. 161. The transition state structures for reactions 11 and 12, as well as all species in reaction 14, were modified according to the recommendations of Dohm *et al.*[168] PNO-CCSD(T) calculations employed the def2-SVP, def2-TZVPP, and def2-QZVPP basis sets,[169] facilitating direct comparison with previous studies. For molecules containing second- and third-row transition metals, Stuttgart relativistic effective core potentials were applied.[170]

HF and PNO-CCSD(T) calculations

HF calculations were performed using the `dscf` module,[171] of TURBOMOLE which does not approximate Coulomb integrals via density fitting. Special care was required for reactant 16 of the MOBH35 set, where the default extended Hückel guess led to incorrect state convergence.

PNO-CCSD(T) calculations were performed using the `pnoccsd` program in TURBOMOLE. Density fitting approximations were used for Coulomb integrals, with the corresponding Coulomb auxiliary basis sets[172,173] applied in all cases. The domain-based PNO-CCSD(T) implementation follows the principal domain approach,[174] where PAO domains are selected based on an approximate MP2 density, constructed in the orbital-specific virtual (OSV) basis while neglecting off-diagonal Fock matrix elements in the occupied space.[175,176] The OSV truncation threshold is directly linked to the PNO threshold.

The CCSD amplitude equations were solved in the PNO basis without applying weak-pair approximations,[177,178] which could introduce additional uncertainty in analysing the PNO truncation error. Weak-pair suppression was enforced using the keyword `multilevel off` in the `$pnoccsd` data group. The (T) energy was computed in the basis of triple natural orbitals (TNOs)[179] using Laplace integration,[180] with a convergence threshold of 0.01 determining the Laplace grid. In all cases, computed energies include a correction term estimating the contribution from discarded pairs and PNOs at the MP2 level, neglecting Fock coupling effects.

A significant computational bottleneck in PNO methods is the storage of density fitting intermediates $(Q|ab)$, required for ladder terms in the CCSD equations. Despite restricting the auxiliary functions Q to a pair domain, large basis sets, tight PNO thresholds, and strict density fitting settings can lead to storage requirements exceeding 1 TB. To address this, we implemented direct evaluation of $(ab|cd)$ and $(ab|ck)$ integrals, avoiding explicit storage of three-index intermediates. This was enabled using the `direct` keyword.

Canonical CCSD(T) calculations

Canonical CCSD(T) calculations were performed using the `ccsdf12` module of TURBOMOLE, employing density fitting for all integrals to ensure exact correspondence with the CPS limit of the PNO-CCSD(T) method. This was enforced via the `risingles` and `riladder` keywords in the `$ricc2` data group.

We successfully computed canonical CCSD(T) energies for molecules in reactions 3, 4, 6, 7, 14, 15, 16, 21, 26, 27, and 30–35 of the MOBH set using the def2-SVP and def2-TZVPP basis sets, denoted as the MOBH16 subset. Similarly, canonical CCSD(T) energies at the cc-pVDZ and cc-pVTZ levels were obtained for all ISOL24 isomer pairs except 1, 4, 6, 7, 16, and 24, defining the ISOL18 subset.

5.2.3 Results and Discussion

5.2.3.1 Error model $E(T) = E + AT^{\alpha}$

Based on the findings of Altun *et al.*[163], the model $E(T) = E + AT^{\alpha}$ with $\alpha \approx 0.5$ is expected to approximate PNO-CCSD(T) truncation errors.

In this study, we address two key questions:

1. To what extent does this error model accurately represent PNO truncation errors in coupled-cluster energies?
2. How does the exponent α depend on the molecular system and correlation method?

To answer these questions, we examine PNO truncation errors in MP2, CCSD, (T), and CCSD(T) correlation energies for an example system (educt number 20 from the ISOL24 set, computed using a cc-pVTZ basis). Figure 5.5 presents a log-log plot of the truncation error $E(T) - E$ as a function of T. The best-fit lines, obtained for thresholds $T = 10^{-6}$ to 10^{-8}, include the corresponding α values in the legend. The trends observed for this example are consistent across the ISOL24 and MOBH35 test sets.

In agreement with our previous findings, the PNO-MP2 truncation error closely follows the error model $E(T) = E + AT^{\alpha}$ with an exponent of $\alpha = 0.44$ in this case. In contrast, the PNO-CCSD truncation error deviates significantly from this model, yielding smaller errors than expected at loose PNO thresholds. This deviation arises from the correction term added to account for the contribution of discarded PNOs, which is computed at the MP2 level. At the CCSD level, this correction term overestimates the actual error from discarded PNOs and decays at a rate different from the CCSD energy error. As a result, extrapolating PNO-CCSD energies to the CPS limit using simple one-component error models is unlikely to be effective.

In contrast, truncation errors in the (T) energy follow the simple error model more closely.

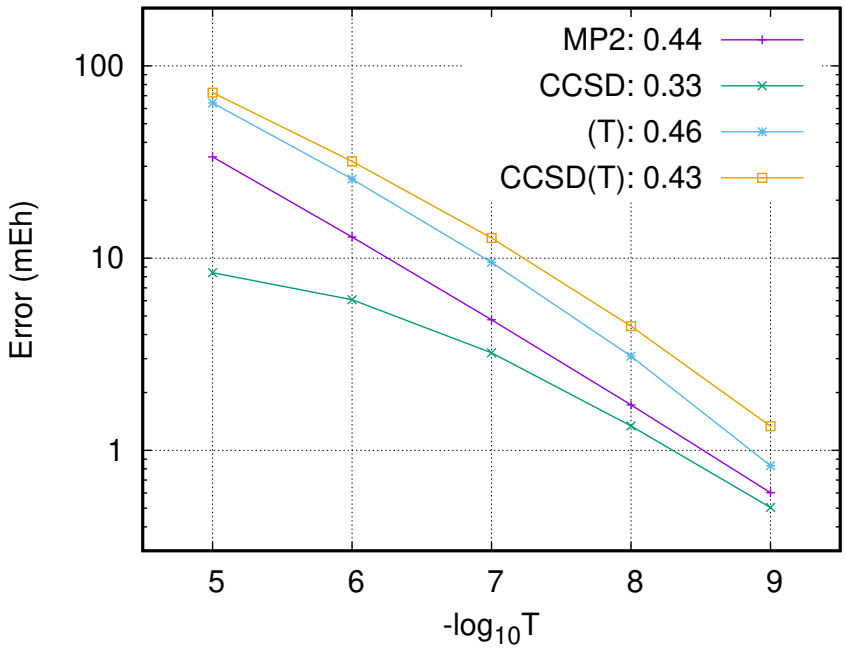


Figure 5.5: PNO truncation errors for educt number 20 of the ISOL24 set using a cc-pVTZ basis. The legend includes the value of α from the best fit to $\log_{10}(E(T) - E) = \log_{10} A + \alpha \log_{10} T$.

This error primarily depends on the TNO truncation threshold, which is set equal to the PNO threshold. Two factors contribute to (T) energy errors:

- The TNO truncation itself, which dominates and follows the same power-law dependence as PNO-MP2.
- The error in CCSD amplitudes used to compute (T), which follows the trend observed in CCSD.

Since the TNO error is the primary source of total PNO-CCSD(T) error, extrapolating PNO-CCSD(T) energies to the CPS limit using simple models is feasible. However, if future improvements in TNO construction reduce (T) errors, extrapolation will become more challenging due to the increasing significance of CCSD contributions.

Variability of α across molecules

To assess the generality of the error model, we performed linear fits using

$$\log_{10}(E(T) - E) = \log_{10} A + \alpha \log_{10} T \tag{5.11}$$

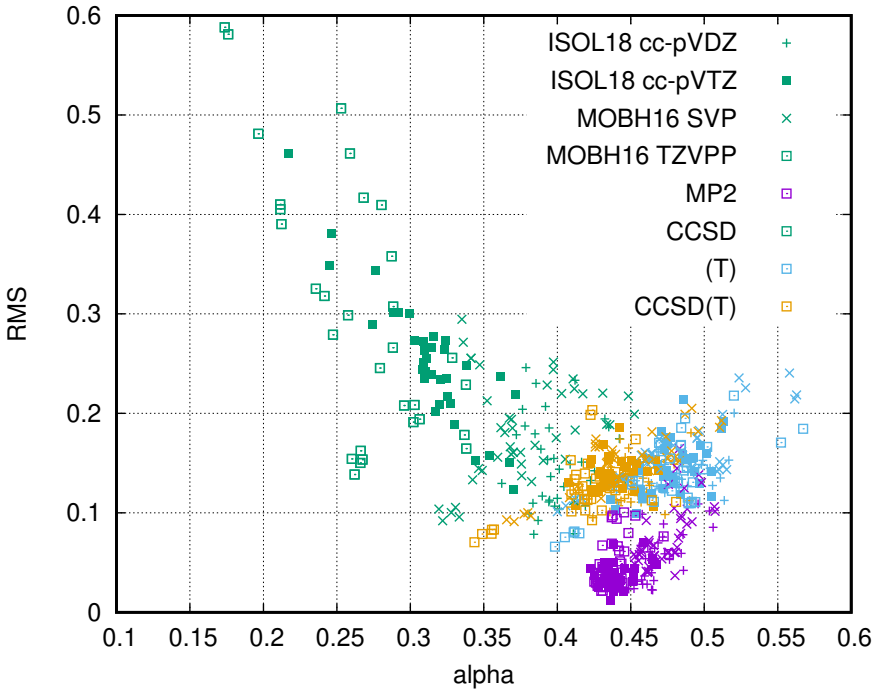


Figure 5.6: Values of α from linear fits using Equation (5.11) against RMS deviation, for PNO truncation errors in MP2, CCSD, and CCSD(T) energies.

for all molecules where canonical energies were available. Figure 5.6 presents a scatter plot of α values versus root mean squared (RMS) deviation from the model for MP2, CCSD, and CCSD(T) truncation errors.

The results confirm that PNO-MP2 truncation follows the error model closely, with α values near 0.5 and weak dependence on system and basis set. However, CCSD shows significant deviations, with α ranging from 0.1 to 0.5, reflecting varying degrees of ring-ladder error cancellation. These deviations are larger for triple-ζ than double-ζ basis sets, but no obvious trend emerges when comparing the MOBH16 and ISOL18 sets. The (T) contribution, in contrast, adheres more closely to the model, with moderate deviations from the ideal $\alpha = 0.5$.

Implications of α on extrapolation

Our study at MP2 level used the three-point extrapolation scheme (Equation (5.2)) that determines α case-by-case based on energy convergence. However, for accurate extrapolation, α must remain approximately constant across the T values used. Given the canonical limit E, we

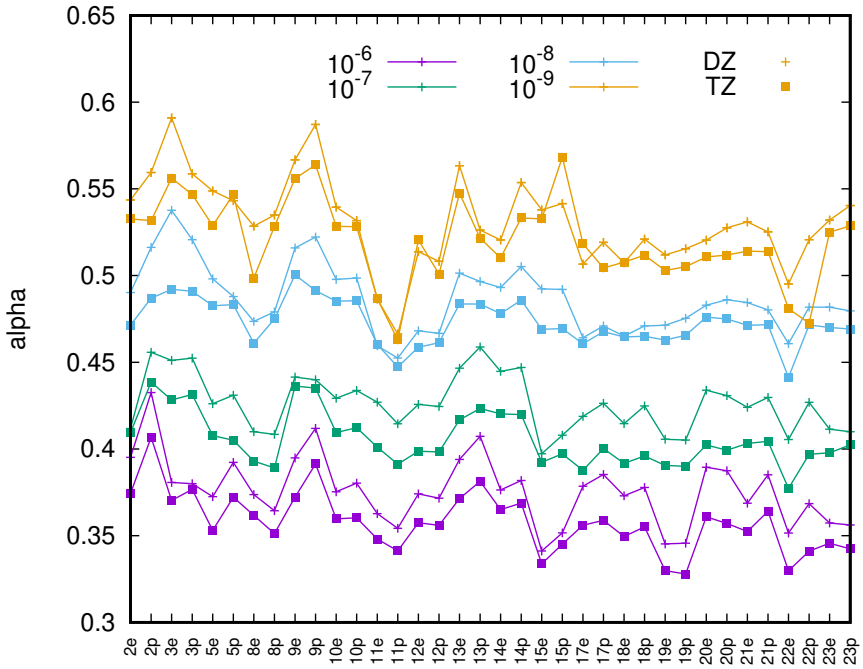


Figure 5.7: Values of $\alpha(T)$ from Equation (5.12) for PNO-CCSD(T) energies of molecules in the ISOL18 set.

define an effective exponent $\alpha(T)$ as

$$\alpha(T) = \log_{10}\left(\frac{E(10T) - E}{E(T) - E}\right) \tag{5.12}$$

Figure 5.7 displays $\alpha(T)$ for $T = 10^{-6}, 10^{-7}, 10^{-8}$, and 10^{-9} in CCSD(T) calculations for the ISOL18 set. Notably, α exhibits significant variation with T, exceeding the variation observed between molecules or basis sets. This explains why the three-point extrapolation approach was ineffective for PNO-CCSD(T) and why fixing $\alpha \approx 0.5$ for a two-point extrapolation is more reliable.

5.2.3.2 Error model $E(T) = E + A(T)T^{1/2}$

We now discuss the alternative, two-point extrapolation scheme obtained by fixing the exponent α at its ideal value of 0.5. By doing so, the PNO truncation error can be expressed without loss of generality as $E(T) = E + A(T)T^{1/2}$. The two-point extrapolation method assumes that the prefactor $A(T)$ remains approximately constant, ensuring accurate extrapolation when this

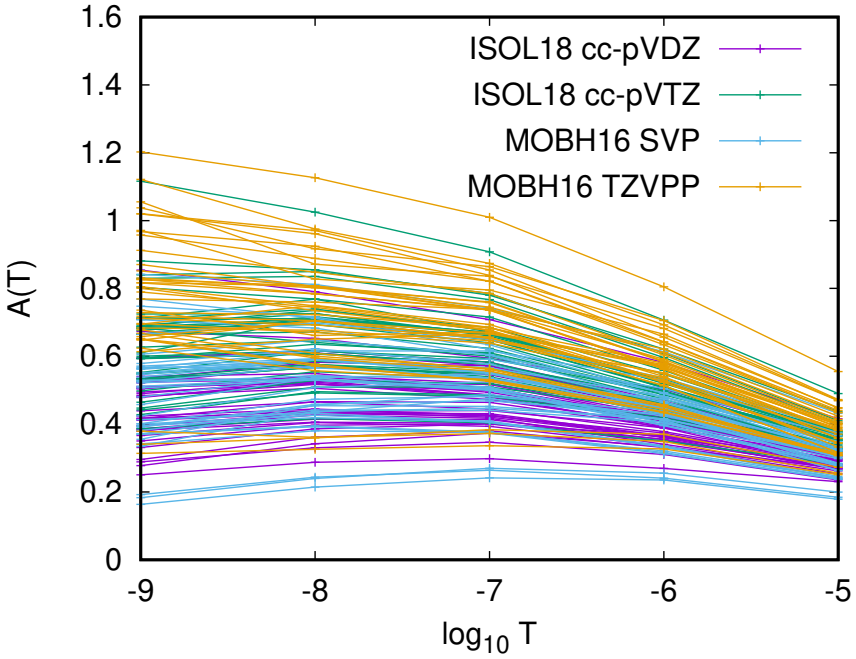


Figure 5.8: Values of $A(T)$ in the error model $E(T) = E + A(T)T^{1/2}$ for PNO-CCSD(T) energies, expressed in mE_h per valence electron.

assumption holds. Applying the two-point extrapolation formula yields

$$\tilde{E} = \frac{T_2^{1/2}E(T_1) - T_1^{1/2}E(T_2)}{T_2^{1/2} - T_1^{1/2}} \tag{5.13}$$

$$= E + \frac{T_1^{1/2}T_2^{1/2}}{T_2^{1/2} - T_1^{1/2}}(A(T_1) - A(T_2)). \tag{5.14}$$

If $A(T)$ increases with T, the extrapolation predicts correlation energies below the canonical limit, whereas $A(T)$ decreasing with T leads to underestimating the correlation energy.

Figure 5.8 presents the values of $A(T)$ for molecules in our test sets where canonical energies are available. Since the prefactor $A(T)$ scales with the number of correlated electrons, similar to the total correlation energy, we express $A(T)$ in units of mE_h per valence electron. The magnitude of $A(T)$ provides insight into the strength of electron correlation, with larger values observed for more strongly correlated systems. Additionally, $A(T)$ increases with the size of the AO basis set, reflecting the greater recovery of correlation energy.

Although $A(T)$ is not strictly constant as a function of T, its variation remains relatively small for most molecules, particularly within the range $T = 10^{-6}$–10^{-8}. Consequently, the two-point extrapolation method is expected to perform well in these cases.

Testset	Basis	Error	10^{-6}	(5, 6)	10^{-7}	(6, 7)	10^{-8}	(7, 8)	10^{-9}	(8, 9)
ISOL18	cc-pVDZ	AV	−0.35	−0.30	−0.19	−0.11	−0.07	−0.02	−0.02	−0.00
		RMS	0.98	0.66	0.47	0.26	0.18	0.06	0.07	0.03
		MAX	2.39	−1.51	−1.14	−0.68	−0.43	−0.21	−0.18	−0.06
	cc-pVTZ	AV	−0.40	−0.33	−0.21	−0.12	−0.09	−0.04	−0.03	0.00
		RMS	1.12	0.78	0.55	0.31	0.23	0.11	0.08	0.04
		MAX	−2.64	−1.86	−1.29	−0.92	−0.65	−0.42	0.22	0.09
	(DT)	AV	−0.42	−0.34	−0.22	−0.12	−0.10	−0.04	−0.03	0.00
		RMS	1.19	0.83	0.58	0.34	0.26	0.14	0.09	0.05
		MAX	−2.85	−2.01	−1.36	−1.01	−0.75	−0.52	0.24	−0.11
MOBH16	def2-SVP	AV	0.28	0.16	0.10	0.02	0.03	−0.01	0.00	−0.01
		RMS	0.70	0.48	0.28	0.15	0.13	0.08	0.06	0.03
		MAX	1.65	1.38	0.67	−0.54	0.33	−0.29	0.14	−0.08
	def2-TZVPP	AV	0.30	0.15	0.12	0.03	0.03	−0.00	0.01	−0.00
		RMS	0.87	0.52	0.37	0.20	0.16	0.10	0.07	0.05
		MAX	−2.33	1.22	−0.89	−0.54	0.40	−0.41	0.20	−0.12
	(ST)	AV	0.31	0.14	0.13	0.04	0.04	−0.00	0.01	0.00
		RMS	0.95	0.56	0.40	0.22	0.17	0.11	0.08	0.06
		MAX	−2.63	−1.21	−1.01	−0.54	0.42	−0.46	0.23	−0.14

Table 5.5: PNO-CCSD(T) truncation error statistics for $T = 10^{-6}$–10^{-9} in kcal/mol with and without two-point CPS extrapolation

Assessment of CPS and CBS extrapolation

In Table 5.5, we report the average (AV), root mean square (RMS), and maximum (MAX) deviations from the CPS limit for PNO-CCSD(T) energies. The results include ISOL18 isomerization energies and MOBH16 barrier heights, evaluated at PNO thresholds $T = 10^{-6}$ to 10^{-9}, alongside two-point CPS extrapolations. The notation (6, 7), for instance, refers to extrapolation using thresholds $T = 10^{-6}$ and $T = 10^{-7}$. The extrapolation follows Equation (5.9) with $\alpha = 0.5$, corresponding to $F = 1.462$ in Equation (5.10).

CPS extrapolation reduces PNO truncation error by approximately a factor of two–effectively equivalent to lowering the PNO threshold by an order of magnitude. This trend is consistent across both test sets and all basis sets considered. For the default threshold $T = 10^{-7}$, RMS errors are about 0.5 kcal/mol, with outliers reaching 1.5 kcal/mol. Thus, the default threshold does not guarantee PNO truncation errors below the 1 kcal/mol benchmark of chemical accuracy. The CPS (6,7) extrapolation significantly mitigates this issue, though some outliers remain around 1 kcal/mol. Ensuring chemical accuracy requires a tighter threshold of $T = 10^{-8}$. Using (7,8) CPS extrapolation reduces the maximum truncation error to 0.5 kcal/mol.

Table 5.5 also presents results for CBS extrapolation, where PNO-CCSD(T) energies from two basis sets are used to estimate the complete basis set (CBS) limit. We apply Helgaker's two-

point scheme[181], with a cardinal number of 2 for the def2-SVP and cc-pVDZ basis sets and 3 for the def2-TZVPP and cc-pVTZ basis sets. PNO truncation error increases with basis size and is slightly magnified in CBS extrapolation due to error propagation. Thus, employing tight PNO thresholds and CPS extrapolation becomes even more critical, reinforcing the conclusions of the work at MP2 level.

The computational cost of PNO-CCSD(T) scales steeply, increasing by a factor of 2–3 with each tenfold decrease in T, and similarly with each increment in the AO basis cardinal number. Large-basis, tight-threshold PNO-CCSD(T) calculations are computationally demanding and may exceed common disk and memory limitations. Explicitly correlated F12 methods[182] offer a solution to this bottleneck, but accessing the basis set limit via conventional methods remains valuable.

Scaling the PNO truncation error

A practical strategy to reduce PNO truncation error in large-basis PNO-CCSD(T) calculations is to estimate the error using a smaller basis set or a lower-cost method, followed by a correction[183,184]. This approach assumes a roughly constant PNO truncation error across methods and basis sets. However, as noted earlier, the prefactor $A(T)$ depends significantly on the basis set and varies even more across correlation methods. As shown in Figure 5.9, the ratio of $A(T)$ between different basis sets is only weakly dependent on T. A similar, albeit weaker, trend holds for the ratio between correlation methods. This observation allows for an accurate estimation of the PNO truncation error scaling factor:

$$E_X(T) = E_X + f(T)A_Y(T)T^{1/2}, \tag{5.15}$$

$$f(T) = \frac{A_X(T)}{A_Y(T)} \approx \frac{E_X(T_2) - E_X(T_1)}{E_Y(T_2) - E_Y(T_1)}, \tag{5.16}$$

where X represents an expensive method/basis set combination, and Y denotes a lower-cost alternative. Since $f(T)$ is only weakly dependent on T, it can be computed with relatively

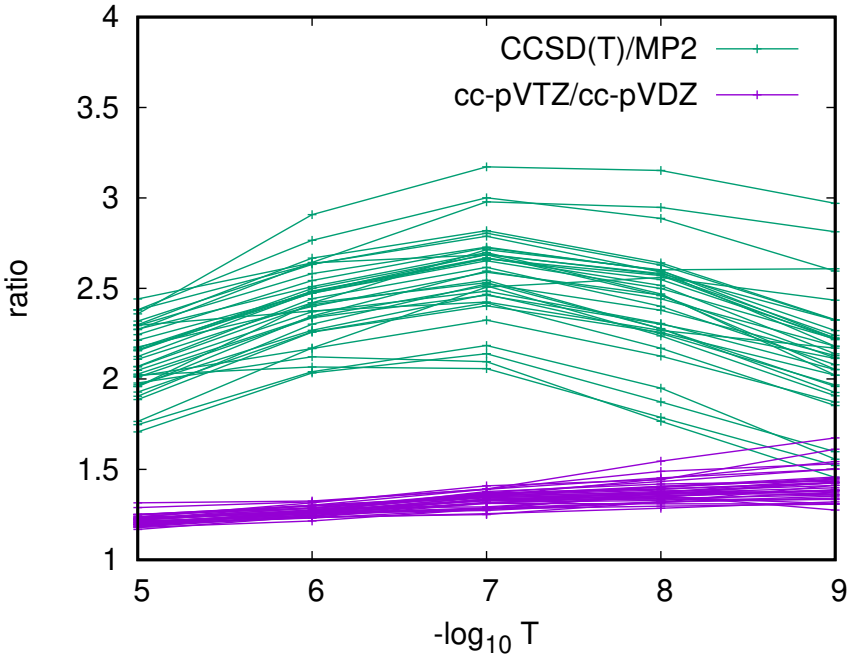


Figure 5.9: Ratios of $A(T)$ between cc-pVTZ and cc-pVDZ basis sets, and between CCSD(T) and MP2 correlation energies for the ISOL18 set.

loose PNO thresholds. Applying two-point extrapolation then yields:

$$E_X \approx E_X(T_3) + fF(E_Y(T_4) - E_Y(T_3)), \tag{5.17}$$

$$F = \frac{T_3^{1/2}}{T_3^{1/2} - T_4^{1/2}}, \quad f = \frac{E_X(T_2) - E_X(T_1)}{E_Y(T_2) - E_Y(T_1)}. \tag{5.18}$$

Here, the PNO truncation thresholds should satisfy $T_1 > T_2 \geq T_3 > T_4$. If $T_2 = T_3$, a total of five calculations are required.

Testing the scaling approach

To assess the accuracy of Equation (5.17), we apply it to CCSD(T)/cc-pVTZ isomerization energies in the ISOL18 set. Table 5.6 reports deviations from the CPS limit for different choices of method Y, using the notation $(5, 6, 7)$ to denote $T_1 = 10^{-5}$, $T_2 = T_3 = 10^{-6}$, $T_4 = 10^{-7}$, etc. The CCSD(T)/cc-pVTZ results are provided for reference.

A comparison between CCSD(T)/cc-pVTZ and CCSD(T)/cc-pVDZ demonstrates similar accuracy. Thus, to achieve (7,8)-quality PNO-CCSD(T)/cc-pVTZ results, one can use $T = 10^{-6}$ and 10^{-7} with cc-pVTZ, supplemented by $T = 10^{-6}$, 10^{-7}, and 10^{-8} calculations using the

Y	Error	$(5,6,7)$	$(6,7,8)$	$(7,8,9)$
CCSD(T)/cc-pVTZ	AV	−0.12	−0.03	0.00
	RMS	0.31	0.11	0.04
	MAX	−0.92	−0.42	0.09
CCSD(T)/cc-pVDZ	AV	−0.09	−0.00	−0.02
	RMS	0.32	0.13	0.07
	MAX	−0.86	−0.35	−0.24
MP2/cc-pVTZ	AV	−0.19	−0.11	−0.01
	RMS	0.83	0.23	0.14
	MAX	2.31	−0.71	−0.42
MP2/cc-pVDZ	AV	−0.14	−0.11	0.01
	RMS	0.79	0.30	0.12
	MAX	1.76	−0.70	−0.43

Table 5.6: PNO truncation error statistics for CCSD(T)/cc-pVTZ isomerisation energies of the ISOL18 set using Eq 5.17.

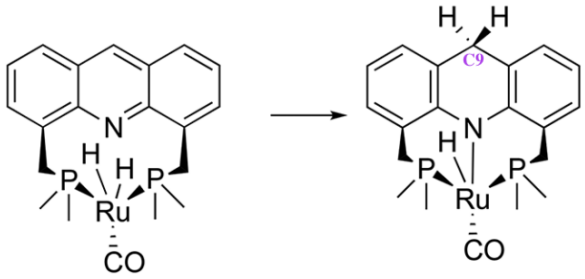


Figure 5.10: Schematic of the reactant and product species of reaction 13 in the MOBH35 set, highlighting the C9 position on the ligand involved in hydride transfer. Figure taken from Ref. 3.

smaller cc-pVDZ basis, avoiding costly tight-threshold cc-pVTZ computations.

On the other hand, using MP2 as method Y introduces larger uncertainties due to increased variation in $f(T)$. However, applying $(6,7,8)$ with MP2 still offers a slight improvement over $(6,7)$ without an MP2 correction. Simultaneously reducing both method and basis set leads to excessive errors and is not recommended.

Case study: reaction 13 in MOBH35

We now compare the accuracy and timings of various approaches for reaction 13 of the MOBH35 set, which shows slow PNO convergence. The reaction involves a ruthenium (Ru) acridine-based pincer complex that heterolytically cleaves activated molecular hydrogen to form a dearomatised complex. This reaction exhibits a rare instance of long-range metal-ligand cooperation. As shown in 5.10, it involves hydride transfer over a relatively long spatial range–

Scheme	Forward	Reverse	Minutes
6	5.5	3.1	92
6+Δ	3.7	2.2	93
(5,6)	3.7	1.9	144
7	2.5	1.4	184
7+Δ	1.8	1.1	185
(5,6,7)	1.0	1.0	213
(6,7)	1.1	0.6	265
8	0.9	0.5	554
8+Δ	0.6	0.4	555
(6,7,8)	0.1	0.3	398
(7,8)	0.1	0.1	726

Table 5.7: Timings and PNO truncation errors in kcal/mol of CCSD(T)/def2-TZVPP barrier heights for MOBH35 reaction 13 using PNO thresholds 10^{-6}-10^{-8} and with extrapolation and correction schemes.

from Ru to the C9 position on the pincer ligand,[185], which is distinct from the more commonly found metal-ligand cooperation scenarios where the metal and reactive ligand site are adjacent to each other. Moreover, the standard pincer ligands are rigid five-membered rings. This reaction involves a flexible six-membered ring of the acridine-based pincer, which facilitates the long-range interaction, but this flexibility also introduces conformational complexity. Modelling such weak interactions requires a very accurate treatment of non-covalent effects (e.g. van der Waals, dispersion). Non-covalent interactions are sensitive to the long-range tails of the electron density and therefore require relatively large PNO domains to be accurately described, resulting in slow convergence with respect to the PNO threshold.[186]

Table 5.7 presents PNO truncation errors for reaction 13. The total wall times for estimating the canonical energy of the reactant are also reported. Various error-reduction schemes for PNO-CCSD(T)/def2-TZVPP are compared: no extrapolation, adding an MP2 correction Δ as suggested by Kubas,[184] scaled extrapolation using def2-SVP, and conventional two-point extrapolation.

All reported wall times include the Hartree-Fock (HF) step, which took 12 minutes with density fitting. While the MP2 correction $\Delta = E_{\text{MP2}} - E_{\text{PNO-MP2}}$ reduces PNO truncation error for loose thresholds with minimal cost, it is less effective for tight thresholds. The most cost-effective method to recover the canonical result is the (6,7,8) scaled extrapolation scheme, avoiding the computational expense of performing PNO-CCSD(T)/def2-TZVPP calculations at the tightest $T = 10^{-8}$ threshold.

5.2.4 Benchmark Data

MOBH35

Our CPS extrapolation approach enables reliable estimation of canonical CCSD(T) energies for large systems with extensive basis sets using PNO methods. This allows extrapolation to the CBS limit without being constrained by PNO truncation errors. Table 5.8 presents our best estimates of the canonical CCSD(T) barrier heights for the complete MOBH35 set. Our def2-SVP results closely align with previous reports, and we provide, for the first time, def2-QZVPP values for the entire dataset, including reactions 17-20, which were omitted in the work of Semidalas and Martin.

To determine the CPS limit for CCSD(T)/def2-SVP, we apply an (8,9) extrapolation of PNO-CCSD(T) energies based on the $T^{1/2}$ convergence model, which has an RMS deviation of less than 0.1 kcal/mol from the canonical limit. We performed PNO-CCSD(T)/def2-SVP calculations with $T = 10^{-9}$ for the entire dataset. However, due to disk space limitations, $T = 10^{-9}$ was not feasible for def2-TZVPP, though we successfully used $T = 10^{-8}$ for all molecules. To estimate the canonical CCSD(T)/def2-TZVPP limit, we employed (7,8,9) extrapolation:

$$E_T \approx E_T(10^{-8}) + fF(E_S(10^{-9}) - E_S(10^{-8})) \tag{5.19}$$

$$F = \frac{10^{1/2}}{10^{1/2} - 1}, \quad f = \frac{E_T(10^{-8}) - E_T(10^{-7})}{E_S(10^{-8}) - E_S(10^{-7})} \tag{5.20}$$

For def2-QZVPP, PNO-CCSD(T) calculations were feasible for all but the largest molecules. In these cases, we applied (7,8,9) extrapolation using def2-SVP values. For the largest systems, we used (6,7,8) extrapolation with def2-TZVPP:

$$E_Q \approx E_Q(10^{-7}) + fF(E_T(10^{-8}) - E_T(10^{-7})) \tag{5.21}$$

$$F = \frac{10^{1/2}}{10^{1/2} - 1}, \quad f = \frac{E_Q(10^{-7}) - E_Q(10^{-6})}{E_T(10^{-7}) - E_T(10^{-6})} \tag{5.22}$$

Our def2-SVP results show slight deviations from the subset of canonical values reported by Semidalas and Martin. In contrast to ours, their HF calculations employed density fitting. This difference in HF energies and the subsequent correlation energy variations lead to an average deviation of 0.1 kcal/mol. For reactions 5, 6, 12, 24, 25, 26, 31, 32, and 35, deviations range

between 0.1-0.3 kcal/mol, which is within typical variations.[187]

Additionally, Table 5.8 presents (8,9) extrapolated CPS values rather than canonical values. While these estimates are within 0.1 kcal/mol of the canonical barrier heights for the MOBH16 subset, this subset does not include reactions 8, 9, and 13, which exhibit stronger correlation effects and slower PNO threshold convergence. As a result, residual CPS errors of up to 0.4 kcal/mol may persist for these reactions. A conservative error estimate of 0.2 kcal/mol should be assigned to the PNO-based canonical values, except for reactions 8, 9, and 13, where errors may reach 0.5 kcal/mol.

The key distinction between our best CBS estimate and that of Semidalas and Martin is our use of (TQ) extrapolation for both CCSD and (T) correlation energies. In contrast, Semidalas and Martin did not compute the (T) contribution with the def2-QZVPP basis, opting instead for (ST) extrapolation. Nonetheless, our barrier heights differ from theirs by less than 0.5 kcal/mol for all reactions except for 8, 9, and 13. For these strongly correlated systems, our values differ by up to 2.5 kcal/mol, lying between those of Semidalas and Martin[161] and the original results reported by Iron and Janes.[166]

ISOL24

Energies close to the CBS limit for the ISOL24 set have been computed by Werner and Hansen using the PNO-LCCSD(T)-F12b method in Molpro with a modified aug-cc-pVQZ basis set[167]. Table 5.9 compares their isomerisation energies with our results obtained via CBS extrapolation of CPS-extrapolated PNO-CCSD(T) energies.

We performed PNO-CCSD(T) calculations with $T = 10^{-9}$ for the cc-pVDZ basis and $T = 10^{-8}$ for the cc-pVTZ and cc-pVQZ basis sets across all molecules. Our best estimate of canonical CCSD(T) energies follows an (8,9) extrapolation for cc-pVDZ and a (7,8,9) extrapolation using cc-pVDZ as Y for the cc-pVTZ and cc-pVQZ basis sets. Our most accurate CBS values are derived using (TQ) extrapolation. The isomerisation energies obtained from (TQ) and F12 methods generally agree within 0.5 kcal/mol, except for isomer pairs 4 and 22, where the deviation reaches 0.9 kcal/mol. This slight discrepancy is marginally larger than what is typically expected from canonical theory. Nonetheless, these results reinforce the reliability of PNO-CCSD(T) theory in CBS extrapolation, provided that PNO truncation errors are effectively

rxn	Forward					Reverse				
	SVP	TZVPP	(ST)	QZVPP	(TQ)	SVP	TZVPP	(ST)	QZVPP	(TQ)
1	27.06	26.67	26.43	26.26	25.94	14.02	13.91	13.87	14.45	14.75
2	5.62	5.91	5.62	5.84	5.77	25.10	22.25	21.87	22.34	22.43
3	0.95	1.03	0.90	1.01	1.01	27.07	26.14	26.80	27.09	27.69
4	2.35	1.54	0.98	1.45	1.38	8.60	7.87	8.34	8.43	8.82
5	4.43	4.69	4.28	4.94	5.03	22.09	22.73	22.60	22.64	22.68
6	13.48	15.60	15.81	15.84	15.98	13.46	14.82	14.32	15.02	14.98
7	26.62	27.70	28.01	27.72	27.80	18.26	18.91	18.29	18.91	18.85
8[a]	37.28	35.65	35.69	36.01	35.70	32.77	32.54	32.47	33.46	33.70
9[a]	28.97	28.08	28.50	29.42	30.01	14.90	12.07	10.66	11.09	10.82
10	−3.52	−3.82	−3.79	−4.16	−4.43	9.59	8.95	7.41	8.03	7.56
11[a]	29.89	30.05	29.91	29.59	29.39	84.13	83.17	83.10	82.95	82.54
12	5.68	5.37	5.46	5.31	5.28	36.95	37.38	38.33	37.17	37.19
13	18.85	20.69	21.37	20.88	21.24	48.37	48.59	48.89	48.52	48.42
14	10.20	10.26	10.26	10.31	10.35	13.33	14.43	13.95	14.89	14.99
15	23.84	20.77	19.77	20.44	20.14	74.62	74.91	74.55	75.96	76.51
16	37.24	35.09	34.50	35.04	34.89	55.45	53.61	53.84	53.93	54.37
17[a]	24.22	22.84	24.20	21.28	20.54	29.94	28.35	27.54	30.94	31.87
18[a]	25.53	26.12	27.79	24.94	24.44	27.93	28.35	27.83	31.70	33.09
19[a]	11.05	11.55	13.09	10.96	10.58	30.36	28.80	27.98	31.69	32.85
20[a]	7.60	10.49	12.28	10.29	10.06	28.15	28.71	28.20	32.18	33.63
21	11.06	8.14	7.87	8.44	8.70	11.06	8.15	7.88	8.44	8.69
22	14.90	14.42	13.64	14.39	14.37	30.83	27.25	26.42	27.66	28.00
23	29.40	29.98	28.81	29.90	29.85	20.82	20.45	20.12	20.64	20.79
24[a]	1.08	2.44	2.35	2.71	2.85	18.61	17.03	17.34	16.61	16.54
25[a]	1.52	2.78	2.60	3.11	3.23	14.58	12.90	13.08	12.91	13.08
26	21.79	25.07	25.94	25.25	25.39	−0.07	0.13	0.22	0.14	0.17
27	16.11	14.09	14.00	13.87	13.84	1.29	1.88	1.75	2.20	2.42
28	32.00	30.63	30.50	30.21	29.86	16.85	15.94	15.41	15.84	15.81
29	15.76	15.30	15.05	14.91	14.69	33.87	32.02	30.74	31.35	30.88
30	10.94	10.07	9.94	9.81	9.64	19.89	17.10	16.29	17.19	17.15
31	2.37	3.41	4.00	3.26	3.07	12.31	13.35	13.03	13.01	12.79
32	23.56	20.43	20.31	20.01	19.87	58.31	62.06	62.67	63.31	64.08
33	2.76	1.21	0.70	1.13	0.99	10.00	8.24	8.21	8.10	8.02
34	28.85	29.82	29.56	29.11	28.66	4.38	3.54	3.49	3.24	2.99
35	15.00	16.68	16.51	17.54	17.99	−3.74	−2.42	−2.24	−2.08	−1.86

Table 5.8: Best estimates for CCSD(T) barrier heights for the MOBH35 test set in kcal/mol
[a] def2-QZVPP values are computed using the (6,7,8) threshold combination with *Y*=def2-TZVPP, rather than using the (7,8,9) threshold combination with *Y*=def2-SVP.

managed.

Isomer pair 22 involves numerous rotatable bonds and functional groups. The reference isomerisation energy, reported by Werner and Hansen (F12), is only 1.08 kcal/mol, indicating that even small numerical or methodological inaccuracies (e.g., in dispersion treatment, BSSE, or PNO truncation) can flip the predicted stability ordering. While both isomer pairs 12 and 22 exhibit small isomerisation energies near zero, isomer pair 22 shows a pronounced basis set dependence, as also noted by Werner and Hansen,[167] who attribute this to significant intramolecular BSSE.

The increased deviations observed for isomer pairs 4 and 22 in our CBS estimates, compared to F12, are primarily due to the absence of diffuse functions in the chosen basis set rather than PNO-related errors. Table 5.10 presents the results of equivalent calculations performed with aug-cc-pVXZ' (APVXZ') basis sets, where the prime notation signifies the exclusion of diffuse functions from hydrogen atoms. For these computations, the multilevel approximation was applied.

Our combined CPS and CBS extrapolation strategy remains equally effective when incorporating diffuse functions and utilising the multilevel approximation. Notably, the inclusion of diffuse functions leads to CBS results that align much more closely with the F12 benchmarks.

5.3 Conclusions

In PNO-based local correlation approximations, basis set errors arise from a combination of PNO truncation effects and intrinsic atomic basis set limitations. Our benchmark study demonstrates that tightening the PNO threshold yields improvements comparable to increasing the atomic basis set. For instance, at the MP2 level, enhancing the basis from TZ to QZ with a PNO threshold of 10^{-6} offers a similar gain as retaining a TZ basis while tightening the threshold to 10^{-7}. Consequently, the accuracy of conventional X^{-3} basis set extrapolation within PNO local correlation methods is highly sensitive to the chosen PNO threshold. While a threshold of $T = 10^{-6}$ may be acceptable for a TZ basis, at least $T = 10^{-7}$ is required for QZ calculations to be meaningful. Notably, a (TQ) extrapolation with $T = 10^{-6}$ often introduces larger basis set errors than a direct QZ computation at $T = 10^{-7}$. Additionally, employing a loose threshold in combination with extrapolation can lead to false convergence when comparing TZ, QZ, and

iso	DZ	TZ	(DT)	QZ	(TQ)	F12[a]
1	67.35	70.22	70.71	71.24	71.55	71.53
2	40.78	39.14	39.90	38.59	38.68	38.13
3	4.29	8.76	9.70	9.67	10.21	10.29
4	75.61	71.55	73.90	70.17	69.89	69.03
5	34.76	32.51	32.92	32.65	33.02	32.85
6	18.62	22.41	23.44	23.47	24.07	24.14
7	18.90	17.92	18.46	17.83	17.90	17.72
8	23.04	24.00	23.13	24.24	24.01	23.93
9	22.77	21.68	21.63	21.36	21.13	21.10
10	6.07	6.14	6.37	6.43	6.47	6.26
11	35.66	35.45	35.19	36.18	36.65	36.80
12	0.68	0.43	0.43	0.42	0.48	0.42
13	29.00	32.25	32.84	33.03	33.29	33.20
14	4.26	4.68	5.30	4.97	5.06	4.92
15	10.82	4.37	3.56	4.03	4.15	4.07
16	20.68	22.69	23.61	22.76	23.04	22.62
17	9.51	9.19	9.57	9.29	9.45	9.59
18	27.06	24.78	24.60	24.19	23.93	23.77
19	18.77	18.41	18.06	18.41	18.37	18.28
20	6.18	5.37	4.98	5.18	4.95	5.13
21	11.17	11.00	11.51	11.29	11.60	11.38
22[b]	−3.59	−0.98	−1.25	0.09	0.18	1.08
23	24.04	23.93	24.31	23.72	23.75	23.66
24	16.32	15.58	15.49	15.34	15.25	15.25

Table 5.9: Best estimates for CCSD(T) isomerisation energies for the ISOL24 test set in kcal/mol.
[a] PNO-LCCSD(T)-F12b/APVQZ' values taken from Ref. 167.
[b] product and educt reversed to maintain positive sign.

iso	DZ	TZ	(DT)	QZ	(TQ)	F12[a]
4	85.55	74.45	74.19	70.94	68.63	69.03
22[b]	−5.94	−1.96	−1.88	0.00	0.97	1.08

Table 5.10: CPS- and CBS-Extrapolated CCSD(T) isomerisation energies in kcal/mol of isomer pairs 4 and 22 in ISOL24 set.
[a] PNO-LCCSD(T)-F12b/APVQZ' values taken from Ref. 167.
[b] product and educt reversed to maintain positive sign.

(TQ) values, significantly underestimating the true basis set error.

To mitigate PNO truncation errors, we explored a three-point extrapolation scheme that leverages the smooth convergence of PNO energies toward the canonical limit as the threshold is tightened–an approach also employed in Frozen Natural Orbital methods. Our findings confirm that this T^{α} extrapolation effectively reduces truncation errors, enabling accurate approximations of canonical MP2 energies without requiring prohibitively tight PNO thresholds.

Beyond standard basis set extrapolation, we introduce an alternative approach based on the N_{ij}^{-1} decay of basis set errors with the number of PNOs used to correlate electron pairs. This method is particularly cost-effective as it avoids the additional HF calculations and integral transformation steps required when employing two basis sets. Moreover, it is broadly applicable, as it does not rely on a pre-optimised hierarchy of basis sets. We show that N_{ij}^{-1} extrapolation at the PNO-MP2/TZ level using $T = 10^{-5}$ and 10^{-6} yields accuracy comparable to conventional (DT) X^{-3} extrapolation of PNO-MP2+Δ energies using $T = 10^{-7}$, while being significantly more efficient. However, when aiming for highly converged basis set limit energies, a dual T^{α}, X^{-3} extrapolation approach remains the most reliable strategy.

Extending these insights to coupled-cluster methods, domain-based PNO-CCSD(T) provides an efficient alternative to canonical CCSD(T), enabling high-accuracy calculations for large molecular systems. However, achieving the 'gold standard' accuracy–where reaction enthalpies are predicted within 1 kcal/mol of experiment–requires rigorous control over both basis set and PNO truncation errors. Our analysis confirms that, similar to canonical methods, CCSD(T) correlation energies exhibit a basis set convergence behaviour of the form $E_X = E_\infty + CX^{-3}$. Additionally, the PNO truncation error follows the trend $E_X(T) = E_X + A_X T^{1/2}$, leading to a combined extrapolation model: $E_X(T) = E_\infty + A_X T^{1/2} + CX^{-3}$. The prefactor A_X depends on the basis set size, increases with the number of correlated electrons, and is more pronounced in systems with strong correlation effects.

For obtaining accurate CBS CCSD(T) energies using PNO methods, the most reliable approach is to first eliminate the PNO truncation error via CPS extrapolation, yielding near-canonical energies E_X and E_{X+1}, followed by standard two-point CBS extrapolation. This CPS scheme closely parallels basis set extrapolation and requires calculations at two PNO thresholds, typically $10T$ and T. Our findings indicate that for systems with moderate static correlation, even

tight PNO thresholds of $T = 10^{-7}$ are insufficient to ensure PNO truncation errors below 1 kcal/mol. However, extrapolating with $T = 10^{-7}$ and $T = 10^{-8}$ consistently produces reliable results across benchmark data sets such as ISOL24 and MOBH35.

Regarding basis set truncation, previous studies confirm that CCSD(T) calculations with double-ζ basis sets exhibit errors comparable to those of density functional approximations, underscoring that (TQ) extrapolation is the minimal requirement for achieving 'gold standard' accuracy. However, the combination of tight PNO thresholds and large basis sets imposes a substantial computational burden, particularly in terms of I/O demands for storing pair-specific integrals. We demonstrate that the prefactor A_X for a large basis can be reliably estimated using information from smaller basis set calculations, thereby reducing the cost of high-accuracy extrapolation with minimal loss of precision.

Our recommended CPS extrapolation approach to obtain CCSD(T) energies in a basis set of cardinal number X is:

$$E_X \approx E_X(10^{-7}) + fF(E_{X-1}(10^{-8}) - E_{X-1}(10^{-7})), \tag{5.23}$$

$$F = \frac{10^{1/2}}{10^{1/2} - 1}, \quad f = \frac{E_X(10^{-7}) - E_X(10^{-6})}{E_{X-1}(10^{-7}) - E_{X-1}(10^{-6})}. \tag{5.24}$$

This approach offers a practical and accurate means of obtaining highly converged CBS CCSD(T) energies while minimising computational overhead.

In summary, our work establishes a framework for systematically reducing basis set and PNO truncation errors in PNO-MP2 and PNO-CCSD(T) calculations. By leveraging combined CPS and CBS extrapolation techniques, we enable reliable, cost-effective extrapolation strategies that balance computational efficiency with high-accuracy correlation energy predictions.

6| Summary and Outlook

We have implemented a periodic PNO-MP2 method for electronic structure calculations of crystalline systems using atom-centred Gaussian basis sets. To the best of our knowledge, this is the first application of PNOs within the framework of BvK boundary conditions.

A key methodological advancement achieved in this work is the development of a practical scheme for generating localised Wannier orbitals by applying a Cholesky decomposition to the Γ-point Bloch orbitals and propagating their locality across **k**-points. This ensures a smooth **k**-dependence of Bloch orbitals and results in well-localised Wannier functions upon Fourier transformation. The effectiveness of this localisation scheme was verified for both 1D and 3D systems using a Pipek–Mezey metric based on IAOs [139] and corroborated by visual inspection.

The BvK supercell appraoch for a truly periodic PNO-MP2 treatment is presented through this work. In this framework, all the relevant entities: Wannier orbitals, PAOs, OSVs, PNOs, and ERIs remain translationally invariant. This allows their translational symmetry to be exploited, so that all necessary computations can be restricted to the reference unit cell. This facilitates an overall asymptotic scaling of $O(N)$ with respect to the size of the unit cell N if the prefactor due to lattice sums in the evaluation of ERIs and the density fitting domain sizes are sufficiently small. Thus, the scaling of the method remains equivalent to that of molecular PNO-MP2, since the lattice summations are performed efficiently.

We performed proof-of-concept calculations to demonstrate the method's potential. The correlation energies for the 1D polymer, Polyethylene, and 2D CO and Xe lattices closely matched the benchmarks extracted from hierarchical molecular PNO-MP2 calculations, even for relatively coarse **k**-point meshes. Furthermore, the periodic PNO-MP2 method was shown to capture dispersion-driven effects in a 1D BN nanoscroll at a fixed degree of rolling, inverting the predictions of HF and DFT methods for the rolling of BN nanosheet from unfavourable to favourable. This result highlights the ability of PNO-MP2 to describe weak long-range interactions, which was already achieved using intermediate PNO thresholds.

As highlighted in Chapter 1, DFT is still the workhorse for material simulations, and correlation calculations of materials using wavefunction-based methods have been largely limited to Γ-point simulations or calculations with coarse Brillouin zone sampling. Therefore, large-

scale simulations of realistic materials have remained out of the reach of wavefunction-based methods. By exploiting the short-range character of dynamical correlation, the local correlation approach can provide significant reductions in the scaling of these methods and extend their scope to periodic systems with larger unit cells. This was already demonstrated by Usvyat *et al.* for some non-conducting systems using OSVs at the MP2 level[81]. However, OSV pair domains are formed as a union of orbital pair domains, regardless of the distance between the two orbitals. Therefore, the sizes of OSV pair domains are significantly larger than necessary for distant pairs, which can be a bottleneck. This bottleneck is lifted in the case of PNOs as the domains are defined pairwise, so that they are only as large as necessary. Because of this, PNOs provide the most compact representation of the virtual space. Therefore, the periodic PNO-MP2 method has the potential to access even larger unit cell sizes than is possible to date.

This work lays the foundation for the periodic PNO-MP2 method. To realise the full potential of the method, it is important to overcome the issue of convergence of lattice sums due to the accumulation of dipoles on the surface of the supercell. An implementation of a dipole correction scheme to mitigate this issue is already ongoing. This, along with the implementation of the CFMM for improved efficiency in the evaluation of ERIs, will make this method a highly efficient and useful tool for systems where MP2 can provide accurate results.

In the future, the framework to handle periodic systems developed in this work can be generalised to coupled-cluster methods, which opens the door to highly accurate, large-scale simulations of periodic systems.

Additionally, our work on extrapolation techniques for molecular PNO-based correlation methods provides valuable insights that may guide future extensions of these techniques to our periodic PNO-MP2 method. Our work shows that basis set and PNO truncation errors are strongly coupled, and that careful control of the PNO threshold is critical for accurate basis set extrapolation. Techniques such as T^{α} extrapolation and extrapolation based on the inverse number of PNOs (N_{ij}^{-1}) offer cost-effective alternatives to conventional X^{-3} basis set extrapolation, reducing the need for prohibitively tight thresholds or large basis sets. These methods have been shown to recover near-canonical correlation energies efficiently and reliably. Furthermore, a combined CPS and CBS extrapolation scheme enables highly accurate CCSD(T) energies with minimal computational overhead. Extending such extrapolation strategies to a periodic

framework could significantly enhance the accuracy and efficiency of periodic PNO-MP2 and PNO-CCSD(T) methods, especially for systems where tight thresholds or large basis sets are computationally demanding.

Bibliography

[1] K. Sorathia and D. P. Tew, J. Chem. Phys. **153**, 174112 (2020).

[2] K. Sorathia, D. Frantzov, and D. P. Tew, Journal of Chemical Theory and Computation **20**, 2740 (2024).

[3] M. A. Iron and T. Janes, J. Phys. Chem. A **123**, 3761 (2019).

[4] E. R. Johnson, R. A. Wolkow, and G. A. Dilabio, Chem. Phys. Lett. **394**, 334 (2004).

[5] K. R. Bryenton, A. A. Adeleke, S. G. Dale, and E. R. Johnson, Wiley Interdiscip. Rev. Comput. Mol. Sci. (2022).

[6] A. D. Boese, ChemPhysChem **16**, 978 (2015).

[7] M. Bursch, E. Caldeweyher, A. Hansen, H. Neugebauer, S. Ehlert, and S. Grimme, Acc. Chem. Res. **52**, 258 (2019).

[8] S. Andersson and M. Grüning, J. Phys. Chem. A **108**, 7621 (2004).

[9] M. Grüning, O. V. Gritsenko, and E. J. Baerends, J. Phys. Chem. A **108**, 4459 (2004).

[10] J. P. Perdew, Int. J. Quantum Chem. **28**, 497 (1985).

[11] Y. Zhao, B. J. Lynch, and D. G. Truhlar, The Journal of Physical Chemistry A **108**, 2715 (2004).

[12] B. J. Lynch and D. G. Truhlar, J. Phys. Chem. A **105**, 2936 (2001).

[13] X. Xu, I. M. Alecu, and D. G. Truhlar, J. Chem. Theory Comput. **7**, 1667 (2011).

[14] X. Zheng, A. J. Cohen, P. Mori-Sánchez, X. Hu, and W. Yang, Phys. Rev. Lett. **107**, 026403 (2011).

[15] J. M. Crowley, J. Tahir-Kheli, and W. A. Goddard, J. Phys. Chem. Lett **7**, 51 (2016).

[16] Z. Feng-Hui, H. Zhan-Wen, L. Li, M. Marsman, J. Paier, A. Stroppa, and G. Kresse, J. Phys. Condens. Matter **20**, 64201 (2008).

[17] J. P. Perdew, K. Schmidt, J. Chem Phys, and J. Mazer, AIP Conf. Proc. **577**, 1 (2001).

[18] N. Mardirossian and M. Head-Gordon, Mol. Phys. **115**, 2315 (2017).

[19] V. R. Saunders, *Ab initio Hartree–Fock calculations for periodic systems*, Tech. Rep. (1984).

[20] S. Tosoni, C. Tuma, J. Sauer, B. Civalleri, and P. Ugliengo, The Journal of Chemical Physics **127**, 154102 (2007).

[21] K. Adhikari, A. Chakrabarty, O. Bouhali, N. Mousseau, C. S. Becquart, and F. El-Mellouhi, Journal of Computational Science **29**, 163 (2018).

[22] C. A. Rozzi, D. Varsano, A. Marini, E. K. U. Gross, and A. Rubio, Phys. Rev. B **73**, 205119 (2006).

[23] V. Blum, R. Gehrke, F. Hanke, P. Havu, V. Havu, X. Ren, K. Reuter, and M. Scheffler, Computer Physics Communications **180**, 2175 (2009).

[24] O. K. Andersen, Phys. Rev. B **12**, 3060 (1975).

[25] S. Y. Savrasov, Phys. Rev. B **54**, 16470 (1996).

[26] T. A. Arias, Rev. Mod. Phys. **71**, 267 (1999).

[27] R. E. Watson, J. W. Davenport, and M. Weinert, Phys. Rev. B **35**, 508 (1987).

[28] E. S. Kadantsev and T. Ziegler, The Journal of Physical Chemistry A **113**, 1327 (2009).

[29] G. Ulian, S. Tosoni, and G. Valdrè, The Journal of Chemical Physics **139**, 204101 (2013).

[30] G. H. Booth, T. Tsatsoulis, G. K.-L. Chan, and A. Grüneis, The Journal of Chemical Physics **145**, 084111 (2016).

[31] S. Boys and F. Bernardi, Molecular Physics **19**, 553 (1970).

[32] M. Marsman, A. Grüneis, J. Paier, et Al, and G. Kresse, J. Chem. Phys **130**, 184103 (2009).

[33] J. J. Shepherd, A. Grüneis, G. H. Booth, G. Kresse, and A. Alavi, Phys. Rev. B **86**, 035111 (2012).

[34] A. Grüneis, M. Marsman, and G. Kresse, The Journal of Chemical Physics **133**, 074107 (2010).

[35] T. Schäfer, B. Ramberger, and G. Kresse, The Journal of Chemical Physics **146**, 104101 (2017).

[36] K. Liao and A. Grüneis, The Journal of Chemical Physics **145**, 141102 (2016).

[37] J. McClain, Q. Sun, G. K.-L. Chan, and T. C. Berkelbach, Journal of Chemical Theory and Computation **13**, 1209 (2017).

[38] Y.-y. Ohnishi and S. Hirata, The Journal of Chemical Physics **135**, 094108 (2011).

[39] A. Grüneis, G. H. Booth, M. Marsman, J. Spencer, A. Alavi, and G. Kresse, Journal of Chemical Theory and Computation **7**, 2780 (2011).

[40] G. Lippert, J. Hutter, and M. Parrinello, Molecular Physics **92**, 477 (1997).

[41] M. Del Ben, J. Hutter, and J. VandeVondele, Journal of Chemical Theory and Computation **8**, 4177 (2012).

[42] H. Stoll, The Journal of Chemical Physics **97**, 8449 (1992).

[43] H. Stoll, Chemical Physics Letters **191**, 548 (1992).

[44] C. Müller, D. Usvyat, and H. Stoll, Phys. Rev. B **83**, 245136 (2011).

[45] B. Paulus, P. Fulde, and H. Stoll, Phys. Rev. B **51**, 10572 (1995).

[46] M. Albrecht, B. Paulus, and H. Stoll, Phys. Rev. B **56**, 7339 (1997).

[47] K. Doll and H. Stoll, Phys. Rev. B **57**, 4327 (1998).

[48] K. Doll, M. Dolg, P. Fulde, and H. Stoll, Phys. Rev. B **55**, 10282 (1997).

[49] K. Rościszewski, K. Doll, B. Paulus, P. Fulde, and H. Stoll, Phys. Rev. B **57**, 14667 (1998).

[50] S. Li, J. Ma, and Y. Jiang, Journal of Computational Chemistry **23**, 237 (2002).

[51] Z. N. Wei Li and S. Li, Molecular Physics **114**, 1447 (2016).

[52] Z. Ni, Y. Guo, F. Neese, W. Li, and S. Li, Journal of Chemical Theory and Computation **17**, 756 (2021).

[53] W. Förner, J. Ladik, P. Otto, and J. Čížek, Chemical Physics **97**, 251 (1985).

[54] Y. Wang, Z. Ni, W. Li, and S. Li, Journal of Chemical Theory and Computation **15**, 2933 (2019).

[55] Y. Wang, Z. Ni, F. Neese, W. Li, Y. Guo, and S. Li, Journal of Chemical Theory and Computation **18**, 6510 (2022).

[56] F. R. Manby, D. Alfè, and M. J. Gillan, Phys. Chem. Chem. Phys. **8**, 5178 (2006).

[57] E. E. Dahlke and D. G. Truhlar, Journal of Chemical Theory and Computation **3**, 46 (2007).

[58] C. Müller and B. Paulus, Phys. Chem. Chem. Phys. **14**, 7605 (2012).

[59] Z.-H. Cui, T. Zhu, and G. K.-L. Chan, Journal of Chemical Theory and Computation **16**, 119 (2020).

[60] M. Nusspickel and G. H. Booth, Phys. Rev. X **12**, 011046 (2022).

[61] A. Grüneis, M. Marsman, and G. Kresse, J. Chem. Phys **133**, 74107 (2010).

[62] Y. H. Liang, H.-Z. Ye, and T. C. Berkelbach, The Journal of Physical Chemistry Letters **14**, 10435 (2023).

[63] S. J. Bintrim, T. C. Berkelbach, and H.-Z. Ye, Journal of Chemical Theory and Computation **18**, 5374 (2022).

[64] X. Wang and T. C. Berkelbach, Journal of Chemical Theory and Computation **16**, 3095 (2020).

[65] V. A. Neufeld and T. C. Berkelbach, Phys. Rev. Lett. **131**, 186402 (2023).

[66] E. A. Vo, X. Wang, and T. C. Berkelbach, The Journal of Chemical Physics **160**, 044106 (2024).

[67] T. Gruber, K. Liao, T. Tsatsoulis, F. Hummel, and A. Grüneis, Phys. Rev. X **8**, 021043 (2018).

[68] T. N. Mihm, T. Schäfer, S. K. Ramadugu, L. Weiler, A. Grüneis, and J. J. Shepherd, Nature Computational Science **1**, 801 (2021).

[69] V. A. Neufeld, H.-Z. Ye, and T. C. Berkelbach, The Journal of Physical Chemistry Letters **13**, 7497 (2022).

[70] H.-Z. Ye and T. C. Berkelbach, Journal of Chemical Theory and Computation **20**, 8948 (2024).

[71] P. Pulay, Chemical Physics Letters **100**, 151 (1983).

[72] P. Pulay, Chem. Phys. Lett. **100**, 151 (1983).

[73] H.-J. Werner, F. R. Manby, and P. J. Knowles, The Journal of Chemical Physics **118**, 8149 (2003).

[74] H.-J. Werner, G. Knizia, C. Krause, M. Schwilk, and M. Dornbach, Journal of Chemical Theory and Computation **11**, 484 (2015).

[75] C. Riplinger, P. Pinski, U. Becker, E. F. Valeev, and F. Neese, J. Chem. Phys. **144**, 024109 (2016).

[76] C. Riplinger, B. Sandhoefer, A. Hansen, and F. Neese, J. Chem. Phys. **139**, 134101 (2013).

[77] P. Pinski, C. Riplinger, E. F. Valeev, and F. Neese, J. Chem. Phys. **143**, 034108 (2015).

[78] Q. Ma and H.-J. Werner, (2015).

[79] C. Pisani, M. Schütz, S. Casassa, D. Usvyat, L. Maschio, M. Lorenz, and A. Erba, Phys. Chem. Chem. Phys. **14**, 7615 (2012).

[80] D. Usvyat, B. Civalleri, L. Maschio, R. Dovesi, C. Pisani, and M. Schütz, The Journal of Chemical Physics **134**, 214105 (2011).

[81] D. Usvyat, L. Maschio, and M. Schütz, The Journal of Chemical Physics **143**, 102805 (2015).

[82] L. Maschio, D. Usvyat, M. Schütz, and B. Civalleri, The Journal of Chemical Physics **132**, 134706 (2010).

[83] P.-O. Löwdin, Phys. Rev. **97**, 1474 (1955).

[84] T. Helgaker, P. Jørgensen, and J. Olsen, "Perturbation theory," in *Molecular Electronic-Structure Theory* (John Wiley & Sons, Ltd, 2000) Chap. 14, pp. 724–816.

[85] D. Cremer and Z. He, The Journal of Physical Chemistry **100**, 6173 (1996).

[86] D. Cremer, WIREs Computational Molecular Science **1**, 509 (2011).

[87] M. Head-Gordon, J. A. Pople, and M. J. Frisch, Chemical Physics Letters **153**, 503 (1988).

[88] S. Sæbø and J. Almlöf, Chemical Physics Letters **154**, 83 (1989).

[89] F. Haase and R. Ahlrichs, Journal of Computational Chemistry **14**, 907 (1993).

[90] R. Jurgens-Lutovsky and J. Almlöf, Chemical Physics Letters **178**, 451 (1991).

[91] T. J. Martinez and E. A. Carter, The Journal of Chemical Physics **100**, 3631 (1994).

[92] M. Feyereisen, G. Fitzgerald, and A. Komornicki, Chemical Physics Letters **208**, 359 (1993).

[93] M. Kobayashi, Y. Imamura, and H. Nakai, The Journal of Chemical Physics **127**, 074103 (2007).

[94] J. Almlöf, Chemical Physics Letters **181**, 319 (1991).

[95] M. Häser and J. Almlöf, The Journal of Chemical Physics **96**, 489 (1992).

[96] S. Saebø and P. Pulay, The Journal of Chemical Physics **115**, 3975 (2001).

[97] V. Fock, Zeitschrift für Physik **61**, 126 (1930).

[98] P. R. Nagy, G. Samu, and M. Kállay, Journal of Chemical Theory and Computation **12**, 4897 (2016).

[99] I. M. Høyvik, K. Kristensen, B. Jansik, and P. Jørgensen, J. Chem. Phys. **136**, 014105 (2012).

[100] R. K. Nesbet, "Electronic correlation in atoms and molecules," in *Advances in Chemical Physics* (John Wiley & Sons, Ltd, 1965) pp. 321–363.

[101] M. Schütz, G. Hetzer, and H.-J. Werner, The Journal of Chemical Physics **111**, 5691 (1999).

[102] M. Schütz and H.-J. Werner, Chem. Phys. Lett. **318**, 370 (2000).

[103] M. Schütz and H.-J. Werner, The Journal of Chemical Physics **114**, 661 (2001).

[104] M. Schwilk, D. Usvyat, and H.-J. Werner, The Journal of Chemical Physics **142**, 121102 (2015).

[105] J. M. Foster and S. F. Boys, Rev. Mod. Phys. **32**, 300 (1960).

[106] C. Edmiston and K. Ruedenberg, Rev. Mod. Phys. **35**, 457 (1963).

[107] J. E. Subotnik, Y. Shao, W. Liang, and M. Head-Gordon, The Journal of Chemical Physics **121**, 9220 (2004).

[108] J. Pipek and P. G. Mezey, The Journal of Chemical Physics **90**, 4916 (1989).

[109] G. Knizia, J. Chem. Theory Comput. **9**, 4834 (2013).

[110] P. E. Maslen, C. Ochsenfeld, C. A. White, M. S. Lee, and M. Head-Gordon, The Journal of Physical Chemistry A **102**, 2215 (1998).

[111] F. Aquilante, T. Bondo Pedersen, A. Sánchez de Merás, and H. Koch, The Journal of Chemical Physics **125**, 174101 (2006).

[112] C. Edmiston and M. Krauss, J. Chem. Phys. **45**, 1833 (1966).

[113] C. Edmiston and M. Krauss, The Journal of Chemical Physics **49**, 192 (1968).

[114] F. Neese, F. Wennmohs, and A. Hansen, The Journal of Chemical Physics **130**, 114108 (2009).

[115] Y. J. Franzke, C. Holzer, J. H. Andersen, T. Begušić, F. Bruder, S. Coriani, F. Della Sala, E. Fabiano, D. A. Fedotov, S. Fürst, S. Gillhuber, R. Grotjahn, M. Kaupp, M. Kehry, M. Krstić, F. Mack, S. Majumdar, B. D. Nguyen, S. M. Parker, F. Pauly, A. Pausch, E. Perlt, G. S. Phun, A. Rajabi, D. Rappoport, B. Samal, T. Schrader, M. Sharma, E. Tapavicza, R. S. Treß, V. Voora, A. Wodyński, J. M. Yu, B. Zerulla, F. Furche, C. Hättig, M. Sierka, D. P. Tew, and F. Weigend, Journal of Chemical Theory and Computation **19**, 6859 (2023).

[116] H. J. Monkhorst and J. D. Pack, Phys. Rev. B **13**, 5188 (1976).

[117] S. F. Boys and A. C. Egerton, Proceedings of the Royal Society of London. Series A. Mathematical and Physical Sciences **200**, 542 (1950).

[118] R. A. Shaw, International Journal of Quantum Chemistry **120**, e26264 (2020).

[119] T. Helgaker, P. Jørgensen, and J. Olsen, "Gaussian basis sets," in *Molecular Electronic-Structure Theory* (John Wiley & Sons, Ltd, 2000) Chap. 8, pp. 287–335.

[120] A. M. Burow, M. Sierka, and F. Mohamed, The Journal of Chemical Physics **131**, 214101 (2009).

[121] R. Łazarski, A. M. Burow, and M. Sierka, Journal of Chemical Theory and Computation **11**, 3029 (2015).

[122] A. Irmler, A. M. Burow, and F. Pauly, Journal of Chemical Theory and Computation **14**, 4567 (2018).

[123] G. Berghold, C. J. Mundy, A. H. Romero, J. Hutter, and M. Parrinello, Phys. Rev. B **61**, 10040 (2000).

[124] M. C. Clement, X. Wang, and E. F. Valeev, Journal of Chemical Theory and Computation **17**, 7406 (2021).

[125] C. M. Zicovich-Wilson, R. Dovesi, and V. R. Saunders, The Journal of Chemical Physics **115**, 9708 (2001).

[126] D. Usvyat and M. Schütz, Theoretical Chemistry Accounts **114**, 276 (2005).

[127] S. Casassa, C. M. Zicovich-Wilson, and C. Pisani, Theoretical Chemistry Accounts **116**, 726 (2006).

[128] J. Bhattacharjee and U. V. Waghmare, Phys. Rev. B **73**, 121102 (2006).

[129] M. Modugno and G. Pettini, New Journal of Physics **14**, 055004 (2012).

[130] A. Damle and L. Lin, "Disentanglement via entanglement: A unified method for wannier localization," (2018).

[131] V. Vitale, G. Pizzi, A. Marrazzo, J. R. Yates, N. Marzari, and A. A. Mostofi, npj Computational Materials **6**, 66 (2020).

[132] N. Marzari and D. Vanderbilt, Phys. Rev. B **56**, 12847 (1997).

[133] I. Souza, N. Marzari, and D. Vanderbilt, Phys. Rev. B **65**, 035109 (2001).

[134] D. P. Tew, Journal of Chemical Theory and Computation **15**, 6597 (2019).

[135] A. Redlack and J. Grindlay, Journal of Physics and Chemistry of Solids **36**, 73 (1975).

[136] L. Z. Stolarczyk and L. Piela, International Journal of Quantum Chemistry **22**, 911 (1982).

[137] K. N. Kudin and G. E. Scuseria, The Journal of Chemical Physics **121**, 2886 (2004).

[138] E. Ö. Jónsson, S. Lehtola, M. J. Puska, and H. Jónsson, Journal of chemical theory and computation **13**, 460 (2016).

[139] A. Zhu and D. P. Tew, The Journal of Physical Chemistry A **128**, 8570 (2024).

[140] F. Weigend, Phys. Chem. Chem. Phys. **8**, 1057 (2006).

[141] M. F. Peintinger, D. V. Oliveira, and T. Bredow, Journal of Computational Chemistry **34**, 451 (2013).

[142] J. Laun, D. Vilela Oliveira, and T. Bredow, Journal of Computational Chemistry **39**, 1285 (2018).

[143] A. D. Becke, The Journal of Chemical Physics **98**, 5648 (1993).

[144] C. Lee, W. Yang, and R. G. Parr, Phys. Rev. B **37**, 785 (1988).

[145] S. Grimme, Journal of Computational Chemistry **27**, 1787 (2006).

[146] M. Challacombe, C. White, and M. Head-Gordon, The Journal of Chemical Physics **107**, 10131 (1997).

[147] H.-J. Werner, The Journal of Chemical Physics **145**, 201101 (2016).

[148] D. P. Tew, B. Helmich, and C. Hättig, J. Chem. Phys. **135**, 074107 (2011).

[149] T. Helgaker, W. Klopper, H. Koch, and J. Noga, J. Chem. Phys. **106**, 31 (1997).

[150] D. Bakowies, J. Chem. Phys. **127**, 084105 (2007).

[151] Y. Minenkov, E. Chermak, and L. Cavallo, J. Chem. Theory Comput. **11**, 4664 (2015).

[152] F. A. Bischoff, S. Wolfsegger, D. P. Tew, and W. Klopper, Mol. Phys. **107**, 963 (2009).

[153] D. P. Tew and W. Klopper, J. Chem. Phys. **123**, 074101 (2005).

[154] K. E. Yousaf and K. A. Peterson, J. Chem. Phys. **129**, 184108 (2008).

[155] F. Weigend and R. Ahlrichs, Phys. Chem. Chem. Phys. **7**, 3297 (2005).

[156] F. Weigend, F. Furche, and R. Ahlrichs, J. Chem. Phys. **119**, 12753 (2003).

[157] T. H. Dunning, J. Chem. Phys. **90**, 1007 (1989).

[158] R. A. Kendall, T. H. Dunning, and R. J. Harrison, J. Chem. Phys. **96**, 6796 (1992).

[159] N. B. Balabanov and K. A. Peterson, J. Chem. Phys. **123**, 064107 (2005).

[160] G. Schmitz, B. Helmich, and C. Hättig, Mol. Phys. **111**, 2463 (2013).

[161] E. Semidalas and J. M. Martin, J. Chem. Theory Comput. **18**, 883 (2022).

[162] I. Sandler, J. Chen, M. Taylor, S. Sharma, and J. Ho, J. Phys. Chem. A **125**, 1553 (2021).

[163] A. Altun, F. Neese, and G. Bistoni, J. Chem. Theory Comput. **16**, 6142 (2020).

[164] D. W. Schwenke, J. Chem. Phys. **122**, 014107 (2004).

[165] R. Huenerbein, B. Schirmer, J. Moellmann, and S. Grimme, Phys. Chem. Chem. Phys. **12**, 6940 (2010).

[166] M. A. Iron and T. Janes, J. Phys. Chem. A **123**, 3761 (2019).

[167] H.-J. Werner and A. Hansen, J. Chem. Theory Comput. **0**, null (0).

[168] S. Dohm, M. Bursch, A. Hansen, and S. Grimme, J. Chem. Theory Comput. **16**, 2002 (2020).

[169] F. Weigend and R. Ahlrichs, Phys. Chem. Chem. Phys. **7**, 3297 (2005).

[170] M. Dolg and X. Cao, Chem. Rev. **112**, 403 (2012).

[171] M. Häser and R. Ahlrichs, J. Comput. Chem. **10**, 104 (1989).

[172] F. Weigend, Phys. Chem. Chem. Phys. **8**, 1057 (2006).

[173] F. Weigend, A. Köhn, and C. Hättig, J. Chem. Phys. **116**, 3175 (2002).

[174] D. P. Tew, J. Chem. Theory Comput. **15**, 6597 (2019).

[175] J. Yang, Y. Kurashige, F. R. Manby, and G. K. L. Chan, J. Chem. Phys. **134**, 044123 (2011).

[176] G. Schmitz, B. Helmich, and C. Hättig, Mol. Phys. **111**, 2463 (2013).

[177] O. Masur, D. Usvyat, and M. Schütz, J. Chem. Phys. **139**, 164116 (2013).

[178] M. Schütz, O. Masur, and D. Usvyat, J. Chem. Phys. **140**, 244107 (2014).

[179] C. Riplinger, B. Sandhoefer, A. Hansen, and F. Neese, J. Chem. Phys. **139**, 134101 (2013).

[180] G. Schmitz and C. Hättig, J. Chem. Phys. **145**, 234107 (2016).

[181] T. Helgaker, W. Klopper, H. Koch, and J. Noga, J. Chem. Phys. **106**, 31 (1997).

[182] C. Hättig, W. Klopper, A. Köhn, and D. P. Tew, Chem. Rev. **112**, 4 (2012).

[183] F. Neese, F. Wennmohs, and A. Hansen, J. Chem. Phys. **130**, 114108 (2009).

[184] J. Pogrebetsky, A. Siklitskaya, and A. Kubas, J. Chem. Theory Comput. **19**, 4023 (2023).

[185] C. Gunanathan, B. Gnanaprakasam, M. A. Iron, L. J. Shimon, and D. Milstein, Journal of the American Chemical Society **132**, 14763 (2010).

[186] M. Gray and J. M. Herbert, The Journal of Chemical Physics **161** (2024).

[187] D. P. Tew, J. Chem. Phys. **148**, 011102 (2018).